



HAL
open science

Design Optimization and Control for Concentric Tube Robot in Assisted Single-Access Laparoscopic Surgery

Mohamed Nassim Boushaki

► **To cite this version:**

Mohamed Nassim Boushaki. Design Optimization and Control for Concentric Tube Robot in Assisted Single-Access Laparoscopic Surgery. Robotics [cs.RO]. Université Montpellier, 2016. English. NNT : 2016MONTT294 . tel-01817565

HAL Id: tel-01817565

<https://theses.hal.science/tel-01817565v1>

Submitted on 18 Jun 2018

HAL is a multi-disciplinary open access archive for the deposit and dissemination of scientific research documents, whether they are published or not. The documents may come from teaching and research institutions in France or abroad, or from public or private research centers.

L'archive ouverte pluridisciplinaire **HAL**, est destinée au dépôt et à la diffusion de documents scientifiques de niveau recherche, publiés ou non, émanant des établissements d'enseignement et de recherche français ou étrangers, des laboratoires publics ou privés.

THÈSE

Pour obtenir le grade de
Docteur

Délivré par l'Université de Montpellier

Préparée au sein de l'école doctorale **I2S***
Et de l'unité de recherche **UMR 5506**

Spécialité: **Systèmes Automatiques et Microélectroniques**

Présentée par **Mohamed Nassim BOUSHAKI**

**Design Optimization and Control for
Concentric Tube Robot in Assisted
Single-Access Laparoscopic Surgery**

Soutenue le 06/10/2016 devant le jury composé de :

PHILIPPE POIGNET	Professeur	Univ. de Montpellier	Direct. de thèse
CHAO LIU	CR CNRS	LIRMM	Co-encadrant
NICOLAS Andreff	Professeur	Univ. Franche-Comté, Besançon	Rapporteur
JÉRÔME Szewczyk	Professeur	UPMC Paris 6	Rapporteur
STEPHANE Caro	CR CNRS	IRCCyN Nantes	Examineur
BENOÎT Herman	CR FNRS	UCL-MEED, Belgique	Examineur
SALIH ABDELAZIZ	MCF	Univ. de Montpellier	Invité



ACKNOWLEDGEMENTS

I would like to thank my advisors, Prof. Philippe Poignet and Dr. Chao Liu, for giving me the opportunity to be a Doctor, for guiding me, and for all the scientific discussions and meetings that we spent together during this period of PhD.

Many thanks to Dr. Etienne Dombre, Dr. Salih Abdelaziz, Dr. Nabil Zemiti and Prof. Yassine Haddab for their orientations during the team meetings.

I would like to thank the medicine doctors Vincent Trevillot and Mohamed Akkari for their help in the medical part of this work.

Thank you Dr. Olivier Company, Dr. Benoit Herman, Laurent Schoevaerds and Laurianne Akoto for the contribution to the mechanical design.

Thank you Olivier Tempier, Pierre-Elie Herve and Dr. Robin Passama for your help.

I would also like to thank all my colleagues and friends especially Gamal Elghazaly, Moussab Bennehar, Hamza Farkoud and Bilal Benchabla. Thank you for the good times that we shared.

I would like to acknowledge the CAMI Labex project for supporting this work.

*To my dear mother Nacera for her encouragement, to my dear father Youcef,
to my sister Soraya and my little brother Mehdi, to all my family and to Amar
Ezzahi...*



Contents

Contents	iii
Abstract	3
Résumé	5
1 General Introduction and Motivation	7
1.1 Robotic assisted surgery and flexible robots	7
1.2 Concentric tube robots	8
1.3 Motivations of the thesis	9
1.3.1 Medical motivation	9
1.3.2 Technical motivation	10
1.4 Organization of the thesis	11
2 From Design to Control of Concentric Tube Robots: A Literature Survey	13
2.1 Introduction	14
2.2 Design of CTR	14
2.2.1 Actuation unit design	15
2.2.2 Tubes design	22

2.3	Kinematic models of CTR	27
2.4	Motion planning	29
2.5	Control of CTR	30
2.6	Conclusion	33
3	Kinematic Modelling of Concentric Tube Robot	35
3.1	Introduction	36
3.2	Forward kinematic model of concentric tube robot	36
3.2.1	Infinite stiffness model	36
3.2.2	Bending model	42
3.2.3	Straight torsion model	44
3.2.4	Torsionally compliant model	45
3.3	Differential kinematic model of concentric tube robot	48
3.4	Inverse kinematic model	50
3.5	Bifurcation phenomenon	52
3.6	Conclusion	54
4	Optimization of CTR Design for Deep Anterior Brain Tumor Surgery	55
4.1	Introduction	56
4.2	Multi-objective optimization using Pareto methods	59
4.3	Techniques used to solve multi-objective optimization problem	59
4.3.1	Scalarization technique	60
4.3.2	Grid-searching technique	61
4.4	Targeted surgical application	63
4.5	Workspace characterization and anatomical constraints	64
4.6	CTR configuration selection	66
4.7	Formulation of grid-searching optimization algorithm for CTR	69
4.7.1	Decision space of the CTR optimization problem	70
4.7.2	Objective space of the CTR optimization problem	71
4.7.3	Constraints	72
4.7.4	Grid-searching algorithm	73
4.8	Results and discussions	74

4.9	Conclusion	78
5	Task-space Position Control of CTR Using Approximated Jacobian	79
5.1	Introduction	80
5.2	Formulation of CTR position control task at actuator level	81
5.3	Task-space position control of CTR with inaccurate kinematics	82
5.4	Simulation studies	86
5.5	Conclusion	94
6	Conclusions and Perspectives	97
6.1	Conclusions	97
6.2	Perspectives	98
A	LIRMM CTR Prototype	101
A.1	CAD design	102
A.2	Motors used	104
	A.2.1 Translation motors: ref. 283833	104
	A.2.2 Rotation motors: ref. 283833	105
A.3	Gears connected to the motors	106
	A.3.1 Gears connected to the translation motors	106
	A.3.2 Gears connected to the rotation motors	107
A.4	Motion transmission	108
	A.4.1 Translation transmission: spindle drive	108
	A.4.2 Translation transmission: gear	109
A.5	Sensors used	111
	A.5.1 Joint position sensors used for the translation and rotation motors	111
	A.5.2 Proximity sensors used for the translated blocks	112
A.6	Controllers	114
A.7	Communication loop	115
	Bibliography	117
	List of Figures	127

List of Tables

130



Abstract

Concentric Tube Robots (CTR) are becoming more and more popular in medical robotics community. In this thesis, a general literature survey on existing works covering the research topics of CTR is first presented. The kinematics of CTR is more specifically detailed since it is the basics of the main contributions of this thesis. The first contribution is a concept study of exploiting CTR for resection of deep brain tumors located at the frontal lobe. Grid searching has been used as the optimization method for the CTR tubes design. This method allows to avoid the crucial problem of weights preselection which is required in all scalarization methods existing in literature. Instead, the grid searching method used in this work allows to choose the optimal parameters with the help of graphical illustration of calculation results distribution with respect to the selection criteria. The elastic stability dues to the bending and torsion interaction between tubes is considered and evaluated with a new approach introduced in this work. The second contribution then is to deal with the kinematic uncertainties in motion control of CTR. The proposed control method designed at the actuator level shows that the control design of actuator input with task-space feedback and approximate Jacobian matrix provides robustness in handling inaccuracy in kinematic model and maintains good control performance at the same time.



Résumé

Les robots à tubes concentriques deviennent de plus en plus populaires dans la communauté de la robotique médicale. Dans cette thèse, un état de l'art général des travaux existants et qui couvre les thématiques de recherche en robots à tubes concentriques (RTC) est présenté dans un premier temps. Les modélisations géométrique (directe et inverse) et cinématique des RTC sont détaillées car elles servent de base pour les contributions de cette thèse. La première contribution consiste en une étude de concept d'utilisation des RTCs pour la résection des tumeurs profondes situées au niveau du lobe frontal du cerveau. 'Grid searching' a été utilisée comme méthode d'optimisation pour la conception des tubes des RTCs. Cette méthode permet d'éviter le problème crucial de présélection des coefficients de pondération, cette pondération étant nécessaire dans toutes les méthodes de scalarisation existantes dans la littérature. La méthode de 'grid searching' utilisée dans ce travail permet la sélection des paramètres optimaux avec l'aide d'une illustration graphique de la distribution des résultats de calcul concernant les critères de sélection. La stabilité élastique due aux interactions des tubes en flexion et en torsion est incluse dans les critères de sélection et est évaluée avec une nouvelle approche introduite dans ce travail. La deuxième contribution de cette thèse repose sur la synthèse d'une loi de commande qui permet de faire face aux incertitudes cinématiques dans le contrôle de mouvement des RTCs. L'étude réalisée a montré qu'un contrôle au niveau des couples moteurs avec un retour dans l'espace opérationnel et une matrice Jacobienne

approchée, ce contrôle assure une robustesse en présence des incertitudes cinématiques au niveau de la matrice Jacobienne et permet d'obtenir des bonnes performances de contrôle en terme d'erreur de poursuite.

General Introduction and Motivation

1.1 Robotic assisted surgery and flexible robots

The evolution of surgery from traditional open surgery to minimally invasive surgery (MIS) has witnessed an improvement of the surgical outcomes (reduced patient trauma, less blood-loss, shorter recovery duration, etc). This improvement is due to the miniature incisions compared to large openings on patient body. However, remarkable limitations are associated to this technique. The accessibility to the surgical target passing through complex 3D paths and the control of the rigid instruments used is more difficult (constrained manipulability, dexterity, degrees of freedom, etc) [Vitiello et al., 2013]. All these have motivated the use of robotic assistance for better benefits of MIS. Robotic assisted surgery started in 2000, with the objective of enhancing the surgical procedure while maintaining the advantages of open surgery in MIS [Satava, 2003]. Robotic systems offer many advantages to MIS procedures: facilitate access to the surgical target with more dexterity and degrees of freedom; enhance the vision of the anatomical structures; enhance the precision of the instrument positioning; eliminate the hand tremor of the surgeon manipulating a teleoperation arm and generate smoother trajectory of the instrument than the trajectory of the hand manipulation ; reduce the fatigue of surgeon thanks to ergonomic studies (comfortable seat position, 3D visual feedback, etc), etc [Rosen et al., 2011].

In MIS interventions, the often used instruments can be classified into three main classes [Dupont et al., 2010a]:

- The first class consists of flexible needles with a straight shaft. They are used for percutaneous insertions in tissues. The needle relies on the lateral forces to steer and change its direction thanks to the guidance forces applied at its base and thanks to its bevel tip. The limitation of this class of instrument is its dependence on tissues, i.e. it can not steer in curved tubular cavities. Moreover, these instruments are not able to produce lateral tip motion without relying on solid tissues penetration.
- The second class of instruments includes straight and stiff shaft with an articulated tool mounted on the tip. The insertion of the instrument from the body entry to the target should be straight and the manipulation of the tool during the operation is ensured by pivoting around the body entry which on the other hand can cause tissues deformation. The straight and stiff shaft is difficult to pass through complex cavity as well.
- The last class is composed of elongated steerable devices such as catheters and multi-stage microrobot devices typically mounted at the distal extremity of a rigid shaft and includes a flexible backbone.

Flexible robots with small size are more suitable for MIS as they can reach surgical sites of high access difficulty with straight rigid instruments [Burgner-Kahrs et al., 2015]. Concentric tube robots belong to this category of flexible robots with the advantage of good steerability compared to rigid devices and controllability of the shape and force compared to catheters with small size. The concept of CTRs is briefly presented in the next section.

1.2 Concentric tube robots

CTR is composed of pre-shaped flexible tubes, mostly made of Nitinol. The tubes are inserted concentrically one into another forming a flexible and controllable robot shaft. Usually the tubes used are composed of two parts: a straight part followed by a curved one (cf. Figure 1.1.a and Figure 1.1.b). The tubes are actuated in axial rotation and linear displacement. Actuating the tubes creates an elastic interaction between them and creates a deformation of the robot shape. The shaft of the robot is composed of a set of sections with different curvatures. The frontiers of the sections are defined by the starting and the end points of each straight

or curved part of all the tubes (cf. Figure 1.1.c). A more detailed description of the CTR kinematics is provided in Chapter 3.

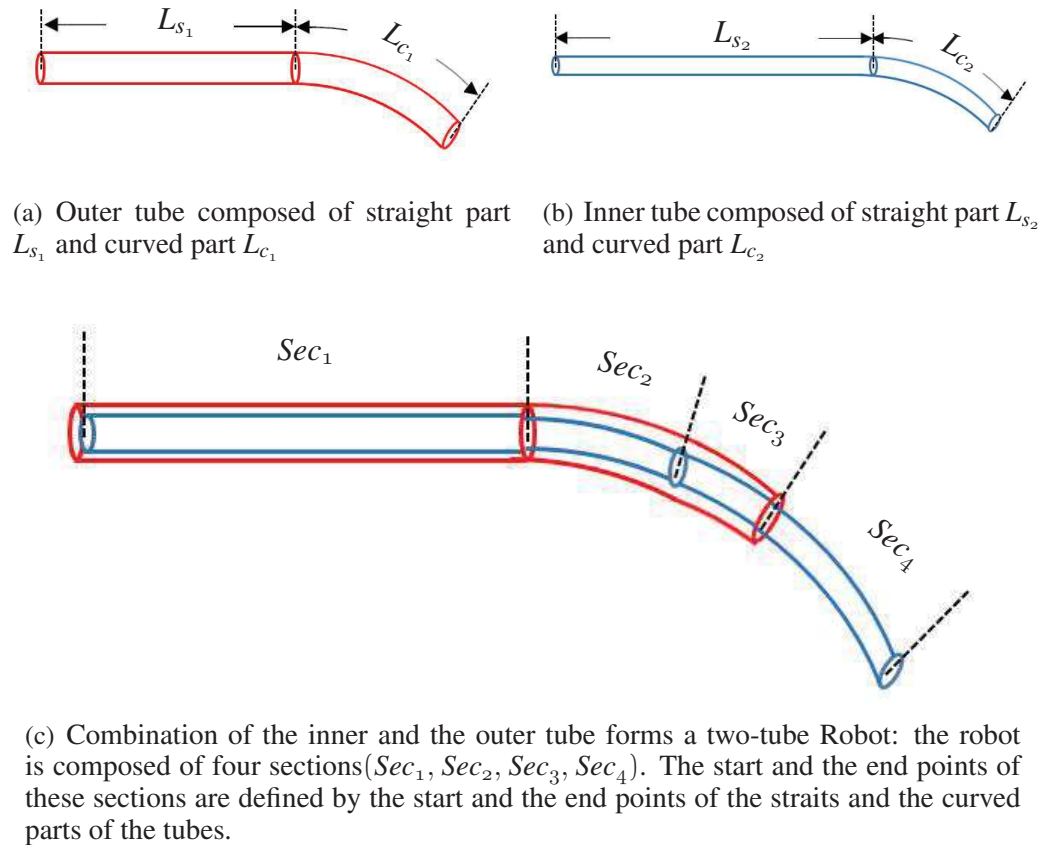


Figure 1.1 – Conception of a concentric tube robot.

1.3 Motivations of the thesis

1.3.1 Medical motivation

It is noted that in 2012, 70% of the over 250000 patients with brain tumor died in the world, this number of deaths is predicted to reach 230000 in 2020 [IAR]. Anterior deep brain tumors are difficult to access with MIS, and its resection requires a cranium access for good accessibility to the surgical target currently. A part of the cranium is severed to ensure an open surgery then fixed once the tumor is resected. This trans-cranial procedure is very traumatic

as the surgeon needs to lift the brain in order to reach the deep tumor located under it. This manipulation causes a swelling of the brain after the operation which creates a high pressure at the brain level.

The concept of an endonasal approach (see Figure 1.2) is studied in this thesis by using CTR which is flexible and adaptable with the anatomical complexity. This operation requires bone drilling in order to access the surgical site. But the insertion path is from the nostril to the anterior wall of the frontal sinus (location of the drilling point) and is surrounded by structures of high sensitivity. The optimization algorithm used is dedicated to this surgical application and aims to obtain the optimal CTR design.

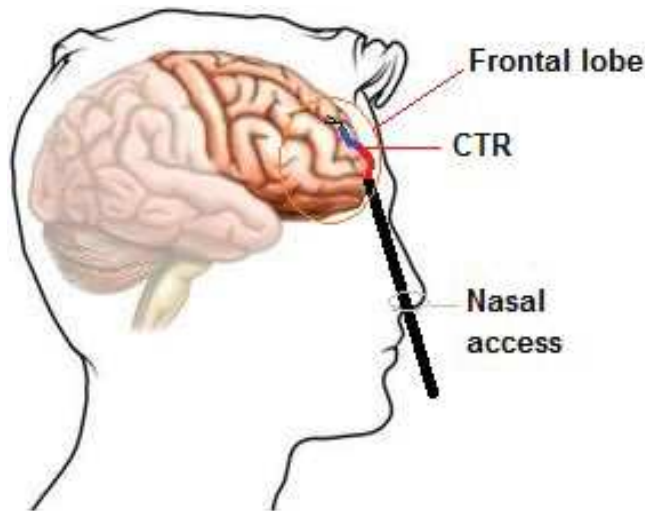


Figure 1.2 – Nasal access to the frontal lobe using CTR.

1.3.2 Technical motivation

For a CTR robot, the shape is defined by the interaction between its tubes. This interaction is created by actuating the tubes in axial rotations and linear translations. Once the tubes interact between each other, they are deformed and result in bending and torsion. The deformation depends on the pre-curvatures of the tubes, their length, their stiffness, and also their translation and rotation. The existing kinematic models which allow to define the robot shape with respect to the rotations and translations of the tubes and taking into account the bending and the torsion between the tubes are complicated, time consuming and not very ac-

curate. Moreover, most of position control strategies developed for CTR are considered in the joint space, which keeps the position control performances highly dependent on the kinematic modelling accuracy. A task-space controller at the actuator level is developed in this thesis in order to reduce the effect of kinematic inaccuracies and guarantee motion control accuracy at the same time.

Another issue in CTR position control is the bifurcation phenomenon. The interaction between the tubes creates an elastic energy which can be stored and suddenly dissipated for some specific configurations. This leads to tip jump which is not safe for medical interventions. In general, the jumps occur for tubes with high curvatures and large lengths and when the difference of rotation angles of the tubes is in the neighborhood of π . In literature, two solutions are proposed to avoid this problem: optimize the tubes dimensions which reduce the bifurcation, and consider the critical configurations at the level of motion planning to avoid them. In this thesis, a new approach to evaluate the bifurcation effect based on the tip trajectory smoothness is proposed. This bifurcation evaluation index and the reachability of the desired surgical volume are used as criteria of a Pareto grid-searching optimization algorithm for CTR design. The objective is to calculate the optimal tubes curvatures which maximize the reachability and minimize the proneness to bifurcation. The Pareto grid-searching optimization method used allows an interpretation of the results without any weights pre-selection comparing to the scalarization methods in literature which require a pre-selection of the weights for the different cost sub-functions composing the global cost function.

1.4 Organization of the thesis

The thesis is organized as follows:

- In Chapter 2, the existing works of CTR in literature are briefly presented under different categories: the design of CTR; the kinematic modelling of CTR; the motion planning; and the control of CTR. The objective of this chapter is to provide a general framework of CTR literature although this thesis mainly focuses on design optimization and control.
- In Chapter 3, the forward, differential, and inverse kinematic models of CTR are presented in detail since they serve as the basis for CTR design and control.

- The Pareto grid-searching optimization method for the design of a CTR robot dedicated to frontal lobe tumor removal and a new method to evaluate the tubes elastic stability are introduced in Chapter 4.
- The chapter 5 presents a new control strategy from the actuator level to compensate the inaccuracies due to the kinematic modelling. Simulation study results are shown to justify the effectiveness of the proposed control method comparing to traditional inverse kinematic method.
- The last chapter concludes the work presented in this thesis and provides some perspectives on future works.
- The prototype of a CTR robot together with its CAD design, motors and sensors selection are presented in the Appendix.

From Design to Control of Concentric Tube Robots: A Literature Survey

Preamble

The motivation to design concentric-tube robot (CTR) is to fulfill clinical tasks requirements of navigation through complex paths and high manipulation dexterity. To reach this objective, efforts have been made to improve the design of CTR, to develop their appropriate kinematic modelling and their path planners, and to improve the performance of posture control. This chapter presents a general literature survey on existing works covering the aforementioned research topics of CTR [Boushaki et al., 2016].

Contents

2.1	Introduction	14
2.2	Design of CTR	14
2.3	Kinematic models of CTR	27
2.4	Motion planning	29
2.5	Control of CTR	30
2.6	Conclusion	33

2.1 Introduction

Since CTRs have been introduced with the objective of more contribution and enhancement to robotic assisted surgery in general thanks to their dexterity and miniature-size, they have mainly witnessed four research axes: the design of the actuation unit and of the tubes; the kinematics modelling; the path planing; and the control. The progress in design of the actuation unit was mainly to propose MRI compatible prototypes with different solutions (pneumatic and piezoelectric actuation). The tubes design and path planing works are often presented in a medical context i.e. define the optimal tubes parameters and the optimal joint sequence to navigate through a path while ensuring the sensitive anatomical structures. Many works have been conducted in kinematics modelling to improve the accuracy by considering more realistic physical phenomena and some control strategies have been developed for CTR position control. In this chapter, existing works in literature on all these topics are briefly introduced to provide a general framework of CTR study, though this thesis mainly focuses on the tubes design and motion control problems.

2.2 Design of CTR

In terms of mechanical structure, CTRs have special characteristics. They look like serial robot but with flexible and length variable links without discrete articulations, and also they look like parallel robot because the actuators are not distributed along the robot arm. The robot then is composed of two main parts: the actuation unit which ensures the translation and the rotation of the tubes, and the second part is the robot arm composed of concentric tubes. To accomplish a specific task, the integration of other mechanical and/or electronic devices on the robot arm would be required for sensing and manipulating. In this section, existing works on design of both actuation unit and arm (tubes) are presented.

2.2.1 Actuation unit design

Since the concept of CTR was introduced, different mechanisms of actuation unit (AU) have been designed. The AU is composed of actuation blocks which carry the tubes in translation and are equipped with rotation actuators. The number of the actuation blocks is equal to the number of the actuated tubes. In terms of repartition of the actuation blocks, CTR AUs can be classified into two categories: AU with serial blocks and AU with parallel blocks. In this part, the majority of existing AUs (serial and parallel) are presented according to:

- the number of actuated tubes;
- the coupling of the rotation and translation motions;
- the number of the robot arms;
- the actuators nature and the MRI compatibility of the robot.

Serial actuation unit

A serial AU is composed of a set of actuation blocks ensuring the rotation and the translation (which can be coupled or not) of each tube. These blocks are distributed in a *one followed by another* configuration (see Figure 2.1). Here, some typical serial AU are introduced and their actuation mechanism are explained.

For the robot illustrated in Figure 2.2, the AU is composed of three actuation blocks to drive three tubes in rotation and translation. The mechanism of actuation is a nut/screw system with a guidance rail which guides the block during translation. The nut and the screw are rotated independently using one motor for each. For the screw, the motion transmission is ensured by a belt, and the nut is fixed on the motor shaft. The extremity of each tube is fixed on its corresponding nut. Holes are drilled on the nuts to allow the concentric insertion of the tubes.

The actuation of a screw creates a block sliding on the guidance rail, which produces a translation of the tube. The rotation of the nut produces two motions: linear translation and axial rotation of the tube. To create a pure rotation of the tube, both nut and screw actuation are required, but with opposite directions of rotation.

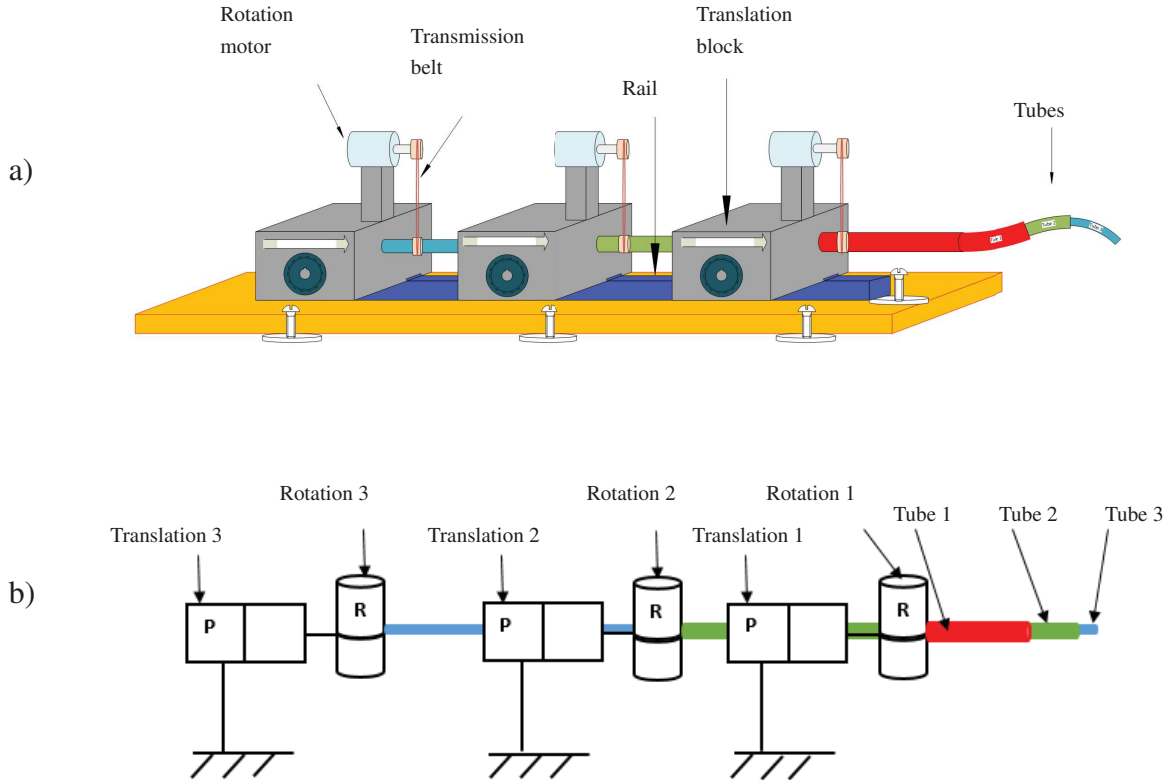


Figure 2.1 – Actuation unit with serial translation blocks: a) structure, b) kinematic scheme.

This actuation system results in the coupled rotation and translation of a tube, i.e. the actuation of one motor creates rotation and translation motions. The rotation of one tube requires the actuation of two motors. The quantities of translations and rotations of the tubes are indispensable to define the arm shape. They are calculated arithmetically from the motors rotation angles and other parameters (gears, pulleys diameters, screw/nut pitches). This block distribution makes the distance between the base of the innermost tube and the base of the outermost tube too long which requires a long innermost tube. As the torsion deformation of the tube is proportional to its length, the innermost tube is then more prone to this deformation. The actuators used are DC motors which are not MRI compatible.

The prototype designed by Burgner et al. in [Burgner et al., 2011] and [Burgner et al., 2014] was the first bimanual CTR (Figure 2.3). The two arms are actuated by two parallel

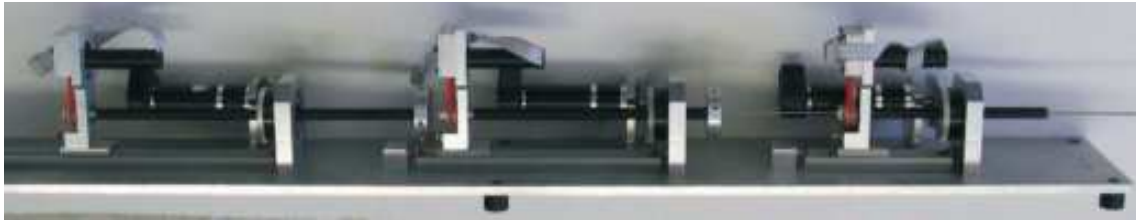


Figure 2.2 – CTR with serial actuation blocks and coupled rotation/translation for three tubes [Webster III, 2007]

axes. Each axis is composed of a screw which supports three serial blocks. Each block is composed of a motorized nut to drive the block in translation, and another motor to actuate the rotation. When the blocks are translated to their maximal extremities, the space between blocks is reduced thanks to the perpendicular positioning of the blocks with the axes, comparing to the previous prototype in which they are co-axial. Two parallel guidance rails are fixed at the base of the device to support and guide the blocks. The actuators of this MRI non-compatible device are DC motors, and for each DOF only one motor is used. In total the actuation structure includes six motors per arm, with three for the rotations and three for the translations independently without any coupling.



Figure 2.3 – RTC equipped with two three-tubes arms and an actuation serial unit without coupling [Burgner et al., 2011] [Burgner et al., 2014].

Pneumatic actuators in [Cardona, 2012] and piezoelectric actuators in [Su et al., 2012] have been used to ensure the MRI compatibility of CTR. These two prototypes are illustrated

in Figure 2.4.a and Figure 2.4.b respectively. The robot AU designed in [Cardona, 2012] allows to drive two tubes. The innermost tube is controlled only in translation, but, the middle tube is controlled in both translation and rotation. A passive outermost tube is added. The translations are actuated by pneumatic cylinders controlled through valves (cylinder-valve system). The rotation is also actuated pneumatically with a cylinder connected to a rack and pinion system. The rotation stage is carried by the translation one and the whole block relies on an aluminum guidance rail. This prototype is MRI compatible with no coupling rotation and/or translation. The encoders used for the joint position sensing are optical.

In [Su et al., 2012], the specification of the structure is that the base of the CTR is not fixed and is manipulated through an orientation and positioning of a 3 DOFs module. The mechanical structure of the CTR is identical to the previous prototype, except the actuators which are piezoelectric motors controlled from an outside workstation. The rotation motion is transmitted via a belt from the motor.

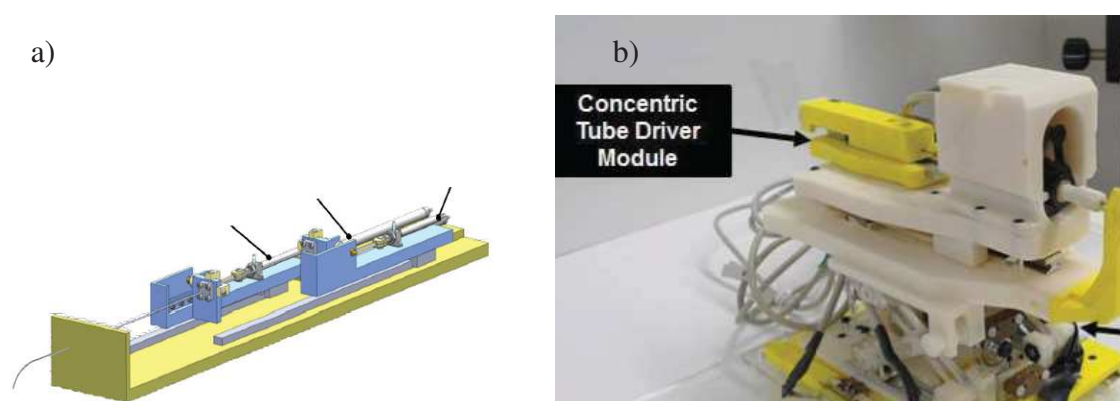


Figure 2.4 – Two-tubes CTR with a) pneumatic actuation unit [Cardona, 2012] and b) piezoelectric actuation unit [Su et al., 2012] non coupled.

Another pneumatic AU, illustrated in the Figure 2.5, with three tubes mounted has been designed by Comber et al. [Comber et al., 2012]. The outermost tube has pure translation as the only DOF and the two others are actuated in both rotation and translation. The particularity of this device is the coupling of the translations: the translation of the outermost tube produces the same quantity of translation for the two others, and the translation of the middle one causes the same translation for the innermost one. The translation of the innermost tube concerns

only itself. The actuation of the translation stage is ensured by a piston-cylinder system. For the rotation, a linear-to-rotary mechanism converter with a belt is used.

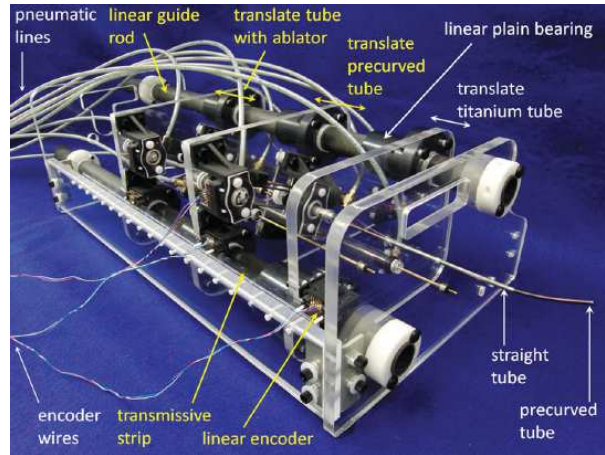


Figure 2.5 – Three-tubes CTR actuated pneumatically with translation coupling [Comber et al., 2012].

Parallel actuation unit

The blocks of a parallel AU are distributed and translated *in parallel with each other*, as show in Figure 2.6.

The first parallel AUs have been reported by Dupont et al. [Dupont et al., 2010a] and Gosline et al. [Gosline et al., 2012a] with both prototypes having the same mechanical structure. The particularity of these prototypes compared to the serial ones is the parallelization of the actuation blocks. Three parallel nut/screw axes are used for the translations, with one motor per nut fixed at its extremity. Theses axes are used for the tubes translations, and each translated screw carries with it a motor dedicated to the rotation. The rotation motion is transmitted through a belt in [Gosline et al., 2012a] (see Figure 2.7.a) or a gearing in [Dupont et al., 2010a] (see Figure 2.7.b). The motions of the tubes are decoupled with each motor creating only one motion for one tube: a linear translation or an axial rotation. Another advantage of this mechanism is the reduction of the tubes lengths as they are actuated by parallel blocks rather than serial ones. The presented devices actuate a single arm with three tubes using DC motors and hence is not MRI compatible.

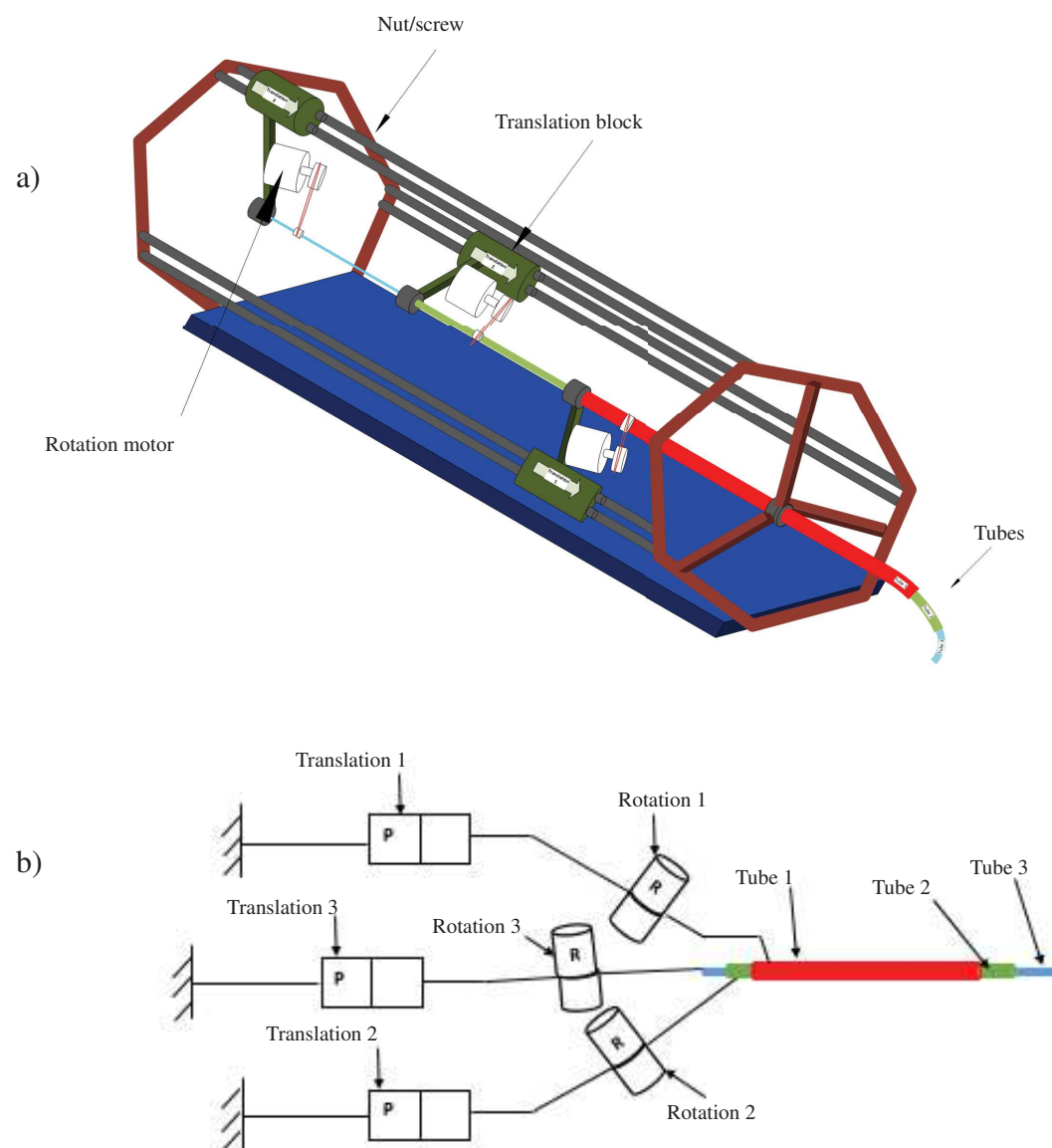


Figure 2.6 – CTR actuation unit with parallel translation blocks: a) structure b) kinematic graph.

In [Xu et al., 2013], two motorized linear slides are assembled perpendicularly on the base

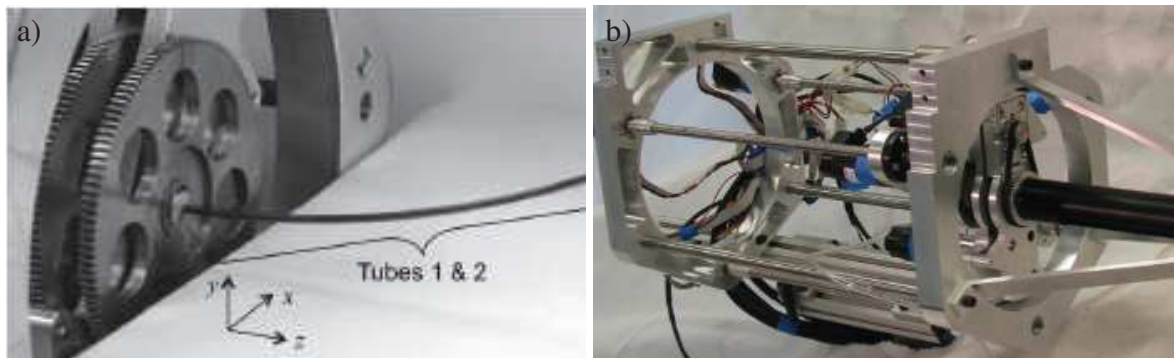


Figure 2.7 – RTC a) [Dupont et al., 2010a] b) [Gosline et al., 2012a] with three tubes decoupled and actuated in parallel.

which allows to reduce the tubes length. The linear slides ensure the translations of two serial rotary stages which are in charge of the two tubes rotations. All rotations and translations are decoupled. The device includes a single arm and is not MRI compatible.

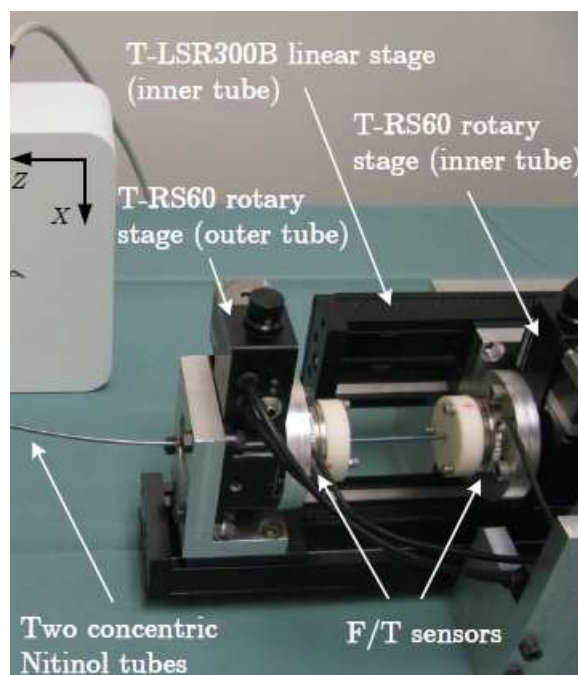


Figure 2.8 – Two-tubes CTR with parallel actuation unit [Xu et al., 2013]

As the sterilization of medical devices is an important issue, Hendrick et al. have isolated the actuators from the transmission stage with a sterile barrier [Hendrick et al., 2014]. The

designed robot is a two-arm CTR inserted in a common sheath (see Figure 2.9). The first arm is a two-tube robot with three DOFs. The first tube is actuated in both rotation and translation, and the other is actuated only in translation. The second arm has three tubes with six DOFs. All the tubes are actuated in both rotation and translation. The tubes are fixed on the translated blocks, and the rotation motion is transmitted through a rotated square shaft. The transmission part is designed to be biocompatible and autoclavable. This robot is also particular in the sense that it is intended to be a hand-held robot.

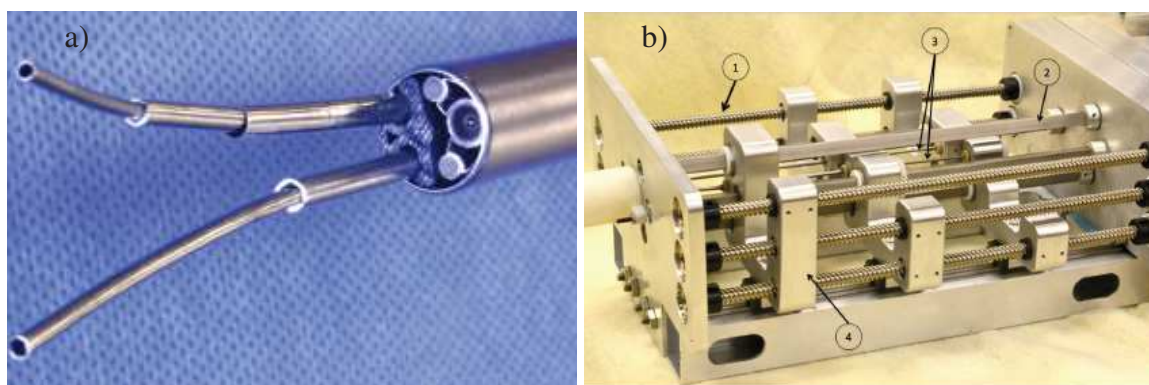


Figure 2.9 – a) Two arms CTR with b) parallel actuation unit [Hendrick et al., 2014].

The serial AU is more oftenly used than the parallel as the latter is more complicated in design. Despite the particularity of each prototype, their *skeletons* resemble each other. The structure for the majority of the prototypes is mainly composed of translating blocks thanks to a nut/screw system and supporting rotation motors. The rotation is usually transmitted to the tube through a belt or gearing. The actuation characteristics of most existing CTR prototypes are summarized in the Table.2.1. A new actuating technique of CTR has been introduced in [Chikhaoui et al., 2016] based on embedded soft micro-actuation.

2.2.2 Tubes design

The arm of a concentric tube robot is a set of pre-shaped super-elastic tubes combined concentrically. The tubes used are usually composed of two sections: a straight section with an extremity fixed on its corresponding rotary axis and a distal pre-curved section. Once the tubes are inserted inside each other and actuated in rotation and translation, elastic interactions

Table 2.1 – Existing CTR prototypes.

Prototype	Number of arms	Number of actuated tubes	Number of DOF	Actuation coupling	MRI compatibility and actuators nature
[Webster III, 2007]	1	3	6	Rot/Trans	No DC Motors
[Dupont et al., 2010a] [Gosline et al., 2012a]	1	3	6	No	No DC Motors
[Burgner et al., 2011] [Burgner et al., 2014]	2	3x2	6x2	No	No DC Motors
[Cardona, 2012]	1	2	3	No	Yes Pneumatic
[Su et al., 2012]	1	2	3	No	Yes Piezoelectric
[Comber et al., 2012]	1	3	6	Trans/Trans	Yes Pneumatic
[Burgner et al., 2012]	1	0	-	No	No Manual
[Butler et al., 2012]	1	2	3	No	No DC Motors
[Swaney et al., 2012]	4	4x3	4x6	No	No DC Motors
[Xu et al., 2013] [Xu et al., 2014]	1	2	4	No	No DC Motors
[Hendrick et al., 2014]	2	3+2	6+3	No	No DC Motors
[Burgner et al., 2013b]	1	2	3	No	No DC Motors
[Azimian et al., 2014]	1	2	4	No	No DC Motors
[Swaney et al., 2015]	1	2 + 1 wire	4+2	Non	No DC Motors

between them (bending and torsion) occur. All these make the shape and the length of the robot arm change.

It is obvious that a specific clinical task requires specific robot shape and length. The shape

and length depend on the tubes specifications (length, curvature, outer and inner diameter, stiffness, etc). This motivates the optimization works introduced in this section, which mainly aim to define the optimal lengths and curvatures of the tubes for a given clinical application.

Before design optimization algorithms were developed, a first guideline of the tube specifications selection has been proposed by Dupont et al. [Dupont et al., 2010a]. The objective of the general rules proposed in that work is to select the specifications of the tubes which satisfy two criteria: the ability to manipulate distal and proximal sections independently, and the ability to navigate through complex curved 3D paths. It is also important that the robot has the capacity to steer in tissues by exerting minimum lateral forces. Mainly, these rules explain how to select the stiffnesses and the curvatures of the tubes but in a general manner. The order of the robot sections is also defined in term of stiffness, curvature and extension (in descending order from the proximal to the distal section for the stiffnesses and in ascending order for the curvatures). The work provides only general rules and does not provide optimal definition of the tube parameters.

After this proposed general guideline, several algorithms have been proposed to optimize the tube dimensions. In order to reduce the complexity of the optimization problem, the number of optimization variables was restricted. In most of the works, the only considered parameters of tubes are the curvatures and the lengths. The number of tubes and their diameters are pre-selected and the only tube pre-shape considered is the circular form except the work of Gilbert et al. in [Gilbert and Webster, 2013] where the helical form is considered.

The three first design optimization algorithms have been introduced in the same period [Bedell et al., 2011] [Anor et al., 2011] [Burgner et al., 2011]. The work of Bedell et al. [Bedell et al., 2011] aims to define the optimal lengths and curvatures for the entire robot sections. However, the number of tubes and sections and their nature (variable or fixed curvature) and order are all preselected. In that work, the optimization problem is decomposed into two sub-problems: navigation optimization problem and manipulation optimization problem. The navigation part of the robot is used to position the manipulation part at the surgical site. Once the surgical site is reached by the manipulation part, the navigation part is held and only the manipulation part moves to accomplish the task (resection, injection, etc). The optimization algorithm used is Generalized Pattern Search (GPS) [Torzcon, 1997], and the cost function of the optimization problem is defined to achieve that: the tip position stays inside the de-

sired workspace limited by the anatomical constraints and the length and the curvatures of the sections are minimal. This work has served later to optimize the design of a robot used in intracardiac beating heart surgery in [Gosline et al., 2012b].

The second design optimization work has been proposed in [Anor et al., 2011] which addresses another medical application. From a given set of discrete target points, and knowing the anatomical constraints, the algorithm allows to find the simplest robot structure with the minimum required number of sections. It also calculates the length and the curvature of each section. All these criteria are formulated by a set of cost functions which are minimized using Pattern Search Algorithm (PSA) [Audet and Jr, 2003].

These two presented works require an inverse kinematics calculation to avoid the anatomical constraints in the optimization procedure. The inverse kinematic calculation for CTR is not trivial. It is complicated and time consuming as will be explained in the next section.

The third work has been introduced by Burgner et al. [Burgner et al., 2011], which allows to avoid the inverse kinematics calculation. Only the forward kinematics calculation is required. The application considered is the trans-nasal skull base surgery. After geometrical description of the workspace based on computed tomography (CT) images, the workspace is discretized to allow an evaluation of the robot within reachability. The reachability is evaluated based on the percentage of the reached volume in the desired workspace. It is quantified by the convex hull of the discrete points reached in the surgical workspace which is considered as a cost function of the optimization problem. The optimization variables are the lengths and the curvatures of the tubes, and the optimization algorithm uses Nonlinear Simplex Method.

The kinematic models used in the aforementioned works are simplified ones. In [Anor et al., 2011] the infinite stiffness model [Furusho et al., 2006] was used which neglects the interaction bending and torsion between tubes, and in both works of [Bedell et al., 2011] and [Burgner et al., 2011] the bending only model was used which neglects the tubes torsion. The advantage of using simplified models is to reduce the computation time and the complexity of the optimization problem formulation. This simplification comes at the cost of accuracy. For this reason, more accurate kinematic models have been used later in the design optimization algorithms.

Torres et al. [Torres et al., 2012] use a more complete kinematic model which considers the torsion of the tubes [Rucker and Webster, 2009]. Their work combines the issues of

finding the robot design space (lengths and curvatures) with the Rapidly-exploring Random Tree (RRT) [LaValle, 2006] motion planning algorithm (configuration search) and finding a design suitable to a given task without damage of the sensitive structure.

The limitation of the presented works so far is the fact that they only consider a discrete set of points to be reached. As an alternative, a volume-based approach was proposed by Burgner et al. in [Burgner et al., 2013a] which uses Nelder-Mead Simplex algorithm [Lagarias et al., 1998] to calculate the optimal tubes dimensions. This work offers more coverage of the surgical workspace compared to the previous works. The kinematic model used in this work is the torsionally compliant model described in [Rucker et al., 2010b].

All the aforementioned works consider only the case of piecewise-constant pre-curvatures. However, there are other options that could be explored. Junhyoung et al. [Ha et al., 2014] have proposed to utilize a variable pre-curvature of the tube along the length. This work shows that the obtained optimal curvatures allow to avoid bifurcation, which is defined in the end of the next chapter. The optimization problem is formulated by maximizing a cost function and studying its monotony.

In order to study the possibility of steering the robot in a follow-the-leader way, i.e. the shaft of the robot keeps its form once the tip progresses forward, Gilbert et al. [Gilbert and Webster, 2013] explored this concept for the first time and showed that this deploying manner is possible only for very specific tube pre-curvatures.

The helical form as another alternative of the tube pre-shaping has been proposed as well. The mathematical conditions of follow-the-leader deployment and of elastic stability have been formulated in that work. The two cases of curved and helical tubes have been studied. The extension of this work with experimental results have been presented in [Gilbert et al., 2015].

The latest work in design optimization [Bergeles et al., 2015] has introduced an optimization framework based on specifications of the task and the anatomical structure to generate the robot tube parameters. The elastic stability was considered in the optimization problem and the possibility of follow-the-leader insertion was studied. The optimization algorithm used is Nelder-Mead downhill simplex method [Nelder and Mead, 1965], and it was tested with two different clinical applications: intra-cardiac and neuro-surgery.

The works introduced in this section are summarized in Table.2.2.

Table 2.2 – Algorithms of tubes design optimization for RTC

Optimization Algorithm	Method used	Objective function	Optimization variables	Model used	Medical application
[Bedell et al., 2011]	GPS	<ul style="list-style-type: none"> • <i>Min</i>(lengths and curvatures of sections) • obstacles avoidance 	lengths and curvatures of sections	Torsion-free model	Intra-cardiac
[Anor et al., 2011]	PSA	<ul style="list-style-type: none"> • <i>Min</i>(lengths and curvatures of sections) • obstacles avoidance 	lengths and curvatures of sections	Infinite stiffness model	Neurology
[Burgner et al., 2011]	Nonlinear Simplex	<i>Min</i> (unreachable points)	Lengths and curvatures of the tubes	Torsion-free model	Skull base
[Torres et al., 2012]	RRT	Design and path ensuring the access to the desired workspace	Length and curvatures of the tubes	Torsionally compliant model	Lung
[Burgner et al., 2013a]	Nelder-Mead Simplex	<i>Max</i> (coverage of the desired workspace)	Lengths and curvatures of the tubes	Torsionally compliant model	Skull base
[Ha et al., 2014]	Study of the monotony	<i>Max</i> (elastic stability)	Curvatures in terms of the lengths	Torsionally compliant model	-
[Bergeles et al., 2015]	Nelder-Mead	<ul style="list-style-type: none"> • <i>Min</i>(Length and curvature of the robot) • elastic stability 	Curvatures and lengths of the tubes	Torsionally compliant model	-

2.3 Kinematic models of CTR

Since the concept of CTR was proposed in 2006 [Sears and Dupont, 2006] [Webster III et al., 2006], many research efforts have been made to study its kinematics behavior [D. Caleb

and R. J., 2009b]. In this section, the main existing kinematic models of CTR in literature are introduced. The mathematical formulation of each model will be detailed in the next chapter.

- The first model used considers the stiffness of the outer-most tube of the robot as infinite compared to all the inner tubes (Infinite Testiness Model) [Furusho et al., 2006]. The limitation of this model is that if the stiffness of the outermost tube is not high enough to satisfy the assumption then the accuracy of the model will degrade. In the case of very high stiffness of the outermost tube compared to the inners, the shape variation and the dexterity of the robot are limited.

otherwise, the shape variation is limited with less dexterity.

- Torsion-Free Model (TFM) takes into account the bending interaction between tubes, but the torsion of tubes is neglected. As the tubes are made of Nitinol, the torsion impact on the rotation angles deformation of the tubes can be significant in some cases which affects the estimation of the shape [Sears and Dupont, 2006].

- Kinematics modelling of CTR is improved by including the transmissional torsion between actuators and the first curved link in the Transmissional Torsion Model (TTM) which reduces the error caused by torsion phenomenon in the straight part, but the torsion in the curved part of the tubes is neglected [Webster et al., 2008] [R. J. Webster et al., 2009].

- The Torsionally Compliant Model (TCM) is more accurate than the prior works, which is based on Cosserat Rod Theory (Special Cosserat Rod Equilibrium Model) [Cosserat and Cosserat, 1909][Antman, 1995]. Two approaches have been used to calculate the forward kinematic model: the Newton equilibrium wrench in [Dupont et al., 2010a] [Rucker et al., 2010b] and the Euler-Lagrange energy minimization in [Dupont et al., 2009] [Rucker et al., 2010a]. The torsions of the straight and curved parts of the tubes are both considered in the model, but the latter is described by a second order nonlinear differential equation causing problems of boundary conditions and heavy computational burden in real-time. Another limitation is that the frictions are not included in this model. For this reason, this model was extended by considering the effect of the friction between tubes in the kinemato-static formulation [Lock and Dupont, 2011].

- In order to reduce the computation time, Xu et al. in [Xu and Patel, 2012] reformulate the torsionally compliant model and linearize it, then they propose to use a force sensor to solve the unknown initial conditions problem: the torsion efforts of the tubes at the base are

unknown (more details are provided in the next chapter). However, the linearization may reduce the accuracy and the force sensors required for each tube are cumbersome.

- A model which considers the deflection of the robot tip in interaction with the environment has been developed in [Mahvash and Dupont, 2011] and used for stiffness control. This model is also based on Cosserat Rod model.

2.4 Motion planning

In order to orient the robot to a specific target with the presence of obstacles (sensitive structures), a motion planner based on constrained environment is required. This planner calculates the optimal actuation sequence which allows the robot tip to move to the desired position. The calculation of the optimal actuation sequence is highly dependent on the robot kinematics. Motion planning algorithms for CTR have been developed and evolved with the kinematics evolution of CTRs and the algorithms have been dedicated to different medical applications. In this section, existing motion planning algorithms for CTRs are presented, and the specification of each work is discussed.

The first work in motion planning of CTR has been introduced by Lyons et al. [Lyons et al., 2009]. This algorithm calculates the optimal translations and rotations of the tubes which guide the robot to reach its target with avoidance of the anatomical obstacles (spherical obstacles). The desired translations and rotations are calculated based on the target position, the initial tip position and orientation, and the geometric representation of the obstacles. The motion planning problem is formulated as a constrained nonlinear optimization problem which is then transformed into a sequence of unconstrained optimization problems using penalty method. The cost function formulates the obstacles avoidance and the target reaching with constraints imposed on the orientation angles and section length. This work utilizes a basic kinematic model which neglects the beam mechanics [Furusho et al., 2006].

In [Lyons et al., 2010], another optimization-based planning algorithm has been proposed. It computes the configuration of the robot which navigates through tubular structures to reach a target. This work is an extension of the previous one by providing two main improvements which are the calculation of the robot shape by minimizing the interaction energy between the tubes, and the consideration of the motion through tubular structure rather than motion with

avoiding spherical obstacles which is a more realistic scenario. The inputs of the algorithm are similar to the previous work. However, the kinematic model used in the formulation of the optimization problem is a beam mechanics model [R. J. Webster et al., 2009] which is more accurate compared to the previous one. This algorithm has been simulated using extracted human CT scan of the lung bronchi for the lung biopsy navigation scenario.

In [Torres and Alterovitz, 2011], Torres et al. have used the Rapidly-Exploring Roadmap (RRM) [Alterovitz et al., May 2011] to calculate the control inputs that guide the robot to the target with minimal collision probability. Unlike previous works, this motion planner uses TCM model which considers the bending and the torsion of the tubes in both straight and curved parts. The clinical application addressed in this work is neurosurgery.

Another work which solves the combined problem of design optimization with motion planing has already been introduced in the previous section [Torres et al., 2012].

In order to avoid the elastic instability which may cause problems of control, a specific motion planner has been developed by Bergeles et al. [Bergeles and Dupont, 2013]. This algorithm aims to find an elastically stable path respecting the anatomical constraints for robots which exhibit only local stability using RRT* algorithm [Karaman and Frazzoli, 2010].

The latest work so far [Torres et al., 2014] in path planning for CTR uses TCM model and enables a collision-free navigation of the robot tip and shaft. The proposed approach combines off-line pre-computation of a collision-free road-map with on-line position control. The road-map is built using modified Rapidly Exploring Random Graph (RRG) [Karaman and Frazzoli, 2011]. The medical scenario of this work is neuro-surgery via a nasal access. All these works are summarized in the following Table.2.3.

2.5 Control of CTR

The complexity and hence high computation time of the CTR forward and inverse kinematics makes its real-time control difficult. It is obvious that the control performance depends on the accuracy of the kinematic model used. For CTR, the precision of the direct and inverse kinematics modelling is inversely proportional to the total length of the robot [Rucker, 2011]. The existing works in control of CTR are presented in this section and are summarized in Table 2.4 specifying: the control strategy used; the robot length (the inner-most tube length

Table 2.3 – Path planing algorithms for CTRs

Planner	Method used	Inputs of the algorithm	Outputs of the algorithm	Model used	Medical application
[Lyons et al., 2009]	Constrained nonlinear programming	<ul style="list-style-type: none"> • Target position • Initial pose • Obstacles 	Translations and rotations of the tubes	Infinite stiffness model	-
[Lyons et al., 2010]	Constrained nonlinear programming	<ul style="list-style-type: none"> • Desired position • Initial pose • Obstacles 	Translations and rotations of the tubes	Bending only model	lungs
[Torres and Alterovitz, 2011]	RRM	<ul style="list-style-type: none"> • Desired position • Initial pose • Obstacles 	Translations and rotations of the tubes	Bending and torsion model	Skull-base surgery
[Torres et al., 2012]	RRT	<ul style="list-style-type: none"> • Design of tubes • Initial configuration • Number of joint samples • Obstacles 	Vertices and edges of the graph constituting the trajectory	Bending and torsion model	Lung
[Bergeles and Dupont, 2013]	RRT*	<ul style="list-style-type: none"> • Initial configuration • Number of samples • Obstacles 	A sequence of stable configurations	Bending and torsion Model	Lung
[Torres et al., 2014]	RRG	<ul style="list-style-type: none"> • New actual and desired positions at each iteration • Obstacles 	Translations and rotations allowing obstacles avoidance of the whole robot	Bending and torsion model	Lung

is considered as the robot length); the implementation in real-time and the cycle frequency. The performances of each architecture in Table 2.4 are evaluated using the Root Mean Square Error (RMS).

In 2009, Webster et al. [Webster et al., 2009] have proposed to control the position of

CTR through visual servoing. In this work, one rotation joint has been fixed, which reduces the dimension of the Jacobian matrix and makes it square as only three actuators have been used: two translations and one rotation. The inverse of the Jacobian matrix has been used to transform the Cartesian errors to the joint errors.

Dupont et al. in [Dupont et al., 2010b] and [Dupont et al., 2010a] have proposed a teleoperated control architecture of the position and orientation angle of the CTR tip. The Cartesian target given by the manipulator from the master side is interpreted to joint target through its inverse kinematic model. Because of the kinematics complexity, and consequently its heavy calculation requirement, an offline approximation has been carried out. A lookup table containing the joint variables and their corresponding Cartesian poses has been used to identify a Fourier series function which models the forward kinematic model. The inverse kinematic model is then a root-finding problem of the approximation function. It is solved using Gauss-Newton algorithm. The control at the slave level is ensured by a PID controller in the joint space, which makes the control performances sensitive and highly depending on the kinematics modelling errors. The RMS error of the forward kinematic model used that works is about $4mm$. Moreover, the approximation function affects the forward kinematic modelling accuracy and consequently the inverse model.

The stiffness control has been applied to control the contact with a soft environment by Mahvash et al. [Mahvash and Dupont, 2011]. The system is teleoperated and the master controller calculates the desired forces to be exerted by the tip (3 DOFs). This calculation is based on the error between the feedback tip position and the interpretation of the teleoperator hand motion. Through a deflection model, the desired forces are used to calculate the desired joint positions. The joint control is then done at the slave level using a PD controller.

The reference position in [Burgner et al., 2011] and [Burgner et al., 2014] is obtained by interpreting the hand motion of the teleoperator at the master side. The desired joint positions corresponding to the desired Cartesian position are obtained through the inverse kinematics calculation. The approach used for the inverse kinematics calculation is the damped least square [Wampler, 1986] of the Jacobian matrix. Based on this method, the joint velocities obtained ensure the avoidance of the singular configurations.

Sliding mode for CTR position control has been used in [Comber et al., 2012]. This control architecture provides good control performances, but it has been studied at the level of

joint tracking (rotations and translations). The control performances of the robot tip Cartesian position has not been evaluated in this work.

The fast kinematic model proposed in [Xu and Patel, 2012] has been derived to calculate the differential kinematic model. The obtained Jacobian matrix has been used for an inverse kinematics control of CTR in [Xu et al., 2013]. Later, this model has been improved in order to control the position of CTR under external loads [Xu et al., 2014].

In order to avoid elastically instable configurations and the joint limits (tube translation limits), Azimian et al. in [Azimian et al., 2014] have proposed an inverse kinematic controller under inequality constraints. All the aforementioned works are summarized in Table 2.4.

Table 2.4 – Control architectures of RTC.

Controller	Control law	Teleoperated	L(mm)	R-T	F_{cycle} (Hz)	RMS (mm)
[Webster et al., 2009]	IKC V. servoing	No	128,6	Yes	15	0,674
[Dupont et al., 2010b]	PID	Yes	200	Yes	1000	4,2
[Mahvash and Dupont, 2011]	Force control, PD	Yes	150	Yes	1000	-
[Burgner et al., 2014]	Inverse kinematic control	Yes	275	Yes	400	1.5
[Comber et al., 2012]	Sliding mode	No	-	-	-	-
[Xu et al., 2013]	Inverse kinematic control	No	400	Yes	-	3,86
[Xu et al., 2014]	Under external loads	No	303	Yes	-	1,4
[Azimian et al., 2014]	IKC under constraints	No	312	Yes	1000	-

2.6 Conclusion

This chapter has summarized the main works in literature and shown the directions of CTR evolution. Deep background on kinematics modelling is detailed in the next chapter. More discussions about existing works in tubes design and control of CTR are also necessary before introducing the two main contributions of this thesis and therefore are provided in the introductions of Chapter 4 and 5.

Kinematic Modelling of Concentric Tube Robot

Preamble

The evolution of CTR kinematic modelling has been introduced briefly in the previous chapter. Since kinematics serves as the basis for CTR design and control, in this chapter the mathematical frameworks of the most oftenly used forward, differential, and inverse kinematic models are presented in detail for the case of two tubes. The pre-shape of the tubes considered is the most oftenly used one which has a straight part followed by a planar constant curved part. Bifurcation, as a special phenomenon for CTR, presents big challenge for motion planning and implementation safety and is presented in the end of this chapter.

Contents

3.1	Introduction	36
3.2	Forward kinematic model of concentric tube robot	36
3.3	Differential kinematic model of concentric tube robot	48
3.4	Inverse kinematic model	50
3.5	Bifurcation phenomenon	52
3.6	Conclusion	54

3.1 Introduction

The kinematic modelling is required for both tube design optimization and control. For CTR, the forward kinematic model is a mapping from the tubes translations and rotations to the tip pose passing by a set of sampling points from the robot shaft. The inverse kinematic model is to find the rotations and translations of the tubes given a pose in task space. The differential kinematic model defines the relation between the spatial tip velocities and the rotations and translations velocities of the tubes thanks to the Jacobian matrix.

The forward kinematic model is used for the reachability and elastic stability evaluation in the Chapter 4 which discusses the tubes design optimization. The differential kinematic model is also employed in the task-space control scheme proposed in Chapter 5. The kinematic modelling developed in this chapter is therefore to be used in the next two chapters. The CTR considered in Chapter 4 includes three tubes which are required to ensure the navigation and the surgical workspace coverage. In Chapter 5, two-tube CTR is used to validate the proposed controller through simulation. The principal of kinematic modelling is similar for CTRs with two tubes and three tubes. The difference lies in the fact that the mathematical formulation complexity is higher in the case of three tubes. For clarity of presentation and ease of understanding, the case of two tubes with a straight and a curved part of each tube is considered in all the kinematics modelling presented in this chapter.

3.2 Forward kinematic model of concentric tube robot

In this section, the existing forward kinematic models for CTR with their mechanics principles used are introduced starting from the model neglecting interactions between tubes to the model including bending and torsion interactions between tubes. In this order, the modelling accuracy, formulation complexity and calculation time increase accordingly.

3.2.1 Infinite stiffness model

The simplest and least accurate forward kinematic model of CTR was proposed in [Furusho et al., 2005] and [Smith et al., 2006] and assumes that the bending and the torsion due to the interactions between tubes are neglected. The robot arm is split into a set of constant

curvature sections. The geometrical shape of a section is assumed to be identical to the pre-shape of the outer-most tube surrounding it regardless the number and the pre-shapes of the inner tubes. As it has been explained in [R. J. Webster and Jones, 2010] and illustrated in

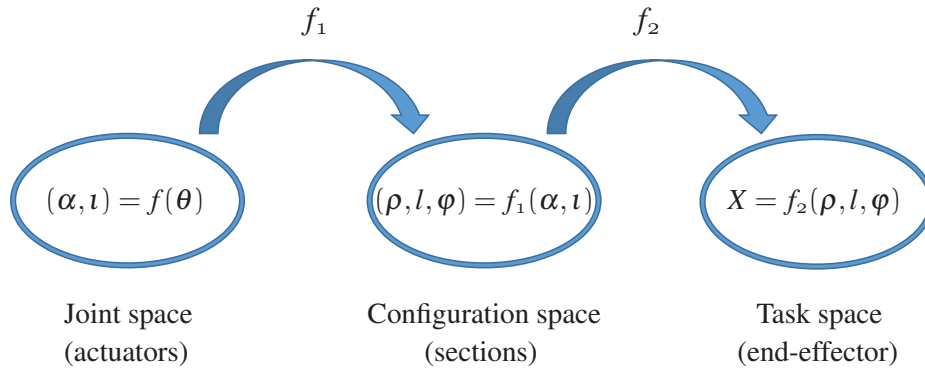


Figure 3.1 – Two mappings defining the forward kinematic model: f_1 from the joint space (α_i, ι_i) to the configuration space (ρ_j, l_j, φ_j) and f_2 from the configuration space to the task space (tip pose X). This figure is adapted from [R. J. Webster and Jones, 2010].

Figure 3.1, two mappings are required to calculate the pose of the end-effector of the CTR arm.

- The first mapping f_1 is to split the robot into a set of constant curvature sections, define the dominant tube in each section, and then to calculate the configuration parameters of each section. The configuration parameters of a section j are: the curvature ρ_j ; the length l_j ; and the orientation angle φ_j ($j = 1, 2, \dots, m$ with m being the number of sections) with respect to the previous section $j - 1$. They are calculated in terms of the joint parameters (rotations α_i and translations ι_i , $i = 1, 2, \dots, n$ with n is the number of tubes) which depend directly on the actuator angles θ_k ($k = 1, 2, \dots, 2n$). The number of sections m and their lengths l_j are defined in terms of the tubes translations ι_i , the lengths of straight parts L_{S_i} and curved parts L_{C_i} of the tubes. The orientation angle φ_j of a section j is obtained by subtraction of the dominant tube rotation angle from the dominant tube rotation angle of the previous section $j - 1$.

Consider the case of two tubes inserted concentrically with the configuration showed in figure 3.2. The limits of the sections are defined by the start and the end points of the straight and the curved parts (L_{S_i}, L_{C_i}) of the dominant tube at each section. The number of sections

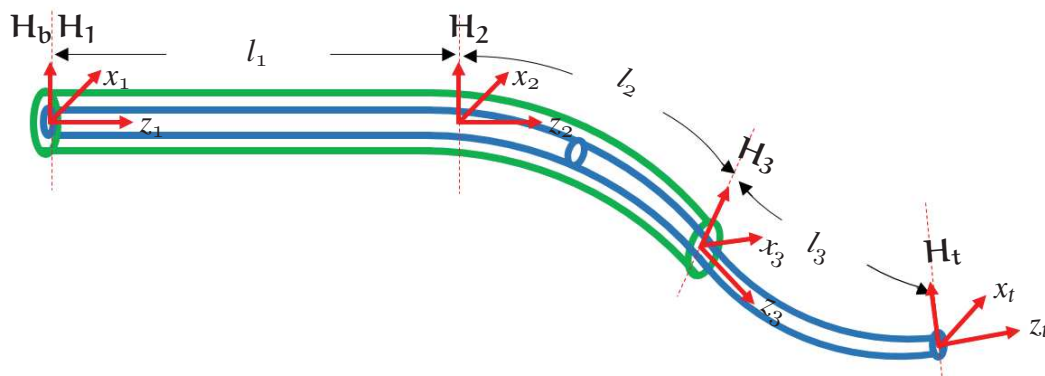


Figure 3.2 – Two-tube CTR with three constant curvature sections, from the base to the tip: the first section of length l_1 delimited by the frame \mathbf{H}_1 (attached to the base of the outer tube) and by the frame \mathbf{H}_2 (attached to the distal extremity of the straight part of the outer tube) is composed of two straight tubes; the second section of length l_2 delimited by the frame \mathbf{H}_2 and the frame \mathbf{H}_3 (attached to the distal extremity of the curved part of the outer tube) is composed of a curved dominant outer tube and an inner tube with a straight and a curved part; the third section of length l_3 is composed of only one curved tube and is delimited by the frames \mathbf{H}_3 and \mathbf{H}_t which is attached to the tip.

is then three: the first section is dominated by the straight part of the outer-tube. The second section is dominated by the curved part of the outer-tube, and the last one is composed of only one inner-tube. The frames \mathbf{H}_j are attached to the section bases and the base frame \mathbf{H}_b is attached to the base of the outer tube with its Z axis coaxial to the tube centerline. This \mathbf{H}_b frame is coincident with the first moving frame \mathbf{H}_1 when the rotation angle α_1 is equal to zero. \mathbf{H}_2 is attached to the distal extremity of the straight part L_{S_1} which corresponds to the base of the second section and \mathbf{H}_3 is attached to the distal extremity of the curved part L_{C_1} which corresponds to the base of the third section. The Z axes of all the frames are coaxial to the robot shaft centerline.

The lengths of the sections are calculated as follows:

$$\begin{cases} l_1 = L_{S1} \\ l_2 = L_{C1} \\ l_3 = (L_{S2} + L_{C2}) - (L_{S1} + L_{C1}) + (l_2 - l_1) \end{cases} \quad (3.1)$$

The tubes are numerated from the outer-most to the inner-most as shown in Figure.3.2.

The orientation angles of the three sections are given by:

$$\begin{cases} \varphi_1 = \alpha_1 \\ \varphi_2 = 0 \\ \varphi_3 = \alpha_2 - \alpha_1 \end{cases} \quad (3.2)$$

where α_i is the Z axial rotation angle of the tube i which is assumed to be constant along the whole tube length since the torsion effect is neglected.

The curvature of a section is equal to the pre-cuvature of the outer-most tube present in it:

$$\begin{cases} \rho_1 = 0 \\ \rho_2 = 1/r_1 \\ \rho_3 = 1/r_2 \end{cases} \quad (3.3)$$

where ρ_j is the curvature of the section j and r_i is the curvature radius of the tube i .

- The second mapping f_2 is to use the configuration parameters (l_j, φ_j, ρ_j) to calculate the homogeneous transformation matrices between the section frames. The position and the orientation of the end effector are then obtained in the base frame by a successive product of these matrices.

The first mapping expressed by the homogeneous matrix ${}^b\mathbf{H}_1 \in SE(3)$ ($SE(3)$ is the special Euclidean group) is then a pure rotation (Rot_z) around the Z axis of the base frame given by:

$${}^b\mathbf{H}_1 = \begin{bmatrix} & & & 0 \\ & [Rot_z(\varphi_1)] & & 0 \\ & & & 0 \\ 0 & 0 & 0 & 1 \end{bmatrix} \quad (3.4)$$

For the first straight section, the mapping from the frame H_1 to the frame H_2 attached to the base of the second section is given by a linear translation along the Z axis with a quantity equal to the section length. The ${}^1H_2 \in SE(3)$ homogeneous matrix expressing the mapping from (H_1) the base of the first section to (H_2) the base of the second section is given by:

$${}^1H_2 = \begin{bmatrix} 1 & 0 & 0 & 0 \\ 0 & 1 & 0 & 0 \\ 0 & 0 & 1 & l_1 \\ 0 & 0 & 0 & 1 \end{bmatrix} \quad (3.5)$$

In the case of a curved section, the mapping from its base to its distal extremity is defined by a rotation φ around the Z axis of the base frame followed by a second transformation as shown in Figure 3.3. The second transformation defines the coordinates of a point from the planar section of radius r in the frame (X', Y', Z') , then the translation between the former and the section base frame is considered. When the rotation $\varphi = 0$, the coordinates of the distal extremity point as can be seen from the Figure.3.3 are: $(0, r \cos(l\rho) - r, r \sin(l\rho))$ and the orientation of the frame attached to distal extremity point of the section is expressed by a rotation $l\rho$ around X where the curvature $\rho = \frac{1}{r}$ and l is the section length.

The mapping 2H_3 therefore is expressed as follows:

$${}^2H_3 = \begin{bmatrix} & & & 0 \\ & [Rot_z(\varphi_2)] & & 0 \\ & & & 0 \\ 0 & 0 & 0 & 1 \end{bmatrix} \begin{bmatrix} & & & 0 \\ [Rot_x(l_2\rho_2)] & \frac{(\cos(l_2\rho_2)-1)}{\rho_2} & & \\ & \frac{\sin(l_2\rho_2)}{\rho_2} & & \\ 0 & 0 & 0 & 1 \end{bmatrix} \quad (3.6)$$

Similarly for the last section we obtain:

$${}^3H_t = \begin{bmatrix} & & & 0 \\ & [Rot_z(\varphi_3)] & & 0 \\ & & & 0 \\ 0 & 0 & 0 & 1 \end{bmatrix} \begin{bmatrix} & & & 0 \\ [Rot_x(l_3\rho_3)] & \frac{(\cos(l_3\rho_3)-1)}{\rho_3} & & \\ & \frac{\sin(l_3\rho_3)}{\rho_3} & & \\ 0 & 0 & 0 & 1 \end{bmatrix} \quad (3.7)$$

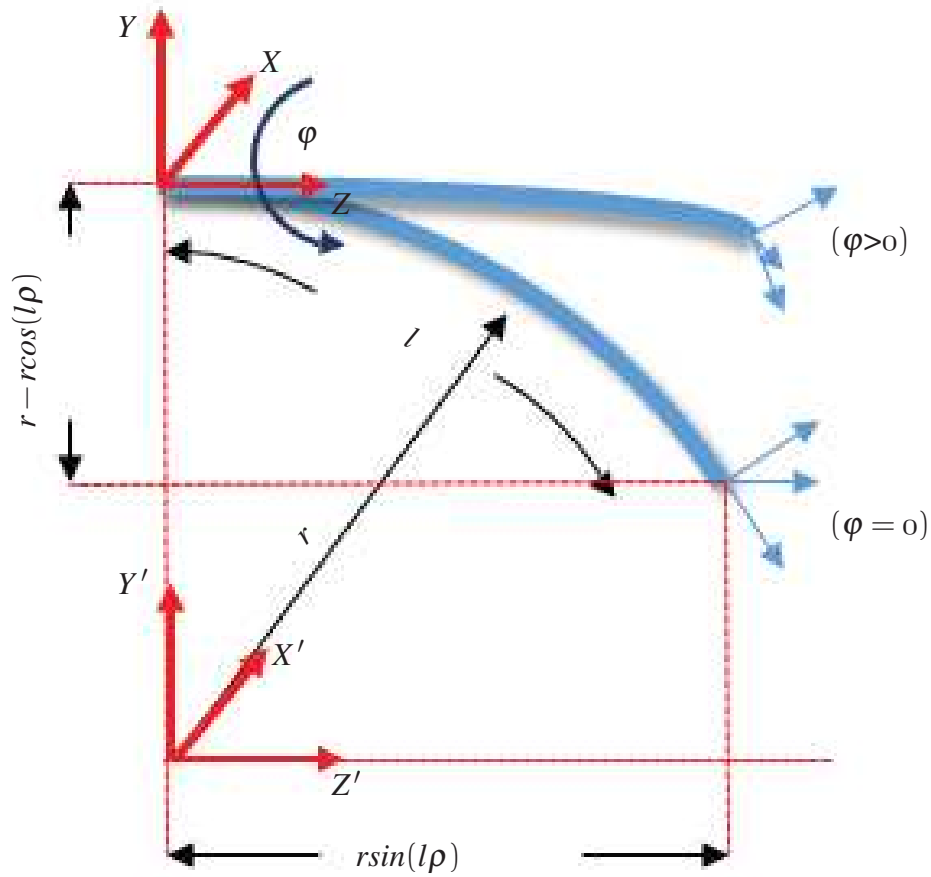


Figure 3.3 – Section geometry, adapted from [R. J. Webster and Jones, 2010].

The forward kinematic model is then given by the product of these transformation matrices in this order:

$${}^b\mathbf{H}_t = {}^b\mathbf{H}_1 {}^1\mathbf{H}_2 {}^2\mathbf{H}_3 {}^3\mathbf{H}_t = \prod_j^{j-1} \mathbf{H}_j \quad (3.8)$$

3.2.2 Bending model

The model proposed in [R. J. Webster et al., 2009] and in [Sears and Dupont, 2006] takes into consideration the bending interaction between tubes. This bending depends on the tubes pre-curvatures, their stiffnesses, and their rotation angles. The outer-most tube is not considered as the dominant tube in terms of stiffness and all the existing tubes in one section are used to calculate its overall curvature and planar angle. Consequently, the number of sections increases compared to the previous model. In our case of study, the section 2 in figure 3.2 is split into two sections as the pre-curvature of the inner tube changes from straight to curved part, and the bending interaction between tubes is considered rather than considering the outer tube as the dominant stiffness tube in the previous model. The sections are then delimited by the straight and curved parts of all the tubes, as shown in figure 3.4.

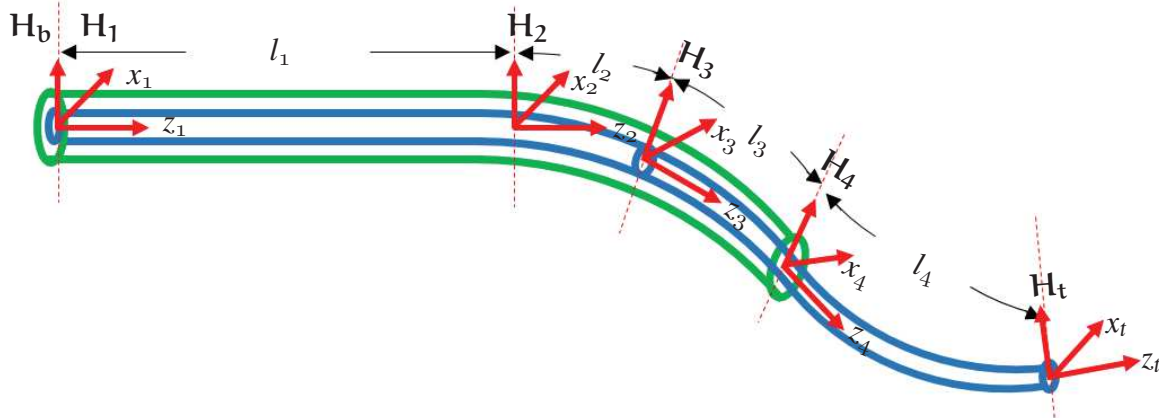


Figure 3.4 – Two-tube CTR with four constant curvature sections, from the base to the tip: the first section is composed of two straight tubes; the second section is composed of an outer curved tube and an inner straight tube; the third section is composed by two curved tubes and the fourth section is a single curved tube.

The total number of sections is four, and for each section j three parameters are required to define the homogeneous transformation matrix between its distal and proximal extremity.

These parameters are the length l_j , the curvature ρ_j , and the orientation angle φ_j with respect to the previous section $j-1$. The lengths of the sections are expressed by:

$$\begin{cases} l_1 = L_{S1} \\ l_2 = (L_{S2} + \iota_2) - (L_{S1} + \iota_1) \\ l_3 = (L_{S1} + L_{C1} + \iota_1) - (L_{S2} + \iota_2) \\ l_4 = (L_{S2} + L_{C2} + \iota_2) - (L_{S1} + L_{C1} + \iota_1) \end{cases} \quad (3.9)$$

For the orientation angle and curvature of a section j , they are obtained after decomposition of the section curvature into two coordinates in the (X, Y) plan [Webster III, 2007]. These (X, Y) coordinates, denoted by (χ_j, v_j) , are expressed in the base frame of each section. They are obtained from the Bernoulli-Euler beam mechanics and are given by:

$$\chi_j = \frac{\sum_i E_i I_i \bar{\rho}_{i,j} \cos \alpha_{i,j}}{\sum_i E_i I_i}, \quad v_j = \frac{\sum_i E_i I_i \bar{\rho}_{i,j} \sin \alpha_{i,j}}{\sum_i E_i I_i} \quad (3.10)$$

where E_i is the modulus of elasticity (Young's modulus), I_i is the second moment of area and the $\bar{\rho}_{i,j}$ is the pre-curvature of the tube i in the section j . The limits of the sums are defined by the number of the tubes present in the section. Then, the orientation angle and curvature are calculated by using these (χ_j, v_j) coordinates :

$$\varphi_j = \tan^{-1} \left(\frac{v_j}{\chi_j} \right) \quad \rho_j = \sqrt{\chi_j^2 + v_j^2} \quad (3.11)$$

For each section j , the curvature does not vary along the whole section. The transformation matrix of a section defining the mapping from its distal to its proximal extremity expressed in the proximal frame is given by the following relationship:

$${}^{j-1}\mathbf{H}_j = \begin{bmatrix} & & & 0 \\ & [Rot_z(\varphi_j - \varphi_{j-1})] & & 0 \\ & & & 0 \\ 0 & 0 & 0 & 1 \end{bmatrix} \begin{bmatrix} & & & 0 \\ [Rot_x(l_j \rho_j)] & & & \frac{(\cos(l_j \rho_j) - 1)}{\rho_j} \\ & & & \frac{\sin(l_j \rho_j)}{\rho_j} \\ & & & 1 \end{bmatrix} \quad (3.12)$$

and the pose of the tip expressed in the base frame is given by the product of these transformations:

$${}^b\mathbf{H}_t = \prod_j^{j-1} \mathbf{H}_j \quad (3.13)$$

where j variates from the base to the tip to include all the sections.

3.2.3 Straight torsion model

The flexibility of the tubes' material leads to torsion problem of the tubes which affects their rotation angles and makes them change from a section to another. In the model of [R. J. Webster et al., 2009], the tube torsions are included in the first straight part of the tubes before the first curvature. This model allows to calculate the rotation angles β_i of all the tubes ($i = 1 \dots n$) after the torsion deformation.

In the considered case study, the angles β_i represent the rotations of the tubes at the distal extremity of the first section (or the base of the second section). The quantity of the elastic energy developed during the tubes interactions is due to their torsions and flexures. The bending energy Υ_{bend} stored in a given section j is the sum of the bending energy along the X direction ($\Upsilon_{x,j}$) and the bending energy along the Y direction ($\Upsilon_{y,j}$):

$$\Upsilon_{bend_j} = \Upsilon_{x,j} + \Upsilon_{y,j}, \quad (3.14)$$

where:

$$\Upsilon_{x,j} = \frac{\sum E_i I_i l_j}{2} (\chi_j - \bar{\rho}_{i,j} \cos \beta_i)^2, \quad \Upsilon_{y,j} = \frac{\sum E_i I_i l_j}{2} (v_j - \bar{\rho}_{i,j} \sin \beta_i)^2 \quad (3.15)$$

As has been previously explained, the only torsion energy included in the elastic energy is the one before the distal extremity of the first straight section given by:

$$\Upsilon_{tor} = \frac{\sum G_n J_n}{2L_i} (\alpha_i - \beta_i)^2 \quad (3.16)$$

where L_i is the length from the tube base to the end of the first section, G_i is the shear modulus and J_i is the polar moment of inertia. The total elastic energy is the sum of the torsion energy and the bending energy of all sections:

$$Y = Y_{bend} + Y_{tor}. \quad (3.17)$$

For the torsion energy of the present case study, it is given by:

$$Y_{tor} = \frac{G_1 J_1}{2L_1} (\alpha_1 - \beta_1)^2 + \frac{G_2 J_2}{2L_2} (\alpha_2 - \beta_2)^2 \quad (3.18)$$

By applying the energy calculation (3.15) for the second and third section yields:

$$Y_{bend} = l_2 \bar{\rho}_1^2 \frac{E_1 I_1 E_2 I_2}{2(E_1 I_1 + E_2 I_2)} + \frac{E_1 I_1 E_2 I_2 l_3}{2(E_1 I_1 + E_2 I_2)} (\bar{\rho}_1^2 + \bar{\rho}_2^2 - 2\bar{\rho}_1 \bar{\rho}_2 \cos(\beta_1 - \beta_2)) \quad (3.19)$$

which expresses the total bending energy stored in the robot.

Once the tubes interact with each other, the resulting shape is found such that the elastic energy Y is locally minimal. The angles β_i are calculated at the equilibrium by setting the gradient ∇Y with respect to β_i to zero which leads to the following system:

$$\begin{cases} -\frac{G_1 J_1}{L_1} (\alpha_1 - \beta_1) + \frac{\bar{\rho}_1 \bar{\rho}_2 E_1 I_1 E_2 I_2}{E_1 I_1 + E_2 I_2} l_3 \sin(\beta_1 - \beta_2) = 0 \\ -\frac{G_2 J_2}{L_2} (\alpha_2 - \beta_2) - \frac{\bar{\rho}_1 \bar{\rho}_2 E_1 I_1 E_2 I_2}{E_1 I_1 + E_2 I_2} l_3 \sin(\beta_1 - \beta_2) = 0 \end{cases} \quad (3.20)$$

This system can be solved using a variety of numerical solvers. The one that has been used in this work is the Newton-Raphson algorithm [Doron, 2010]. After obtaining the angles β_i , they are used in (3.10) and (3.11) to calculate the resulting curvatures and orientation angles of each section after including the torsion as has been explained earlier. Later, the obtained curvatures and orientation angles are used in the formula (3.12) for each section, and the pose of the tip is calculated using the product (3.13).

3.2.4 Torsionally compliant model

In order to improve the accuracy of the kinematics, the torsion effect in both straight and curved parts of the tubes has been included in the models introduced in [Dupont et al., 2009]

[Rucker et al., 2010a] [Dupont et al., 2010a] [Rucker et al., 2010b] instead of considering it only in the straight part in the previous model. The model proposed in [Dupont et al., 2010a] is derived from the special Cosserat rod model [Cosserat and Cosserat, 1909]. The curvature $\rho_i \in \mathbb{R}^3$ of a tube i has three components $(\rho_{i,x}, \rho_{i,y}, \rho_{i,z})$ along (X, Y, Z) axes where the first two are due to the bending, and the last one is due to the torsion. For previous models, the curvatures are defined section by section and assumed to be constant along the whole section. However, for this model, the curvatures vary continuously according to the robot length $s \in [0, L]$. As torsion is considered, the rotation angles $\alpha_i(s)$ of the tubes depend on the distance s along the robot shaft from the robot base. The relative twist angle between the two tubes is defined by:

$$\gamma(s) = \alpha_2(s) - \alpha_1(s) \quad (3.21)$$

The bending curvature components $(\rho_{1,x}, \rho_{1,y})$ and $(\rho_{2,x}, \rho_{2,y})$ of the first and second tube respectively are calculated after defining the equilibrium moment conditions and ensuring the same bending shape of tubes once assembled. After the mathematical formulation of these conditions presented in [Dupont et al., 2010a], it leads to:

$$\begin{aligned} \rho_1|_{x,y} &= (Rot_z(\gamma(s))\rho_2)|_{x,y} \\ \rho_2|_{x,y} &= (K_1 + K_2)^{-1} (Rot_z^T(\gamma(s)K_1\bar{\rho}_1(s) + K_2\bar{\rho}_2(s))|_{x,y} \end{aligned} \quad (3.22)$$

where $\rho_i|_{x,y}$ are the (X, Y) curvature components of the tube i and

$$K_i = \text{diag}(K_{i,x}, K_{i,y}, K_{i,z}) = \begin{bmatrix} E_i I_i & 0 & 0 \\ 0 & E_i I_i & 0 \\ 0 & 0 & G_i J_i \end{bmatrix} \quad (3.23)$$

is the stiffness tensor of the tube i .

The torsion curvature components are obtained after including the torsional twist, satisfying the equilibrium of the torsional moments, and using the equilibrium equation of the special Cosserat rod model [Antman, 1995].

The development of these conditions yields:

$$\begin{aligned}\rho_{1,z} &= -\frac{K_{2,z}}{K_{1,z}}\rho_{2,z} \\ \frac{d\rho_{2,z}}{ds} &= \frac{K_{2,xy}}{K_{2,z}}(\bar{\rho}_{2,y}\rho_{2,x} - \bar{\rho}_{2,x}\rho_{2,y})\end{aligned}\quad (3.24)$$

with $K_{2,xy} = K_{2,x} = K_{2,y}$. The twist rate is expressed by:

$$\dot{\gamma} = \rho_{2,z} - \rho_{1,z} \quad (3.25)$$

The resulting equations (3.22), (3.24), and (3.25) form a nonlinear differential equation system with $(\gamma, \rho_{2,z})$ as integration variables.

At the robot base $s = 0$, γ is known as it is calculated from (3.21), however, $\rho_{2,z}$ is unknown. At the distal extremity of the robot $s = L$, the torsion curvature is zero, which means $\rho_{2,z}$ is zero. The system is then a nonlinear differential equation with boundary conditions. The `bvp4c` matlab function allows to solve this kind of systems, which integrates from the initial limit to the final one and then integrates back and repeats this go-and-back integration until both initial and final conditions are satisfied. Once this system is integrated, the obtained curvatures are used to define the robot shape. The curvatures are then integrated analogously to the twist velocity integration by preserving the group structure on $SE(3)$. A variety of methods are presented in [Park and Chung, 2005].

A less complicated alternative method is to approximate the robot shape by a set of small constant curvature sections of length Δs , then it is integrated using the Rodrigues' formula.

Consider \mathbf{H} as an homogeneous matrix expressing the mapping between two frames and \mathbf{V} is the twist between them. Recall the following well-known relationship in kinematics of rigid body [Murray et al., 1994]:

$$[\mathbf{V}] = \mathbf{H}^{-1}\dot{\mathbf{H}} \quad (3.26)$$

where the operator $[\cdot]$ denotes the mapping from \mathbb{R}^6 to $se(3)$ ($se(3)$ is the Lie Algebra of $SE(3)$ [Park and Chung, 2005]).

Neglecting the elongation of the tubes, the reference twist is given by:

$$\xi(\mathbf{s}) = \left[\begin{bmatrix} 0 & 0 & 1 \\ \rho(s)^T \end{bmatrix} \right]^T \quad (3.27)$$

Analogous to (3.26), the following is obtained:

$$[\xi(\mathbf{s})] = \mathbf{H}^{-1}(\mathbf{s})\dot{\mathbf{H}}(\mathbf{s}) \quad (3.28)$$

As the curvatures $\rho(s)$ have already been calculated after integrating the previous system, and considering these curvatures constant at each sampling section of length Δs , the robot shape can be obtained recursively by the Rodrigues' formula:

$$\mathbf{H}(\mathbf{s}) = \mathbf{H}(\mathbf{s} - \Delta \mathbf{s}) \expm([\xi(\mathbf{s})]\Delta \mathbf{s}) \quad (3.29)$$

where *expm* is a matlab function calculating the exponential of a matrix.

3.3 Differential kinematic model of concentric tube robot

In this section, the calculations of the differential kinematic model ending model, straight torsion model, and torsionally compliant model are presented in details. For a constant curvature section j of the robot, the spacial velocity vector $\mathbf{V}_j \in \mathbb{R}^6$ of its distal extremity with respect to its base expressed in its frame base can be obtained by integrating the following equation:

$$[\mathbf{V}_j] = \dot{\mathbf{H}}\mathbf{H}^{-1} \quad (3.30)$$

Substituting the homogeneous matrix \mathbf{H} by the general expression (3.12) in equation (3.30) yields:

$$\left\{ \begin{array}{l} \mathbf{V}_j = \begin{bmatrix} \rho' \sin(\varphi_j - \varphi_{j-1}) (\cos(\rho l) - 1) / \rho^2 \\ \rho' \cos(\varphi_j - \varphi_{j-1}) (\cos(\rho l) - 1) / \rho^2 \\ l' - \rho' (\sin(\rho l) - \rho l) / \rho^2 \\ \cos(\varphi_j - \varphi_{j-1}) (\rho' l + l' \rho) \\ \sin(\varphi_j - \varphi_{j-1}) (\rho' l + l' \rho) \\ \varphi'_j - \varphi'_{j-1} \end{bmatrix} \\ \mathbf{V}_j = \begin{bmatrix} 0 \\ 0 \\ l' \\ 0 \\ 0 \\ \varphi'_j - \varphi'_{j-1} \end{bmatrix} \end{array} \right. \dot{\mathbf{q}} = \mathbf{J}_j \dot{\mathbf{q}} \quad \text{if } \rho \neq 0 \quad (3.31)$$

with: $\mathbf{q} = [\alpha_1 \dots \alpha_i l_1 \dots l_i]^T$ is the joints vector, $\rho' = \frac{\partial \rho}{\partial q}$, $l' = \frac{\partial l}{\partial q}$, and $\varphi' = \frac{\partial \varphi}{\partial q}$. (l' , ρ' , φ') are vectors of derivatives with respect to the joint variables q .

Once the velocity of each section is obtained, the general spacial velocity of the robot tip expressed in the base frame is given by:

$$\mathbf{V} = \mathbf{J} \dot{\mathbf{q}} \quad (3.32)$$

with

$$\mathbf{J} = \mathbf{J}_1 + \mathbf{Ad}({}^0\mathbf{H}_1) \mathbf{J}_2 + \dots + \mathbf{J}_j \mathbf{Ad}({}^0\mathbf{H}_j) \quad (3.33)$$

being the spacial Jacobian. $\mathbf{Ad}(\mathbf{H})$ is the adjoint transformation of the matrix \mathbf{H} [Murray et al., 1994].

- In the case of bending model, the vectors (ρ' , l' , φ') can be obtained by deriving the expressions of (l , ρ , φ).
- In the case of straight torsion model, the derivatives of (ρ , φ) can not be obtained by a straightforward derivation.

Consider β^* as the solution of the energy gradient set to zero (see (3.19)), it has:

$$\begin{cases} \frac{\partial \rho_j}{\partial q} = \frac{\partial \rho_j}{\partial \beta^*} \frac{\partial \beta^*}{\partial q} \\ \frac{\partial \varphi_j}{\partial q} = \frac{\partial \varphi_j}{\partial \beta^*} \frac{\partial \beta^*}{\partial q} \end{cases} \quad (3.34)$$

The derivatives $(\frac{\partial \rho_j}{\partial \beta^*}, \frac{\partial \varphi_j}{\partial \beta^*})$ can be obtained by a straightforward derivation of the expressions of (ρ, φ) given by (3.10).

At β^* , the gradient $\nabla Y = \Phi(q, \beta^*) = 0$ and $D_q \Phi = D_1 \Phi + (D_2 \Phi)(D_q \beta^*) = 0$, (D is the differential operator), which yields:

$$D_q \beta^* = -(D_2 \Phi)^{-1} (D_1 \Phi). \quad (3.35)$$

Substituting (3.35) into (3.34) gives:

$$\begin{cases} \frac{\partial \rho_j}{\partial q} = \frac{\partial \rho_j}{\partial \beta} \left(-\frac{\partial \Phi}{\partial \beta^*}\right)^{-1} \frac{\partial \Phi}{\partial q} \\ \frac{\partial \varphi_j}{\partial q} = \frac{\partial \varphi_j}{\partial \beta} \left(-\frac{\partial \Phi}{\partial \beta^*}\right)^{-1} \frac{\partial \Phi}{\partial q} \end{cases} \quad (3.36)$$

- The Jacobian matrix for the case of torsionally compliant model has no closed form. As introduced in [Rucker and Webster, 2011], a column J_i^s of the Jacobian corresponding to an element q_i of the joint vector and at a distance s from the robot shape can be approximated by the following relationship:

$$J_i^s \approx \left(\frac{H_i(s) - H(s)}{\Delta q_i} H(s)^{-1} \right)^\vee \quad (3.37)$$

with $H_i(s)$ being the pose of the end-effector at the joint position $(\mathbf{q}_i + \Delta \mathbf{q}_i)$ and the operator $^\vee$ allows the mapping from $se(3)$ to \mathbb{R}^6 (see [Antman, 1995]). This approximation is valid only under the conditions of small variations $\Delta \mathbf{q}_i$.

3.4 Inverse kinematic model

The inverse kinematic model is required in inverse kinematic control strategies which are widely used in CTR, especially in teleoperated architectures in which the master target

pose is interpreted to desired joints at the slave side (CTR) [Dupont et al., 2010b]. The inverse kinematic model is also used in design optimization in order to avoid obstacles [Bedell et al., 2011]. For the bending model [Sears and Dupont, 2006], the inverse kinematic model introduced in [Sears and Dupont, 2007] is split into two mappings: the first mapping calculates the section parameters represented by the bending components (χ_j, v_j) using the generalized inverse of the Jacobian matrix linking the tip velocity \mathbf{V} to the bending parameter velocities (χ_j, v_j) . The second mapping is a closed-form expression of the joints (α_i, t_i) in terms of the bending components (χ_j, v_j) .

For other models, the most oftenly used techniques for inverse kinematics calculation are not in a closed form. Root finding function has been used in [Su et al., 2012] which allows to solve the inverse kinematic problem after implementation of the forward kinematic model. In [Su et al., 2012], a lookup table of joint and position samples is used to initialize the root-finding algorithm. The Fourier series approximation function of the forward kinematic model mentioned in Section 2.5 is then inverted using a root-finding algorithm.

The pseudo-inverse of the Jacobian \mathbf{J}^+ in [Torres and Alterovitz, 2011] has been used to calculate the joint variations $\Delta \mathbf{q}$ approximatively corresponding to the tip position changes $\Delta \mathbf{X}$ in task space:

$$\Delta \mathbf{q} = \mathbf{J}^+ \Delta \mathbf{X} \quad (3.38)$$

where

$$\mathbf{J}^+ = \mathbf{J}^T (\mathbf{J}\mathbf{J}^T)^{-1}, \quad (3.39)$$

this pseudo inverse corresponds to the least square solution minimizing the joint velocities norm $\|\dot{\mathbf{q}}\|$ and the errors $\|\dot{\mathbf{X}} - \mathbf{J}\dot{\mathbf{q}}\|$.

The damped least square (see [Wampler, 1986]) of the Jacobian matrix \mathbf{J}^\dagger has been largely used [Hendrick et al., 2014] [Burgner et al., 2014] [Xu et al., 2013] [Burgner et al., 2011] as in the case of serial robots where the inverse kinematic model has no closed form and for the same objective as mentioned above:

$$\Delta \mathbf{q} = \mathbf{J}^\dagger \Delta \mathbf{X}, \quad (3.40)$$

where:

$$\mathbf{J}^\dagger = (\mathbf{J}^T \mathbf{J} + \lambda \mathbf{I})^{-1} \mathbf{J}^T, \quad (3.41)$$

where λ is the damping factor. This solution ensures a minimization of the errors $\|\dot{\mathbf{X}} - \mathbf{J}\dot{\mathbf{q}}\|^2 + \|\lambda\dot{\mathbf{q}}\|^2$. Inequality constraints can be added to this approximation problem in order to avoid the singularities and the joint limits.

3.5 Bifurcation phenomenon

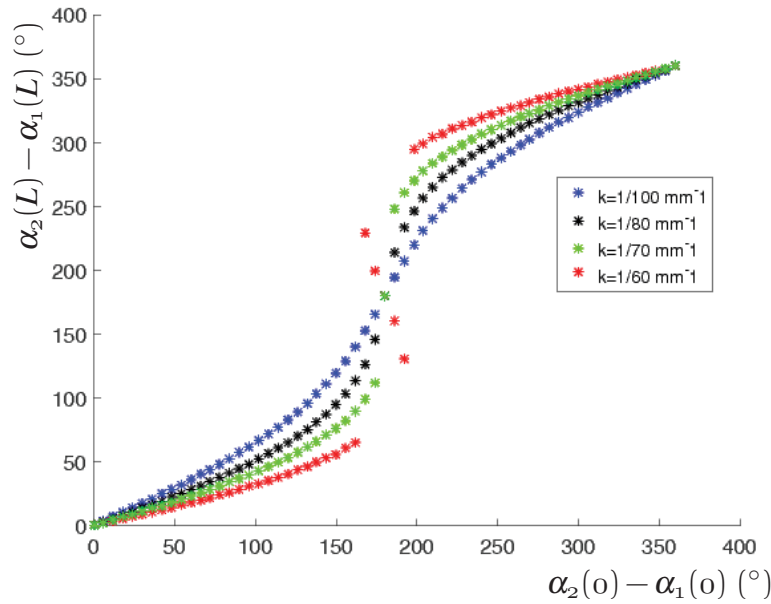


Figure 3.5 – Effect of tube curvatures on the elastic stability: from the blue (***) to the red (***) dot-curve, the curvatures of the two tubes are increased as $1/100, 1/80, 1/70, 1/60 \text{ mm}^{-1}$, and the lengths of both tubes are set to 100 mm .

When a CTR is in motion and maneuvering, the interactions between tubes develop elastic energy dues to bending and torsion. The resulting shape of a set of interacting tubes at the equilibrium is conformed such that the elastic energy is minimal. In some configurations, the elastic energy allows two minimum solutions, which causes an instable state of the robot in the form of ‘Jumps’ or also named ‘Bifurcations’ [Dupont et al., 2010a], [Webster III, 2007].

For the case of two tubes, these instable states appear once the relative tube rotations is close to π . The elastic stability can be evaluated by studying the evolution of the tubes angle difference at the distal extremity ($\alpha_2(L) - \alpha_1(L)$) according to the difference tube angles at the base ($\alpha_2(0) - \alpha_1(0)$). The elastic stability depends on the tube lengths and curvatures

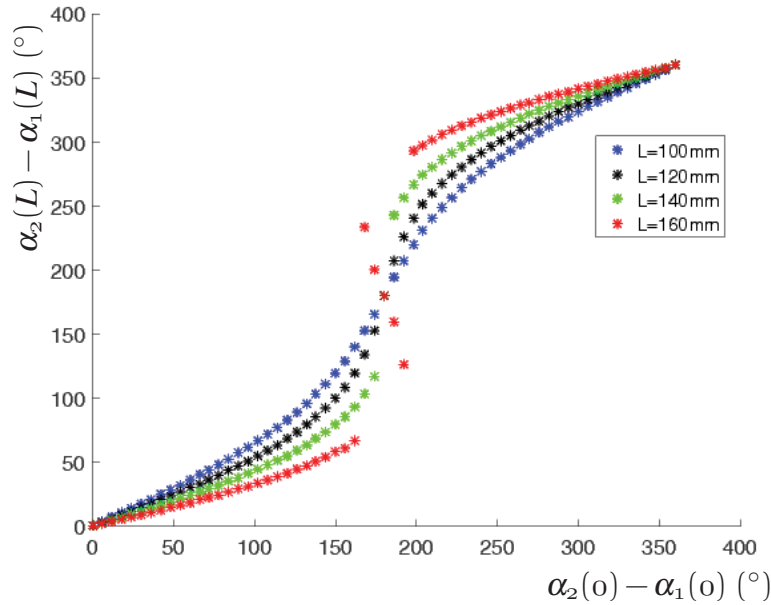


Figure 3.6 – Effect of tube lengths on the elastic stability: from the blue (***) to the red (***) dot-curve, the lengths of the two tubes are increased as (100, 120, 140, 160) mm, and the curvatures of both tubes are set to $1/100 \text{ mm}^{-1}$.

as well. A simulation study has been carried out in order to show the effect of the lengths and curvatures of the tubes on the elastic stability. In Figure 3.5, the pre-curvature for both two tubes forming the CTR has been increased. It can be seen from the figure that the green dot-curve is at the limit of stability and the distal angle difference admits two solutions, which creates the jumps at the tip position for the red dot-curve. The amplitude of jumps increase once the curvature increases. The length has the same impact on the elastic stability as it can be seen from Figure 3.6.

The characteristics of the two tubes used in this simulation case study are given in Table 3.1.

3.6 Conclusion

In this chapter, the forward, inverse and differential kinematic models for CTR have been introduced in detail. From this chapter, it can be concluded that the kinematic modelling of CTR represents a balance between complexity and accuracy which should be considered in the CTR motion control. The bifurcations presents a serious problem which should be

Table 3.1 – Tubes parameters used in simulation of length and curvature effects on the elastic stability.

	Outer tube	Inner tube
Outer diameter (<i>mm</i>)	1,63	1,05
Inner diameter (<i>mm</i>)	1,12	0.61
Young modulus (<i>GPa</i>)	50	50
Shear modulus (<i>GPa</i>)	19,23	19,23

considered at the level of tube design or at the level of path planing. The next two chapters of contributions are based on the kinematics introduced in this chapter and also take bifurcation into consideration for practical implementations.

Optimization of CTR Design for Deep Anterior Brain Tumor Surgery

Preamble

Most of existing works on the tubes design optimization of CTR do not consider the elastic stability in the objective function. The only work which formulates the elastic stability in the objective function is based on scalarization method which is the main tool used in existing multi-objective CTR design optimization works. The optimization objective in scalarization method is to maximize/minimize one single objective function composed of a set of weighted objective functions. In this method, the selection of function weights is crucial as the optimization results are greatly affected by them and could be misleading if these weights are improperly chosen. As an alternative optimization technique, Pareto grid-searching method can be used to avoid this problem and allow a straightforward interpretation of the optimization results. This chapter shows a three-tube CTR design based on Pareto grid-searching method in order to maximize the reachability and the elastic stability of the CTR within a specific curvature range dedicated to the deep anterior brain tumor removal surgery.

Contents

4.1	Introduction	56
4.2	Multi-objective optimization using Pareto methods	59

4.3	Techniques used to solve multi-objective optimization problem	59
4.4	Targeted surgical application	63
4.5	Workspace characterization and anatomical constraints	64
4.6	CTR configuration selection	66
4.7	Formulation of grid-searching optimization algorithm for CTR	69
4.8	Results and discussions	74
4.9	Conclusion	78

4.1 Introduction

In order to better benefit new less or non-invasive surgical procedures (Minimally Invasive Surgery, Single-Incision Laparoscopic Surgery, and Natural Orifice Transluminal Endoscopic Surgery), flexible medical devices are favorable [Jessica et al., 2015]. They are more convenient and safer in maneuver and navigation through body cavities than rigid devices. Moreover, flexible devices offer more accessibility to the surgical site in case of complex path from the insertion body point to the surgical site. CTR is flexible robot with the main concept of inserting pre-shaped flexible Nitinol tubes such that each of them can rotate and translate [Sears and Dupont, 2006].

CTR has been used in many medical applications, such as neurosurgery [Anor et al., 2011], intracardiac surgery [Bedell et al., 2011], endonasal skull base surgery [Burgner et al., 2011] and lung biopsy [Torres et al., 2012]. It is obvious that the required design of the robot tubes differs from one medical application to another. The tubes dimensions required for a given application depend mainly on the specific task and the involved anatomical structure. To achieve good operation performances, the robot tubes design should be optimized accordingly. The evolution of CTR design optimization presented previously in a general context can be traced from three aspects. Firstly, the design optimization follows the advances in kinematics modelling. In the early works on tubes design optimization, only basic kinematic model was used [Bedell et al., 2011] [Burgner et al., 2011]. Later on, more accurate kinematic model has been involved [Burgner et al., 2013a]. With more accurate kinematics, better robot design optimization could be obtained since the kinematic model is involved in the optimization calculation. Secondly, the design optimization evolution could also be analyzed from the view

of clinical applications addressed seeing that many specific design optimization algorithms have been proposed for different clinical procedures [Anor et al., 2011] [Bedell et al., 2011] [Burgner et al., 2011] [Torres et al., 2012]. Another axis of evolution is the transition from considering a discrete set of points in the cost function evaluating the coverage of the desired workspace to a volume-based cost function [Burgner et al., 2013a]. This evolution can be illustrated in Figure 4.1.

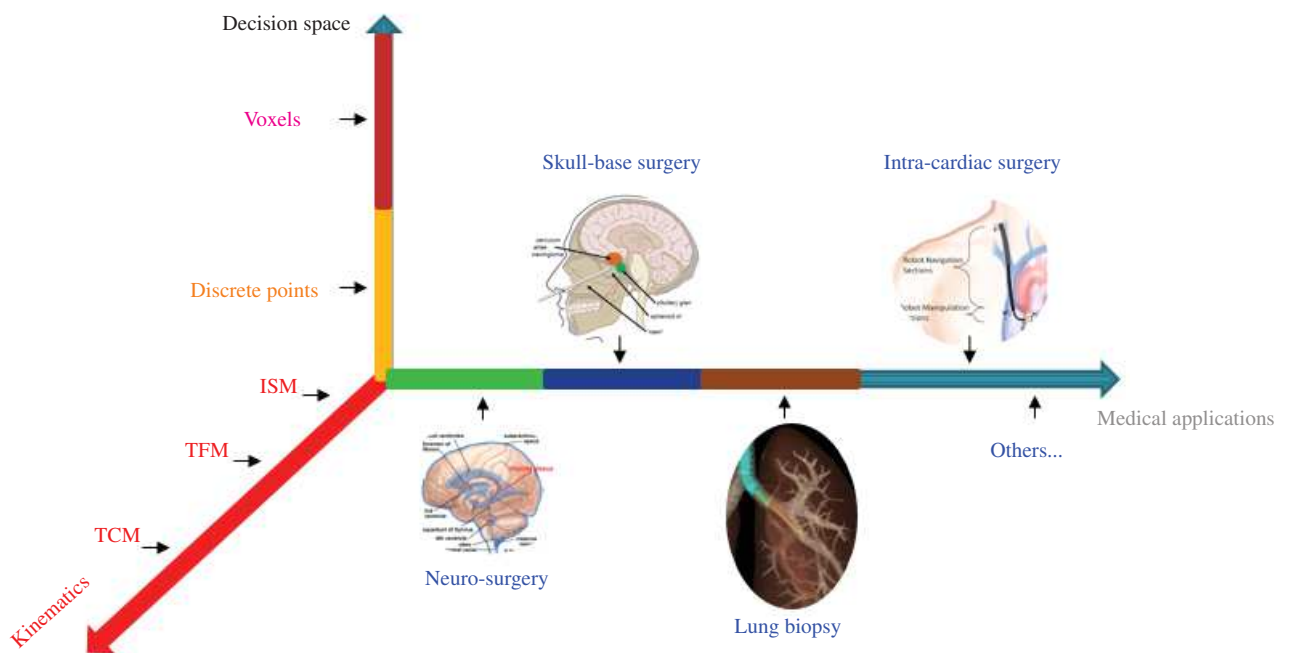


Figure 4.1 – Evolution of CTR tubes design. (ISM: Infinite Stiffness Model, TFM: Torsion Free Model, TCM: Transmissional Compliant Model)

The problem of elastic instability was not taken into account in CTR tube design optimization in literature until the work of [Ha et al., 2014], but it is limited to a particular case of two planar tubes with variable pre-curvature of the tubes. Bergeles et al. in [Bergeles et al., 2015] have shown a way to analyze the stability when the number of tubes exceeds two, but it is not applicable for arbitrary number of tubes. The elastic instability may occur when the difference of tube angles at the base of the robot is at the neighborhood of π . The rotation angle difference of the tubes at the distal part has no unique solution in the case of instability,

which generates a jump at this distal proximity [Dupont et al., 2010a]. As discussed in the previous chapter and shown in Figures 3.5 and 3.6, the elastic stability decreases once the curvatures and/or the lengths increase, and when it exceeds the stability limit the snapping phenomenon appears. This leads to a sudden variation of the robot end effector pose even if the rotation angle velocities of the tubes are low and smooth. This could lead to serious safety problem during the robotized intervention if it is not considered in the robot design or in the path planning.

The targeted surgical application considered in this work is deep frontal lobe brain tumors where elastic instability is of high risk to the operation safety. Therefore, in this work the elastic stability must be explicitly considered as an objective function in the optimization problem formulation. Instead of using scalarization methods in which the weights are pre-selected without any a priori informations, a Pareto grid-searching method has been used which incorporates all performance criteria within the optimization process and addresses them simultaneously to find a set of optimal designs in the objective space (the space constituted by the objective functions) [Unal et al., 2008], and therefore avoids the weight choice problem.

The objective of optimization in this work is to find the tube curvatures which suit best the specifications of the addressed surgical application. The robot structure and other parameters such as the lengths of the tubes and variation intervals of the curvatures to be optimized are pre-selected based on CT scan images in order to respect the anatomical constraints during the insertion and to be as close as possible to the optimal parameters with the help of surgeons.

Another contribution of this work is the use of forward kinematic model in the objective function instead of the inverse kinematics which has been used in [Bedell et al., 2011] and [Bergeles et al., 2015] to avoid the anatomical obstacles. The inverse kinematic model is complex and time consuming to calculate, and it requires a numerical optimization to be solved. The forward kinematic model used in this work is the torsionally compliant model developed in [Dupont et al., 2010a].

The optimal design presented in this chapter belongs to multi-objective (reachability and stability) optimization problem under constraint (anatomical constraints). The formulation of multi-objective optimization problem and the techniques used to solve it are briefly introduced in the next two sections.

4.2 Multi-objective optimization using Pareto methods

Multi-objective optimization considers a set of objective functions to be optimized simultaneously. These objective functions are usually in conflict with each other which causes a trade-off in selection of the optimal solution. A perfect solution that optimizes all the objective functions simultaneously is in general not available. The solution making a balance between all the objective functions is selected from a set of solutions in the objective space (formed by the set of objective functions) called Pareto front or Pareto curve.

Consider the following mathematical formulation of a multi-objective optimization problem:

$$\begin{aligned} \min_x \{ & \Phi_1(x), \Phi_2(x), \dots, \Phi_n(x) \} \\ \text{subject to } & x \in \varpi \end{aligned} \quad (4.1)$$

where $n > 1$ is the number of objective functions, $x \in \mathbb{R}^m$ is the decision variables vector of dimension m , $\Phi_{i=1, \dots, n}$ are the objective functions constituting the objective space, and ϖ is the set of constraints [Caramia and Dell'Olmo, 2008]. The constraints are expressed in terms of the decision variables and can have an equality $\varpi_{eq}(x)$ and/or an inequality $\varpi_{inq}(x)$ form:

$$\varpi = \{x \in \mathbb{R}^m : \varpi_{eq}(x) = 0, \varpi_{inq}(x) > 0\}. \quad (4.2)$$

A decision variable vector $x^* \in \varpi$ is the Pareto optimal vector for a multi-objective problem if all other vectors $x \in \varpi$ cause higher values for at least one objective function Φ_i or have the same values for all Φ_i . The Pareto front is formed by the collection of all efficient solutions (see the red curve in Figure 4.2). The trade-off between objective functions is concluded from this Pareto curve.

4.3 Techniques used to solve multi-objective optimization problem

In this section, two different techniques are presented for solving multi-objective optimization problem. The first one is the scalarization technique which transforms the multi-objective problem to a single-objective problem by weighting the objective functions without knowing the distribution of solutions in the objective space, and the second technique is grid-searching

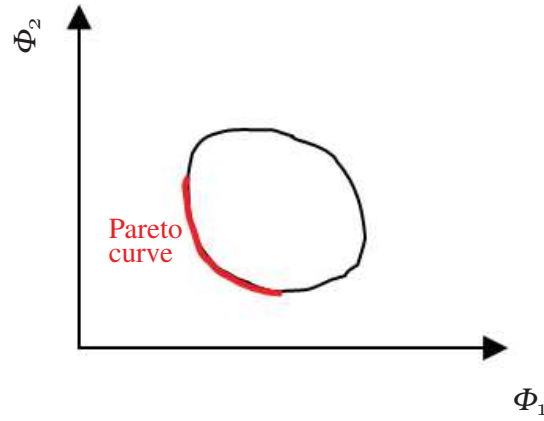


Figure 4.2 – Example of a Pareto front in case of two objective functions.

in which the solutions are analyzed in a direct way from graphics illustrations of the solutions distribution. The problem of pre-weighting the objective functions is then avoided.

4.3.1 Scalarization technique

Among all methods to solve Pareto optimal solutions for multi-criteria optimization, the scalarization method is the most commonly used one. In scalarisation method, the objective functions to be minimized are transformed to a single-objective scalar function by weighting and summing them [Kasprzak and Lewis, 2000]. The minimization of the new objective function is defined as:

$$\begin{aligned}
 \min_x \sum_{i=1}^n \omega_i \cdot \Phi_i(x), \\
 \sum_{i=1}^n \omega_i = 1, \quad (\omega_i > 0) \\
 \text{subject to } x \in \mathcal{W}
 \end{aligned} \tag{4.3}$$

The minimum of this new optimization objective belongs to the Pareto curve. This method is easy to understand and to implement. However, as the weights are pre-selected with no exact knowledge of the importance of each objective function, they may not correspond to the relative importance of the objective functions. It is also difficult for the decision maker

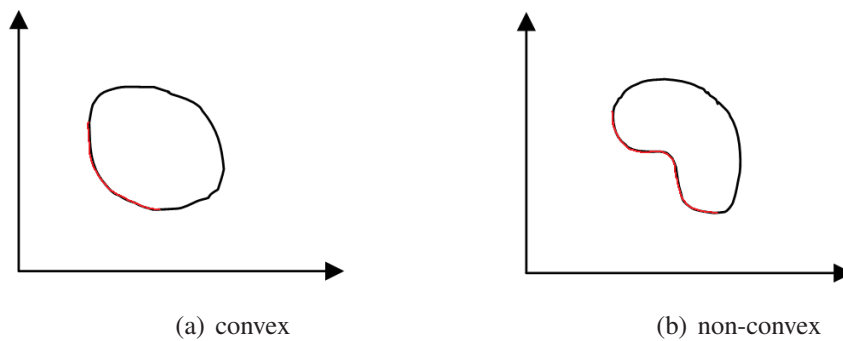


Figure 4.3 – Convex and non-convex Pareto curve.

to find an heuristic iterative variation law making them change in order to correctly change the solution and reach a part of the Pareto curve. Moreover, a vector of weights allows to find only one point from the Pareto front. To find more parts of the Pareto curve, selecting different weights vectors to perform more optimizations is required, which causes a large computational burden. Two other limitations of this scalarization technique can be observed as well: a uniform spread of the weights does not produce a uniform propagation of the Pareto curve points i.e. some points of the former have not been considered; non-convex Pareto set parts are not reachable with the minimization of convex combinations of the objective functions (see Figure 4.3) [Kasprzak and Lewis, 2000].

4.3.2 Grid-searching technique

As an alternative to the scalarization technique, grid-searching method generates a sampling of the Pareto curve and allows to avoid the drawbacks of scalarization previously introduced due to the pre-selection of the weights. Three steps are to be followed in order to define the best trade-off between different objective functions:

- First, the Pareto set is generated by taking a sampling grid of the decision space x and then to calculate their corresponding objective functions. The obtained points are plotted in the objective space as illustrated in Figure 4.4 for a two-function case, where the Pareto curve can be approximated by a polynomial. If the grid resolution is fine enough, this method guarantees to find both convex and non-convex portions of the Pareto curve.
- The next issue after tracing the Pareto set is to find the suitable solution on it. Many ap-

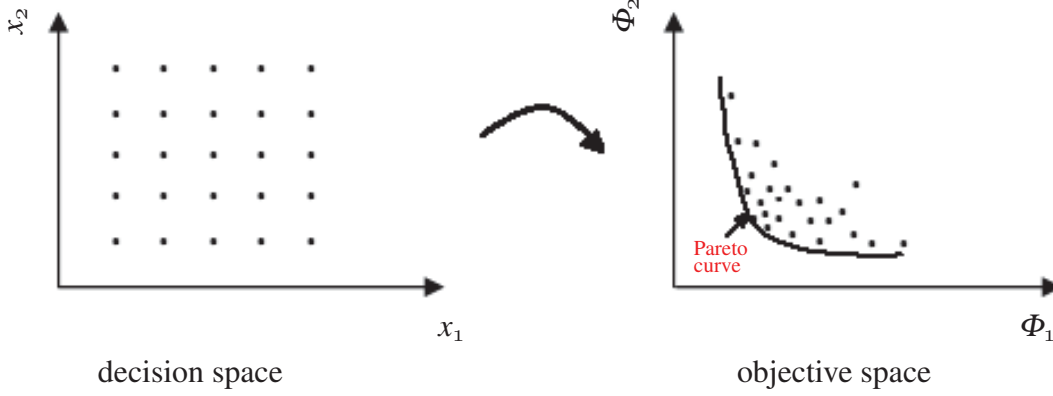


Figure 4.4 – Mapping from decision space to objective space.

proaches have been proposed in literature to solve this problem. The approach used in this work is the no-preference approach assuming “equal importance” of each objective function where the mostly used way to find the best solution is to calculate the L_2 norm for all the points as follows:

$$D_{L_2}(x) = \sqrt{\sum_{i=1}^n (\Phi_i(x) - \Phi_i^{min})^2}, \quad (4.4)$$

where Φ_i^{min} is the minimum of Φ_i , and then to select the point corresponding to the minimum of this distance [Kasprzak and Lewis, 2000]. In case of maximization of the objective functions, the maximum of the L_2 norm is used. Note that if the equal importance of the objective functions is not considered, then one of the plot axes should be scaled before calculating the L_2 norm, and this scale corresponds to the weight. This is different from scalarization methods where the weights are pre-selected without analysis of the solutions distribution in the objective space and this grid-searching technique where the scaling of the objective functions (weighting) is performed after analysis of the solutions distribution.

- The last step is to map from the Pareto set back to the decision space. There are many methods in literature which ensure this mapping such as intersection of constant objective contours, etc. In this work we select the decision variables that correspond to the optimal objective solution with highest L_2 norm obtained in the previous step. In the previously presented technique, the correspondence between the weights and the solutions is not known i.e. the weights se-

lected by the decision maker do not necessarily correspond to the relative importance of the objective functions. However, in this method the scaling in the objective space is done in a straightforward way with aid of graphics and corresponds to the relative importance of the objective functions. Moreover, in scalarization method, one weights vector corresponds to only one point of the Pareto curve which requires several optimization times to obtain a portion from the Pareto curve imposing computational burden, while in grid-searching method this problem is avoided and both convex and non-convex Pareto curve can be found (see [Caramia and Dell’Olmo, 2008] for more details).

4.4 Targeted surgical application

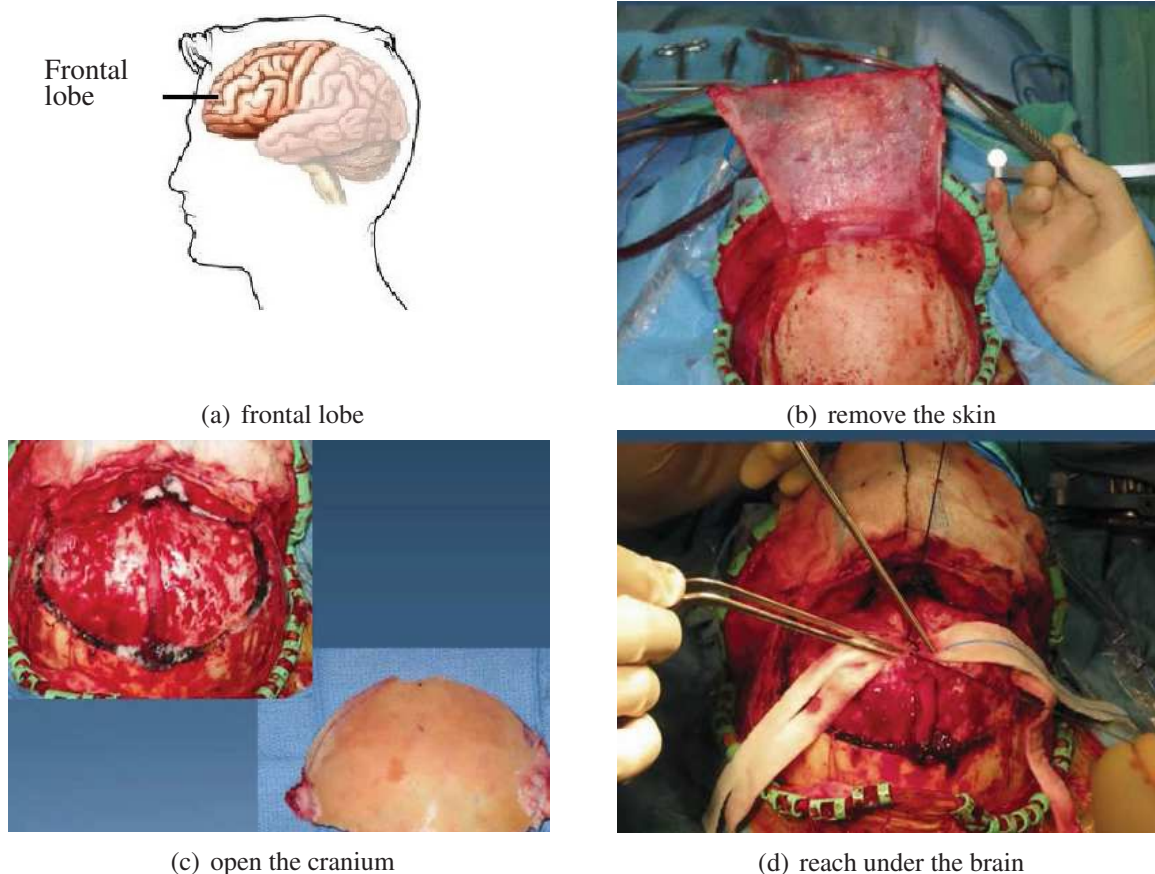


Figure 4.5 – Transcranial intervention for frontal lobe tumor resection [YOU]

In this work, the specific surgical application is considered; removal of deep frontal lobe brain tumors cf. Figure 4.5.a. It is noted that in year 2012, 70% of the over 250000 patients with brain tumor died in the world [IAR]. Usually for anterior skull base surgery, the procedure is transcranial, the access is created by severing a portion of the cranium. The surgeon needs to gently lift up the brain to access to the deep tumor located under the brain in order to accomplish the resection procedure cf. Figure 4.5.b-d. Following this procedure, the brain will swell up after the operation, which creates a brain pressure and causes a large trauma for the patient. To alleviate this problem, an endonasal approach is proposed by using CTR which is flexible and adaptable with the anatomical complexity. Note that, similar as the case in [Burgner et al., 2011] which addresses pituitary gland tumor removal, this operation requires bone drilling in order to access to the surgical site and reach the tumor. But the insertion path in our case from the nostril to the anterior wall of the frontal sinus (location of the drilling point) is surrounded with structures of high sensitivity cf. Figure 4.6.a-c. Another challenge of the targeted surgical application is the no-coaxiality of the insertion path with the tumor location increases the complexity of accessibility to the surgical site.

4.5 Workspace characterization and anatomical constraints

Given the three planes CT scan images (axial, coronal, and sagittal) of a real patient case study, a base frame F_b is attached to the patient head with its origin O close to the nose and centered at the median between the two nostrils as shown in Figure 4.6. The Z axis is oriented from the nose to the head back, the Y axis is oriented from the nose to the head top. The insertion point of the robot is at point P in Figure 4.6, with P defined as the origin of the robot frame F_r . The orientation of F_r is decided by two rotations: ϕ which orients the robot from the nostril to the frontal sinus in the Y - Z plan of the frame F_b and allows to avoid the nasal turbinates; and the ψ which orients the robot to the left or to the right of the cerebral falx depending on the tumor location.

Based on CT scan images and with more clarification and orientation of the surgeon, the space of the passage used to introduce the CTR from the nostril to the frontal sinus is identified roughly as a straight tunnel with variable diameter (from $\approx 10mm$ for smaller ellipse diameter

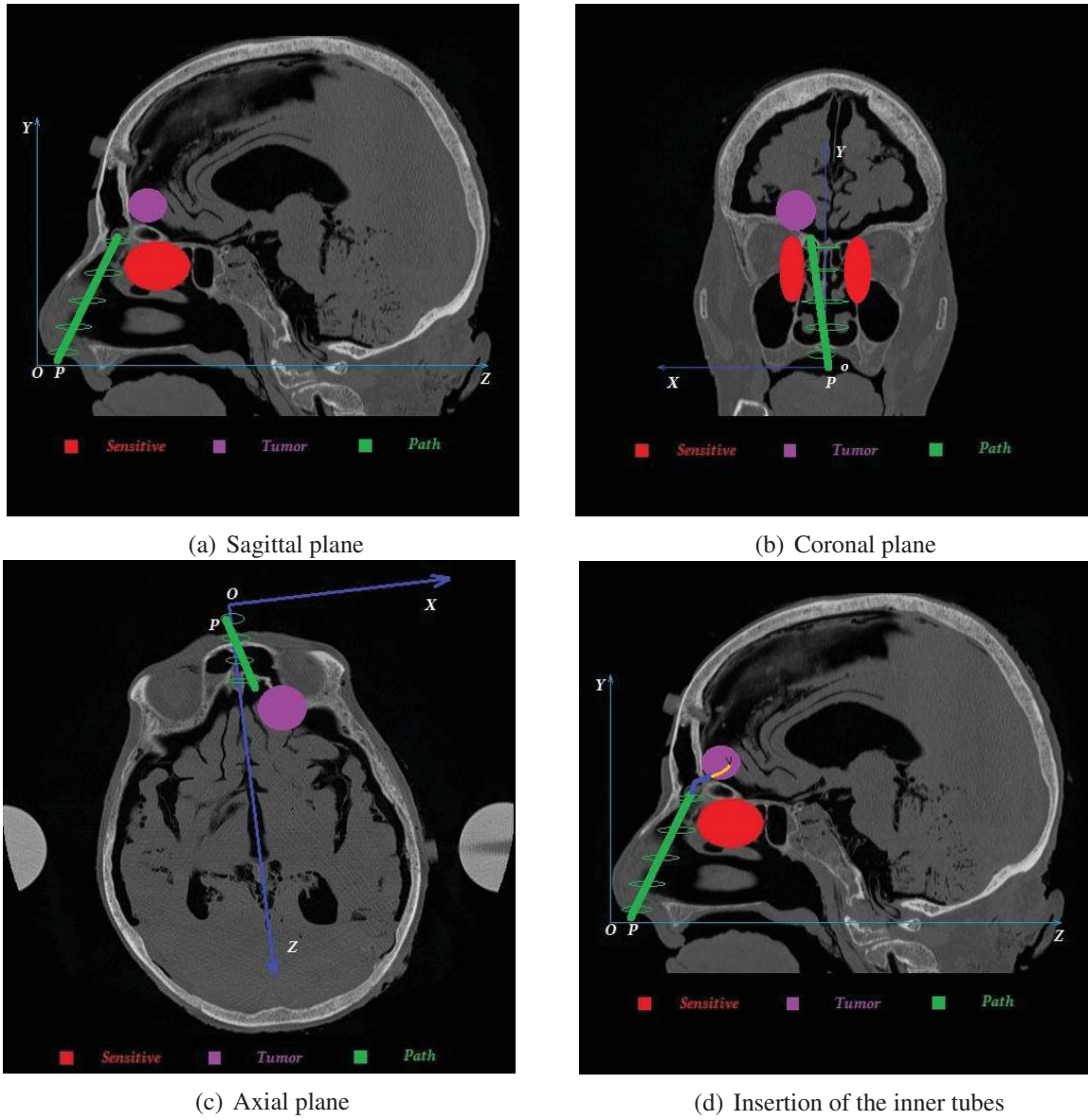


Figure 4.6 – Work-space characterization (a-c) and inner tubes insertion (d).

to $\approx 30mm$ for bigger ellipse diameter) and a length of $\approx 72mm$ for the patient sample studied. These allowed workspace borders are illustrated by six green ellipses in Figure 4.6. These anatomical constraints (orbits, optic canal, nerves etc) should be considered in an eligibility criterion. In order to reduce the friction during the robot insertion, a large passive tube is pre-inserted before introducing the robot. This facilitates the insertion of the robot in the first part of its path which is characterized by high friction according to the surgeons. Once the navigation path is traversed, the distal section of the robot accesses to the anterior skull base to manipulate at the tumor location.

A scenario of a sphere tumor defined by its center position coordinates c and its radius $a = 10\text{ mm}$ is shown by purple color in Figure 4.6. The frequent scenario in reality is that the tumor is located at the left of at the right of the frontal lobe. To perform the task of tumor removal, various tools can be attached to the distal extremity of the robot for purposes like ablation, retraction, blood stopping, etc.

4.6 CTR configuration selection

By considering the aforementioned anatomical description and operation requirements, a robot configuration is proposed in this section.

- Kinematics:

To fulfill accessibility and dexterity requirement, the candidate robot to be optimized is a three-tubes CTR. Only one outer tube can ensure the navigation from the nostril access to the entry of the desired surgical workspace because this path is almost a straight path after preparation from the surgeon; remove some nonsensitive structures (mycosis, etc) to facilitate the robot insertion. A variable curvature section is required to manipulate the robot tip as it offers more manipulability and coverage of the desired workspace. Two pre-curved inner tubes are required to form the variable curvature section. The outer-most tube T_1 is straight and the other two tubes T_2 and T_3 have two parts (straight and curved) as shown in Figure 4.7. The tubes deployment decides the number of tubes existing in a section, the number of sections, their order, lengths and curvatures (constant or variable curvature).

In terms of reachability, the proposed configuration allows to benefit from both advantages of constant curvature and variable curvature of the robot distal section. The distal section can

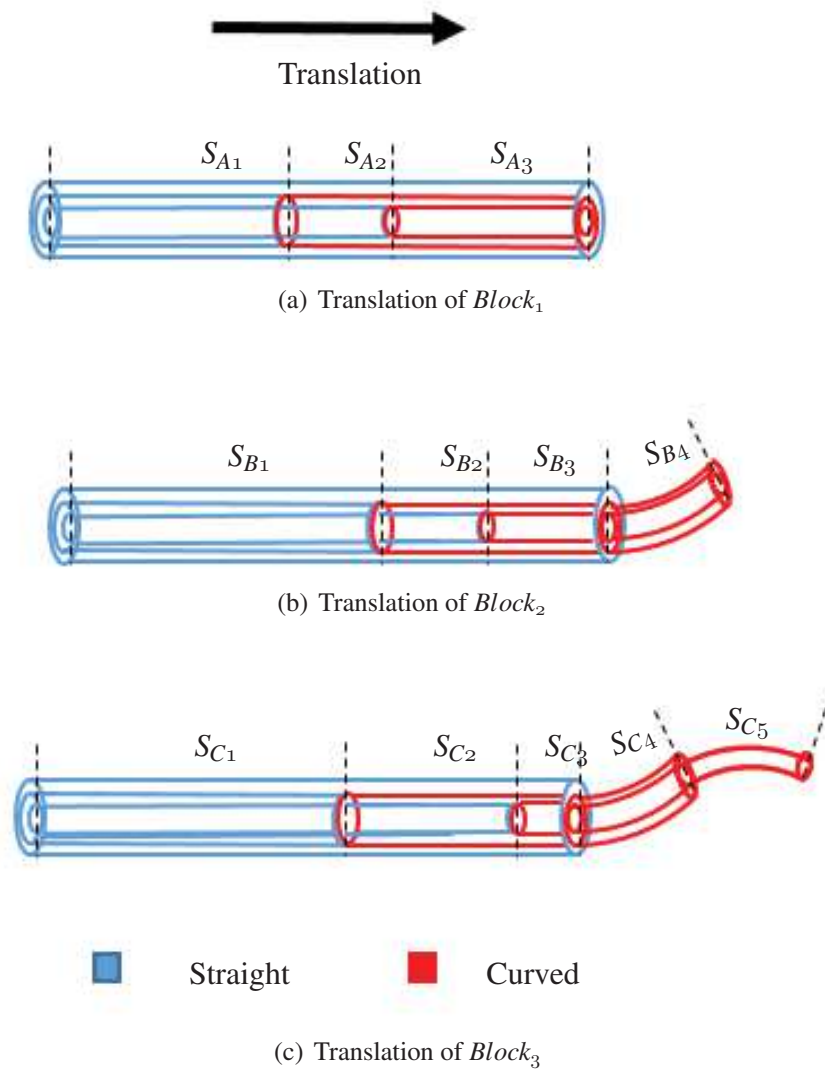


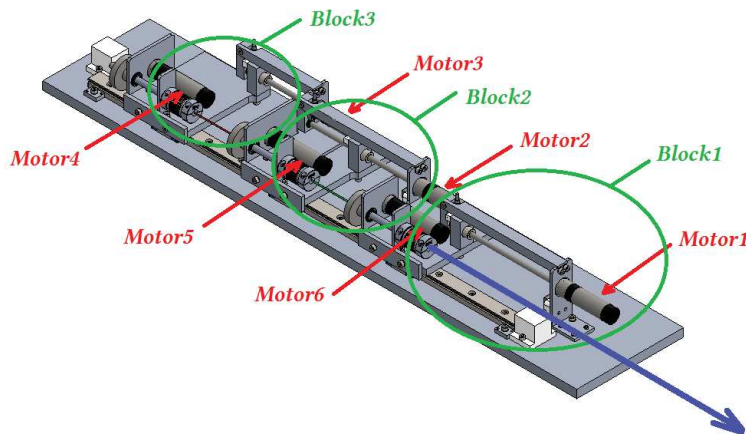
Figure 4.7 – Robot shaft sections

be composed by two pre-curved tubes which is a variable curvature section (S_{B4}) or by only one pre-curved tube which means a constant curvature section (S_{C5}) as seen in Figure 4.7. The translation limits, the curved and straight tube lengths define this transition constant/variable curvature of the distal section. The distal section manipulates the tool to accomplish the requested task (grasping, aspiration, electrocoagulation etc). For the proposed robot structure,

the constant curvature section allows to reach the regions far from the centerline of the robot shaft and the regions close to it could be reached by a variable curvature distal section as its curvature can decrease and then comes closer to the centerline.

- Actuation:

Concerning the actuation block it is composed of three blocks with one for each tube. Note that for the proposed actuation unit and for each tube, the rotation and translation are decoupled. Thanks to this decoupling, each rotation is controlled by one dedicated motor, which improves the control performance, facilitates the calibration procedure and reduces the modelling complexity.



(a) Robot Design



(b) CTR Platform

Figure 4.8 – CTR Robot: CAD and real platform.

The tubes translations are produced by the blocks translations, which are ensured by the rotations of nut-screw systems and guidance rails (see Figure 4.8.a). Once a block translates, it pulls the blocks behind it. This mechanism allows to reduce the tubes lengths and hence the tubes torsions. The *Block*₁ (front block) is dedicated to the outer-most tube T_1 , and the *Block*₃ (rear block) is dedicated to the inner-most one T_3 .

The insertion of the robot from the nostril till the frontal sinus is ensured by the translation of the *Block*₁ which pulls the two other blocks, producing a translation of the three tubes simultaneously. The distal proximities of the tubes are at the same limit. The shape of the robot shaft is held during this insertion. After this navigation insertion, the tube T_1 is held, then if only *Block*₂ is translated, the distal section of the robot is a variable curvature section (see Figure 4.7.b), otherwise a part of the inner-most tube T_3 extends out of tube T_2 and forms a distal constant curvature section (see Figure 4.7.c). Once the distal extremity of the robot accesses to the anterior cranial fossa through the posterior table of the frontal sinus, tube T_2 and/or T_3 are/is actuated in rotation and/or translation to accomplish the manipulation task.

The kinematic model used in this work for forward kinematics calculation is the torsionally compliant model [Dupont et al., 2009] presented previously. In this model, the pose of a point $\mathbf{G}(\mathbf{s})$ from the robot shaft and at a distance s from the robot base is obtained by two mappings h_1 and h_2 . The first mapping h_1 is to calculate the curvature $\mathbf{u}(\mathbf{s})$ in terms of the joint variables \mathbf{q} as noted by $\mathbf{u}(\mathbf{s}) = \mathbf{h}_1(\mathbf{q})$. The second mapping is to use the curvatures $\mathbf{u}(\mathbf{s})$ in order to define the pose $\mathbf{G}(\mathbf{s}) = \mathbf{h}_2(\mathbf{u}(\mathbf{s}))$.

The forward kinematic modelling is then split into two steps: the first one is to calculate the curvature $u(s)$ in term of the joint variables \mathbf{q} as noted by $\mathbf{u}(\mathbf{s}) = \mathbf{h}_1(\mathbf{q})$; the second one is to use the curvatures $\mathbf{u}(\mathbf{s})$ in order to define the robot shaft $\mathbf{G}(\mathbf{s}) = \mathbf{h}_2(\mathbf{u}(\mathbf{s}))$.

4.7 Formulation of grid-searching optimization algorithm for CTR

Recall that previous CTR design multi-criteria optimization algorithms use scalarization methods, which lumps the optimization objective functions in one single-objective function by assigning weights empirically to each objective function. The challenge of these methods is to properly choose the criteria weights which defines well their priorities and consequently

Table 4.1 – Notations and Dimensions

F_b : base frame with origin O , F_r : robot frame with origin P
ϕ : X -rotation angle of Rob , ψ : Y -rotation angle of Rob after its X -rotation
c : tumor center coordinates
h_1 : solves the nonlinear differential equation system of the forward kinematic model to obtain the curvatures $\mathbf{u}(s)$
h_2 : numerical integration of the curvatures $u(s)$ to define the robot shape
$\mathbf{G}(s)$: homogeneous matrix of the pose of a point s from the robot shaft
k_2, k_3 : curvatures of tubes T_2 and T_3 expressed in mm^{-1}
Δq : sampling step of the rotation joints, Δs : sampling length
χ : Cartesian tip position in F_b , $\chi = [\chi_1, \chi_2, \chi_3]$
a : radius of the sphere tumor = 10 mm
l_{s1} : length of the straight part of $T_1 = 70$ mm, l_{s2} : length of the straight part of $T_2 = 30$ mm
l_{c2} : length of the straight part of $T_3 = 31$ mm, l_{s1} : length of the curved part of $T_2 = 41$ mm
l_{s2} : length of the curved part of $T_3 = 43$ mm
Δk : curvature sampling step in the refining = $5mm^{-1}$
$k_2 = 55 : \Delta k : 70mm^{-1}, k_3 = 35 : \Delta k : 50mm^{-1}$

influences the optimization results [Unal et al., 2008]. However, there is no systematic and rigorous way reported to choose the weight values. Comparatively, the proposed grid-searching method [Caramia and Dell’Olmo, 2008] allows an interpretation of the optimization results in transparency, and the decision is taken by studying a set of possible solutions. The objective functions are evaluated along a large range of each optimization parameter.

4.7.1 Decision space of the CTR optimization problem

For our specific surgical application, the manipulation part of the robot extends from the drilling point to the posterior part of the tumor. For such a distance, the lengths of the curved parts of the two inner tubes do not have significant effect on the optimization results. Moreover, reducing the number of decision parameters allows to decrease the computation time significantly. Therefore the lengths of tubes are pre-selected suitable for the task respecting the workspace and anatomical constraints. The curvatures k_2 and k_3 of the tubes T_2 and T_3 respectively are considered as the decision variables. The localization of their ranges is firstly estimated from the geometry of the anatomical constraints, then obtained by executing the Algorithm.1 as introduce later.

4.7.2 Objective space of the CTR optimization problem

During the operation, the displacement of the robot tip inside the whole desired workspace is important. This displacement should be as long as possible and at the same time should be safe without sudden jumps. The objective space is then defined by two criteria (objective functions):

- **Reachability criterion:** In order to evaluate the reachability of the surgical workspace (tumor), this desired workspace is sampled homogeneously to a set of points $\mathbf{W}(\mathbf{i})$ ($i = 1, \dots, n$, where n is the total number of sample points). If the Euclidean distance between the workspace center and the tip position is less than or equal to the work-space radius a , we check which point from $\mathbf{W}(\mathbf{i})$ is closest to this tip position and then increase the score of reachability of this point $\mathbf{W}(\mathbf{i})$. For a given configuration (k_2, k_3) , a point from $\mathbf{W}(\mathbf{i})$, $i = 1, \dots, n$ can be reached more than once. Considering m is the number of the reached points from $\mathbf{W}(\mathbf{i})$, and recalling n is the number of the work-space sample points, the reachability is evaluated as:

$$C_{reach}(k_2, k_3) = \frac{m}{n} \times 100 \quad (4.5)$$

- **Stability criterion:** For the elastic stability analysis, previous works rely on the evolution of the difference of distal tubes angles in terms of the base difference tubes angles [Dupont et al., 2010a]. The case of three tubes was treated by Bergeles et al. in [Bergeles et al., 2015]. There is no systematic and general approach so far which allows to evaluate the elastic stability once the tube number exceed three.

In this work, a new way of stability evaluation is proposed. It relies on numerical evaluation of the tip trajectory smoothness. In case of elastic instability, jumps appear in the robot tip trajectory even if the tubes rotations variations are continuous and smooth. The elastic stability could be quantified by evaluating the Euclidean distance $\sqrt{\chi_1^2 + \chi_2^2}$ covered by the robot tip, since the robot shaft rotation is around the Z axis of the robot frame. In order to find out the jumps (case of elastic instability) on the distal angle difference in ascending and descending (see Figure 4.9), the *bvpinit* Matlab function is used to detect the symmetric solution (where the system admits two solutions) which shows a distal angle jump leading to a tip position jump (see blue and red arrows if Figure 4.9). The newly proposed approach is to quantify these jumps or discontinuities of the robot tip trajectory. Firstly, the numerical derivative of the Euclidean distance in term of the joint variation (rotation sampling step) is

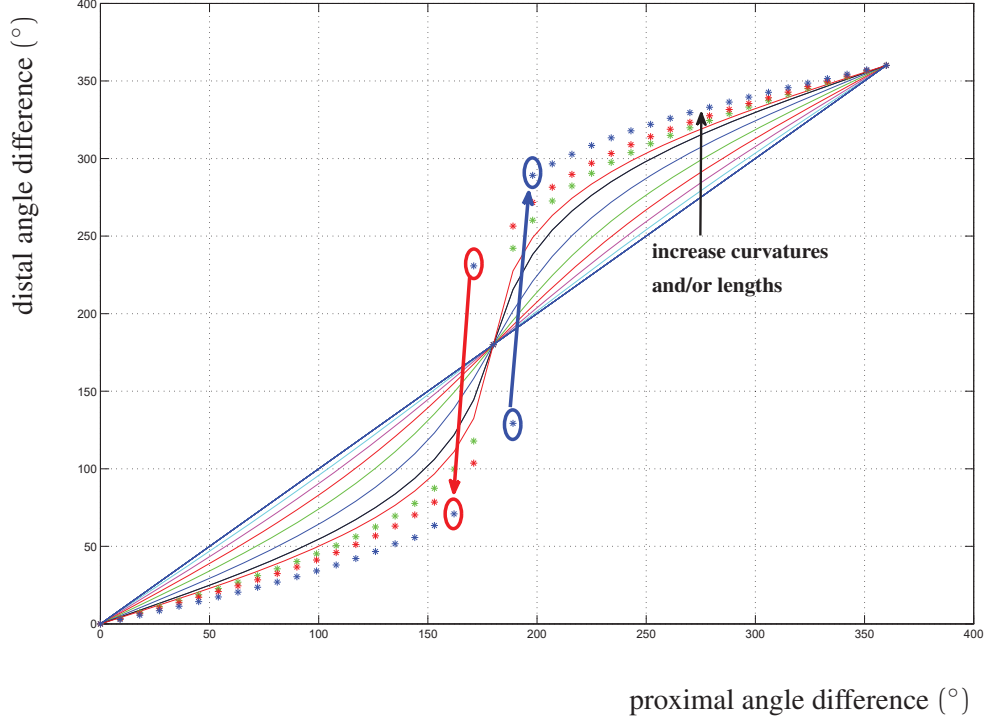


Figure 4.9 – Joint jumps

calculated for each configuration (k_2, k_3) as:

$$\frac{\Delta \sqrt{\chi_1^2 + \chi_2^2}}{\Delta q},$$

then the standard deviations of these derivatives are calculated. This mean allows to quantify the distance between two successive points of the trajectory along the whole set of points forming the trajectory and thus smoothness. The stability of a given configuration (k_2, k_3) is inversely proportional to the derivative standard deviation as the former increases with the occurrence of the jumps.

$$C_{stab}(k_2, k_3) = \text{normalization}\left(\frac{1}{std\left(\frac{\Delta \sqrt{\chi_1^2 + \chi_2^2}}{\Delta q}\right)}\right) \quad (4.6)$$

4.7.3 Constraints

The first constraint is to consider only the decision variables satisfying $(k_2 < k_3)$ during the grid sampling. This heuristic condition is recommended in [Dupont et al., 2010a] be-

cause the proximal sections are constrained by the navigation path and then should be of small curvature. Moreover, the distal sections which are composed of inner tubes dedicated to manipulating the tip should be of high curvatures. The second constraint is defined by an eligibility condition under the notation C_{eli} . The collision of the robot shaft with the anatomical structure is checked using the ellipses borders. Once the Y coordinate χ_2 of the robot is equal to the Y coordinate as an ellipse, this shaft robot point is checked to see if it is inside the ellipse or not by using the two radii of the ellipse to calculate the distance from the borders. The robot shaft is considered satisfying the eligibility condition if and only if each point of the robot which has the same Y coordinate of an ellipse is inside its corresponding ellipse. This condition is to be checked before evaluating the reachability and stability. The configurations outside of the borders are rejected and will not be evaluated in the reachability and stability criteria.

4.7.4 Grid-searching algorithm

Based on the selection criteria and the constraints aforementioned, a grid-searching algorithm can be developed for the CTR design optimization problem. The algorithm is explained as in following. As illustrated in Algorithm 1, for all the configurations of the grid (decision space), the forward kinematic model is calculated for all possible joint configurations (resolution sampling in rotation of $\pi/12 rad$, and in translation of $3mm$ is chosen to allow the coverage evaluation of the desired workspace regarding its dimension. The work of [Burgner et al., 2011] helps for this resolution selection). At each joint configuration, the limits defined by the ellipses are checked, then if the robot shaft satisfies these borders, the tip position is stored, else, this position is rejected. At the end of the algorithm, the stored positions of each configuration from the grid are evaluated in reachability and stability.

After the first execution of the Algorithm 1 with large sampling interval ($15mm^{-1}$) which allows to locate the variation ranges of the decision variables (k_2, k_3) ; where the optimal decision variables intervals corresponding to the highest reachability and stability may lie in. A second execution is conducted with smaller sampling interval ($5mm^{-1}$) to ensure a finer mapping from the decision variables (k_2, k_3) to the objective space (C_{stab}, C_{reach}) . The resolution of the grid in both large and small sampling intervals is estimated from this range of variation of the decision variables (k_2, k_3) as given in Table 4.1. For each configuration, (k_2, k_3)

of the grid satisfying $(k_2 < k_3)$, the eligibility condition C_{eli} is checked. If it is respected, then the two selection criteria are evaluated, i.e. the *stability criterion* C_{stab} and the *reachability criterion* C_{reach} as defined previously. The criteria C_{stab} and C_{reach} are evaluated along all the configurations satisfying the eligibility condition. The next step is to calculate the L_2 norm of all obtained solutions in the objective space. As the objective of this optimization problem is to maximize both objective functions, in the end the solution with highest L_2 norm is chosen and their corresponding (k_2, k_3) are defined as the optimal decision variables.

Initialization:

```

Reachable( $W(i)$ ) = 0 with  $i = 0 : n$ 
for  $k_2 = k_{2init} : k_{2fin}, k_3 = k_{3init} : k_{3fin}$  do
  config ++
  for  $d_2 = 0 : d_{2fin}, d_3 = 0 : d_{3fin}, \theta_2, \theta_3 = 0 : 2\pi$  do
     $u(s) = h_1(k_2, k_3, d_2, d_3, \theta_2, \theta_3)$ 
     $G(s) = h_2(u(s))$ 
    if  $\chi_2 = Y_{borders}$  then
      if the shaft is inside the ellipses borders then
        Test Reachability:
        if  $\chi - c \leq a$  then
           $ind = index(\min(\chi - W(i)))$ 
           $Reachable(config, ind) ++$ 
          save( $\chi$ ) to be used in  $C_{stab}$  evaluation
          save( $Reachable(config)$ ) to be used in  $C_{reach}$  evaluation
        end if
      end if
    end if
  end for
end for
end for
Calculate  $C_{stab}(config)$  for all configurations
Calculate  $C_{reach}(config)$  for all configurations

```

Algorithm 1: Grid-searching algorithm execution

4.8 Results and discussions

The tubes used in this study are made of Nitinol (55% Nickel-45% Titanium, see [EUR]) with the outer tube straight and the two inner tubes composed of two parts (a straight part followed by curved part). Their parameters are given in the Table.4.2.

Table 4.2 – Tubes parameters used in simulation of length and curvature effects on the elastic stability.

	T_1	T_2	T_3
Outer diameter (<i>mm</i>)	3,11	2,18	1,55
Inner diameter (<i>mm</i>)	2,66	1,76	1,15
Young modulus (<i>GPa</i>)	50	50	50
Shear modulus (<i>GPa</i>)	19,23	19,23	19,23

The grid-searching optimization method as explained in last section was executed twice: the first time with larger parameters interval (k_2, k_3) and curvatures sampling resolution; then the second time to refine the optimization procedure with smaller parameters interval and curvature sampling. In order to accelerate the computation, the algorithm has been run on a server with the characteristics: *Intel(R) Xeon(R), CPU E5-2695-v3 2.30GHz, (27 cores / 396 Go ram)*.

The results of the new stability evaluation approach obtained through the second execution are interpolated and shown in Figure 4.10. It can be seen from this illustration that the stability criterion index increases along both X and Y axis, i.e. when the curvatures (k_2, k_3) decrease (curvature radii increase) which is consistent with the evolution stability in terms of curvatures presented in [Dupont et al., 2010a]. The variation amplitude of the stability criterion is around 0.7.

Theoretically, the reachability can be improved by increasing the curvatures. However, in our study this rule is not well satisfied as the anatomical obstacles are considered along the whole robot shaft, i.e. many points from the workspace are eliminated by the eligibility condition. From Figure 4.11 it can be seen that simple linear relationship does not exist between reachability and curvature. In some cases the reachability increases by increasing the curvature and it decreases in other cases by increasing the curvature, which is explained by the anatomical constraints, i.e. the elimination of the tip positions which do not satisfy the eligibility condition and excluded from the reachable set of points. It can also be seen that the variation amplitude of the reachability is around 30% which justifies the importance of tubes design optimization.

From the mapping to the objective space shown in Figure 4.12, the solution with highest

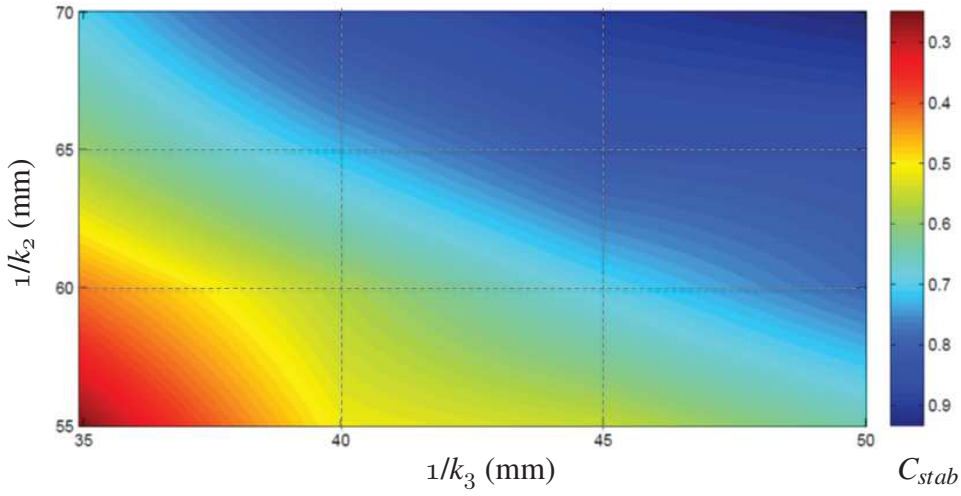


Figure 4.10 – Stability evaluation

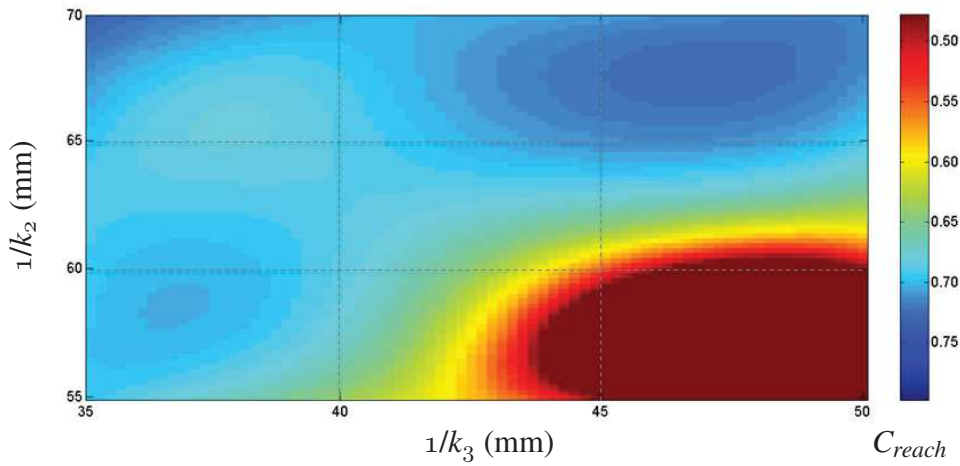


Figure 4.11 – Reachability evaluation

L_2 norm with respect to the P_{min} of coordinates $(\min(C_{reach}), \min(C_{stab})) = (0.46, 0.48)$ is selected ($D_{L_2} = 0.5631$). The point P_{opt} surrounded by a black circle is the one with highest L_2 norm, and all the other points corresponding to solutions with different decision variables (k_2, k_3) are included in the big blue circle with a radius equal to the D_{L_2} , i.e. with smaller L_2 values. This solution point corresponds to the reachability and stability value respectively at 0.72 and 0.99. The decision variables corresponding to this solution point P_{opt} are $k_2 = \frac{1}{70} mm^{-1}$, $k_3 = \frac{1}{50} mm^{-1}$. The reason why the number of points in Figure 4.12 is restricted (16

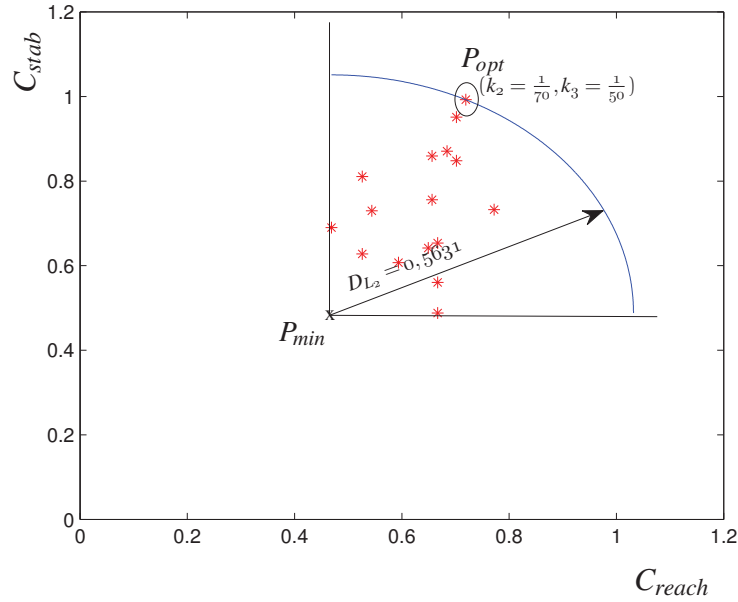


Figure 4.12 – Stability/Reachability selection

points) is because of the fact that non-suitable solutions have already been eliminated in the first execution of the algorithm.

Remark 3.1: The used optimization method addresses two-objective problem, however it can be extended to more than two objectives. If the number of objective functions exceeds three, the description of the Pareto set is hyperplane and more complicated compared to the case of two objectives.

Remark 3.2: Implementing of all optimization algorithms used for CTR existing in literature to carry out a comparison study is not a trivial work, especially for multi-objective scalarization methods in which one vector of weights provides only one point of the Pareto curve. This requires tremendous execution times for each algorithm with different combinations of the weights vector which is a huge task. The kinematics calculation is also time consuming, and to obtain the inverse kinematic model is an optimization problem itself and hence computationally heavy. For this reason, we focus on analyzing the advantages and the drawbacks of the technique used in literature and our proposed technique in this work from the working mechanism point of view and only numeric analyses of the latter are presented.

4.9 Conclusion

The main contribution of the work presented in this chapter is to provide an alternative method which avoids using scalarization techniques for multi-objective CTR tubes design optimization. These scalarization techniques as has been explained require weights pre-selection without any a priori information about the objective functions distribution. On contrary, grid-searching method has been used with a direct interpretation of the optimization results. Moreover, a new method of elastic stability evaluation has been used as an objective function. In this new approach, the stability is evaluated explicitly based on the smoothness of the robot tip trajectory instead of evaluating the tubes angles difference as in literature.

The obtained optimized tubes parameters will be used to curve the tubes to be integrated to our CTR platform, and the addressed deep tumor removal surgical procedure will be tested through *ex vivo* lab test and *in vivo* cadaver test.

Task-space Position Control of CTR Using Approximated Jacobian

Preamble

The kinematics modelling of CTR has been presented in Chapter 3. It should be noted that so far the developed kinematic models are either simplified and hence inaccurate, or complex and hence computationally heavy. Existing works in control of CTR are based on inverse kinematics calculation and thus the control performance largely relies on the accuracy of the kinematic model used. In this chapter, a new control method designed at the actuator level is proposed which shows that the control design of actuator input in task-space with approximate Jacobian matrix provides more flexibility and robustness in handling inaccuracy in kinematic model and maintains good control performance at the same time [Boushaki et al., 2014].

Contents

5.1	Introduction	80
5.2	Formulation of CTR position control task at actuator level	81
5.3	Task-space position control of CTR with inaccurate kinematics	82
5.4	Simulation studies	86
5.5	Conclusion	94

5.1 Introduction

Mechanics-based models with different assumptions have been developed to realize real time applications of CTR control. The first model proposed assumes that the outer most tube has infinity stiffness compared to inner tubes [Furusho et al., 2006]. Later on, more realistic physical phenomena previously neglected, such as bending and torsion, have been taken into consideration in order to improve the kinematics [D. Caleb and R. J, 2009b]. Based on the developed kinematic models, several motion planning algorithms have been developed [Lyons et al., 2009] [Lyons et al., 2010]. These motion planning algorithms resort to inverse kinematics calculation to obtain the actuator joint angles to achieve desired task space positions. However, the inverse kinematics calculation of CTR is not straightforward due to the nonlinear mapping between relative tube displacements and tip configuration as well as due to the multiplicity of solutions. A geometric approach is given for single and multiple sections in [Neppalli et al., 2009] by applying an analytical process to solve inverse kinematics based on modelling of each section with a spherical joint and a straight rigid link. Jacobian-based methods represent another approach to robot-independent inverse kinematics. In the Jacobian-based inverse kinematics strategy, it is possible to build actuator limits into the control law so that the robot trajectory is always physically realizable [R. J. Webster and Jones, 2010], e.g. [Sears and Dupont, 2007] for active cannula results. Root finding function are also used to solve the inverse kinematics calculation [Su et al., 2012].

It is noticed that existing works in literature on CTR position control are based on inverse kinematics calculation to get the necessary actuator joint angle first in order to achieve control tasks that are usually defined in operational space (image space, Cartesian space, etc). Consequently, the control performances are sensitive to the kinematic modelling inaccuracy. However, so far there exists no closed form inverse kinematic of CTR when the number of tubes exceeds two, and the modelling challenge lies in the physical phenomena due to elasticity interaction between tubes such as bending, friction and torsion. With the existence of kinematics modelling errors, the inverse kinematics based control methods may suffer position errors and lead to safety problems. Although in teleoperation scenario this kind of positioning deviation could be partially compensated by the surgeon, it is not always guaranteed to work as the surgeon intuitive manual correction command could be mis-interpreted by the inaccurate kinematics used in the inverse kinematics calculation.

To alleviate this problem, the CTR position control from the actuator input level is investigated in this work. It is shown that even if only approximate Jacobian matrix is available, the position control task can still be accomplished with a simple PID form control torque input based on task space feedback position errors. The proposed control design is rigorously analysed through theoretical proof. Simulation studies based on a realistic experimental platform (see Figure 5.2) are shown to justify the advantage of proposed task-space control method over inverse kinematics based design method in handling kinematics modelling inaccuracy.

5.2 Formulation of CTR position control task at actuator level

In literature, the position control of concentric tube robot is mostly formulated as a motion planning problem based on inverse kinematics calculation. Given the desired position or trajectory \mathbf{x}_d in operational space, which can be obtained by interpreting the tele-operator hands motions in case of tele-operation scenario (refer to Figure 5.1), the corresponding desired joint positions or trajectories \mathbf{q}_d are calculated by solving the inverse kinematics:

$$\mathbf{q}_d = f_{InvKin}(\mathbf{x}_d), \quad (5.1)$$

and it is assumed that the actuator for each joint will faithfully generate the desired joint motion \mathbf{q}_d . However, if the robot kinematics is not accurately modeled, the joint position obtained through calculation (5.1) may not guarantee the desired operational space position.

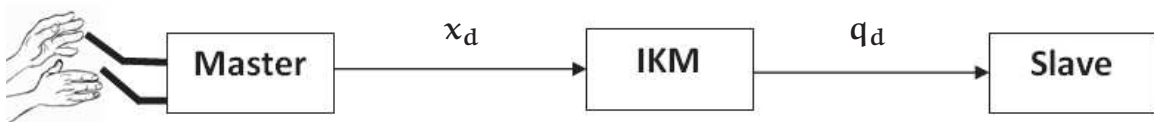


Figure 5.1 – The task-space desired trajectory at the master side is converted through the inverse kinematic model f_{InvKin} to a desired joint trajectory at the slave side.

In this work, the kinematics modelling error from the actuator control input level are compensated and the inverse kinematics calculation is bypassed, inspired by the works on uncertain kinematics task-space control for serial robot in literature [Liu and Cheah, 2006] [Liu et al., 2006].

For existing CTR design, the joints are normally actuated by current driven motors which possess the following dynamics:

$$M_i \ddot{\theta} + C_i \dot{\theta} = K_i u_i - \frac{\tau_{ei}}{r_i} \quad (5.2)$$

where θ denotes the motor rotor shaft angle, M_i denotes the rotor inertia moment, C_i denotes the friction coefficient and K_i the torque constant. u_i is the control current input, τ_{ei} is the external load torque. $r_i = \theta_i/q_i$ is the transmission gear ratio from the motor angle θ to the CTR joint variables \mathbf{q} , which is usually quite big and thus the effect of external load τ_{ei} could be neglected. Considering the linear relationship between actuator and joint variables $\theta_i = r_i q_i$ and, for simplicity of expression and without loss of generality, setting $\frac{K_i}{r_i} = 1$, the dynamic relationship between CTR joint variables and actuator input can be written from (5.2) as:

$$\mathbf{M} \ddot{\mathbf{q}} + \mathbf{C} \dot{\mathbf{q}} = \mathbf{u} \quad (5.3)$$

where $\mathbf{M} = \text{diag}([M_1, \dots, M_n])$, $\mathbf{C} = \text{diag}([C_1, \dots, C_n])$ and $\mathbf{u} = \text{diag}([u_1, \dots, u_n])$.

Now the position control task could be specified at the actuator level: design the actuator current input \mathbf{u} such that the tip position \mathbf{x} of CTR can reach the desired operational space position ($\Delta \mathbf{x} = \mathbf{x} - \mathbf{x}_d = \mathbf{0}$) even with inaccurate kinematics model. Compared to joint level control which is directly influenced by the kinematics errors, the lower level control design provides another solution which possesses more flexibility to handle such kind of problem.

5.3 Task-space position control of CTR with inaccurate kinematics

The operational space velocity $\dot{\mathbf{x}}$ and the CTR joint velocity $\dot{\mathbf{q}}$ could be determined by Jacobian matrix $\mathbf{J}(\mathbf{q})$ as [R. J. Webster and Jones, 2010]

$$\dot{\mathbf{x}} = \mathbf{J}(\mathbf{q}) \dot{\mathbf{q}}. \quad (5.4)$$

5.3. TASK-SPACE POSITION CONTROL OF CTR WITH INACCURATE KINEMATICS

With the presence of kinematics errors, accurate Jacobian matrix is unknown and only estimated (best-guess) Jacobian $\hat{\mathbf{J}}(\mathbf{q})$ is available.

In this study, it is assumed that the Jacobian estimation error $\|\hat{\mathbf{J}}(\mathbf{q}) - \mathbf{J}(\mathbf{q})\|$ is bounded with an upper limit β as

$$\|\hat{\mathbf{J}}(\mathbf{q}) - \mathbf{J}(\mathbf{q})\| \leq \beta. \quad (5.5)$$

Based on the approximate Jacobian matrix $\hat{\mathbf{J}}(\mathbf{q})$, the control current input can be designed with the use of task-space position error as in the following form:

$$\mathbf{u} = -\hat{\mathbf{J}}^T(\mathbf{q})\mathbf{K}_p\Delta\mathbf{x} - \mathbf{K}_d\dot{\mathbf{q}} - k_i \int_0^t (\dot{\mathbf{q}} + \alpha\hat{\mathbf{J}}^T(\mathbf{q})\Delta\mathbf{x})d_t \quad (5.6)$$

where $\mathbf{K}_p = k_p\mathbf{I}$, $\mathbf{K}_d = k_d\mathbf{I}$ and k_i are positive definite control gains, α is a positive scalar.

Since the CTR joint velocities are not directly measurable and noting the fact that $\dot{\mathbf{q}} = \mathbf{r}^{-1}\dot{\boldsymbol{\theta}}$, the control input is actually implemented using easily available and more accurate actuator joint velocity $\dot{\boldsymbol{\theta}}$ as

$$\mathbf{u} = -\hat{\mathbf{J}}^T(\mathbf{q})\mathbf{K}_p\Delta\mathbf{x} - \mathbf{K}'_d\dot{\boldsymbol{\theta}} - K'_i \int_0^t (\dot{\boldsymbol{\theta}} + \alpha'\hat{\mathbf{J}}^T(\mathbf{q})\Delta\mathbf{x})d_t \quad (5.7)$$

which is equivalent to the control design in (5.6) with $\mathbf{K}'_d = \mathbf{K}_d\mathbf{r}^{-1}$, $K'_i = k_i\mathbf{r}^{-1}$, $\alpha' = \mathbf{r}\alpha$.

It is seen from the proposed control input (5.6) or (5.7) that no inverse Jacobian calculation is required in this control method which is in general much more complicated than transpose Jacobian calculation. The task-space position error can be obtained online through different imaging modalities (camera, ultrasound, MRI, magnetic tracker, etc) according to different clinical applications.

Next, the system positioning performance through Lyapunov analysis are investigated. Substituting control input (5.6) into the dynamics equation (5.3), the closed-loop system dynamics has

$$\mathbf{M}\ddot{\mathbf{q}} = -\hat{\mathbf{J}}^T(\mathbf{q})\mathbf{K}_p\Delta\mathbf{x} - (\mathbf{C} + \mathbf{K}_d)\dot{\mathbf{q}} - k_i \int_0^t (\dot{\mathbf{q}} + \alpha\hat{\mathbf{J}}^T(\mathbf{q})\Delta\mathbf{x})d_t. \quad (5.8)$$

Propose a Lyapunov function candidate as

$$V = \frac{1}{2}\dot{\mathbf{q}}^T\mathbf{M}\dot{\mathbf{q}} + \alpha\dot{\mathbf{q}}^T\mathbf{M}\hat{\mathbf{J}}^T(\mathbf{q})\Delta\mathbf{x} + \frac{1}{2}\Delta\mathbf{x}^T\mathbf{K}_p\Delta\mathbf{x} + \frac{1}{2}\mathbf{z}^T k_i \mathbf{z} \quad (5.9)$$

where $\mathbf{z} = \int_0^t (\dot{\mathbf{q}} + \alpha\hat{\mathbf{J}}^T(\mathbf{q})\Delta\mathbf{x})d_t$.

Rewrite V into the form

$$\begin{aligned}
 V &= \frac{1}{2}(\dot{\mathbf{q}} + \alpha \hat{\mathbf{J}}^T(\mathbf{q})\Delta\mathbf{x})^T \mathbf{M}(\dot{\mathbf{q}} + \alpha \hat{\mathbf{J}}^T(\mathbf{q})\Delta\mathbf{x}) \\
 &\quad - \frac{\alpha^2}{2}\Delta\mathbf{x}^T \hat{\mathbf{J}}(\mathbf{q})\mathbf{M}\hat{\mathbf{J}}^T(\mathbf{q})\Delta\mathbf{x} + \frac{1}{2}\Delta\mathbf{x}^T \mathbf{K}_p\Delta\mathbf{x} + \frac{1}{2}\mathbf{z}^T k_i \mathbf{z} \\
 &= \frac{1}{2}(\dot{\mathbf{q}} + \alpha \hat{\mathbf{J}}^T(\mathbf{q})\Delta\mathbf{x})^T \mathbf{M}(\dot{\mathbf{q}} + \alpha \hat{\mathbf{J}}^T(\mathbf{q})\Delta\mathbf{x}) \\
 &\quad + \frac{1}{2}\Delta\mathbf{x}^T (\mathbf{K}_p - \alpha^2 \hat{\mathbf{J}}(\mathbf{q})\mathbf{M}\hat{\mathbf{J}}^T(\mathbf{q}))\Delta\mathbf{x} + \frac{1}{2}\mathbf{z}^T k_i \mathbf{z}
 \end{aligned} \tag{5.10}$$

Since matrix $\hat{\mathbf{J}}(\mathbf{q})\mathbf{M}\hat{\mathbf{J}}^T(\mathbf{q})$ is positive semi-definite, if α is chosen small such that the following matrix is positive definite

$$\mathbf{K}_p - \alpha^2 \hat{\mathbf{J}}(\mathbf{q})\mathbf{M}\hat{\mathbf{J}}^T(\mathbf{q}) > 0, \tag{5.11}$$

then

$$V > \frac{1}{2}(\dot{\mathbf{q}} + \alpha \hat{\mathbf{J}}^T(\mathbf{q})\Delta\mathbf{x})^T \mathbf{M}(\dot{\mathbf{q}} + \alpha \hat{\mathbf{J}}^T(\mathbf{q})\Delta\mathbf{x}) + \frac{1}{2}\mathbf{z}^T k_i \mathbf{z} > 0 \tag{5.12}$$

which is positive definite in $\dot{\mathbf{q}} + \alpha \hat{\mathbf{J}}^T(\mathbf{q})\Delta\mathbf{x}$ and \mathbf{z} .

Differentiate V with respect to time, it has

$$\begin{aligned}
 \dot{V} &= (\dot{\mathbf{q}} + \alpha \hat{\mathbf{J}}^T(\mathbf{q})\Delta\mathbf{x})^T \mathbf{M}\ddot{\mathbf{q}} + \alpha \dot{\mathbf{q}}^T \mathbf{M}\dot{\hat{\mathbf{J}}^T}(\mathbf{q})\Delta\mathbf{x} + \Delta\mathbf{x}^T \mathbf{K}_p \mathbf{J}(\mathbf{q})\dot{\mathbf{q}} \\
 &\quad + \alpha \dot{\mathbf{q}}^T \mathbf{M}\dot{\hat{\mathbf{J}}^T}(\mathbf{q})\mathbf{J}(\mathbf{q})\dot{\mathbf{q}} + (\dot{\mathbf{q}} + \alpha \hat{\mathbf{J}}^T(\mathbf{q})\Delta\mathbf{x})^T k_i \dot{\mathbf{z}}
 \end{aligned} \tag{5.13}$$

Substituting the closed-loop system dynamics (5.8) into (5.13), it has

$$\begin{aligned}
 \dot{V} &= (\dot{\mathbf{q}} + \alpha \hat{\mathbf{J}}^T(\mathbf{q})\Delta\mathbf{x})^T [-\hat{\mathbf{J}}^T(\mathbf{q})\mathbf{K}_p\Delta\mathbf{x} - (\mathbf{C} + \mathbf{K}_d)\dot{\mathbf{q}} - k_i \mathbf{z}] \\
 &\quad + \alpha \dot{\mathbf{q}}^T \mathbf{M}\dot{\hat{\mathbf{J}}^T}(\mathbf{q})\Delta\mathbf{x} + \alpha \dot{\mathbf{q}}^T \mathbf{M}\dot{\hat{\mathbf{J}}^T}(\mathbf{q})\mathbf{J}(\mathbf{q})\dot{\mathbf{q}} + \Delta\mathbf{x}^T \mathbf{K}_p \mathbf{J}(\mathbf{q})\dot{\mathbf{q}} \\
 &\quad + (\dot{\mathbf{q}} + \alpha \hat{\mathbf{J}}^T(\mathbf{q})\Delta\mathbf{x})^T k_i \dot{\mathbf{z}} \\
 &= -\dot{\mathbf{q}}^T \hat{\mathbf{J}}^T(\mathbf{q})\mathbf{K}_p\Delta\mathbf{x} - \dot{\mathbf{q}}^T (\mathbf{C} + \mathbf{K}_d)\dot{\mathbf{q}} - \alpha \mathbf{K}_p\Delta\mathbf{x}^T \hat{\mathbf{J}}(\mathbf{q})\hat{\mathbf{J}}^T(\mathbf{q})\Delta\mathbf{x} \\
 &\quad - \alpha \Delta\mathbf{x}^T \hat{\mathbf{J}}(\mathbf{q})(\mathbf{C} + \mathbf{K}_d)\dot{\mathbf{q}} + \alpha \dot{\mathbf{q}}^T \mathbf{M}\dot{\hat{\mathbf{J}}^T}(\mathbf{q})\Delta\mathbf{x} \\
 &\quad + \alpha \dot{\mathbf{q}}^T \mathbf{M}\dot{\hat{\mathbf{J}}^T}(\mathbf{q})\mathbf{J}(\mathbf{q})\dot{\mathbf{q}} + \Delta\mathbf{x}^T \mathbf{K}_p \mathbf{J}(\mathbf{q})\dot{\mathbf{q}} \\
 &= -\mathbf{K}_p\dot{\mathbf{q}}^T (\hat{\mathbf{J}}(\mathbf{q}) - \mathbf{J}(\mathbf{q}))^T \Delta\mathbf{x} - \alpha \Delta\mathbf{x}^T \hat{\mathbf{J}}(\mathbf{q})(\mathbf{C} + \mathbf{K}_d)\dot{\mathbf{q}} \\
 &\quad + \alpha \dot{\mathbf{q}}^T \mathbf{M}\dot{\hat{\mathbf{J}}^T}(\mathbf{q})\Delta\mathbf{x} - \dot{\mathbf{q}}^T (\mathbf{C} + \mathbf{K}_d)\dot{\mathbf{q}} + \alpha \dot{\mathbf{q}}^T \mathbf{M}\dot{\hat{\mathbf{J}}^T}(\mathbf{q})\mathbf{J}(\mathbf{q})\dot{\mathbf{q}} \\
 &\quad - \alpha \mathbf{K}_p\Delta\mathbf{x}^T \hat{\mathbf{J}}(\mathbf{q})\hat{\mathbf{J}}^T(\mathbf{q})\Delta\mathbf{x}
 \end{aligned} \tag{5.14}$$

5.3. TASK-SPACE POSITION CONTROL OF CTR WITH INACCURATE KINEMATICS

By using the Jacobian estimation bound (5.5), it has

$$\begin{aligned} \dot{V} \leq & -\{\lambda_{\min}[\mathbf{C} + \mathbf{K}_d] - \alpha\|\mathbf{M}\hat{\mathbf{J}}^T(\mathbf{q})\mathbf{J}(\mathbf{q})\|\}\|\dot{\mathbf{q}}\|^2 \\ & -\alpha\mathbf{K}_p\lambda_{\min}[\hat{\mathbf{J}}(\mathbf{q})\hat{\mathbf{J}}^T(\mathbf{q})]\|\Delta\mathbf{x}\|^2 + \{\mathbf{K}_p\beta \\ & + \alpha[\|\hat{\mathbf{J}}(\mathbf{q})(\mathbf{C} + \mathbf{K}_d)\| + \|\mathbf{M}\hat{\mathbf{J}}^T(\mathbf{q})\|\]}\|\dot{\mathbf{q}}\|\|\Delta\mathbf{x}\| \end{aligned} \quad (5.15)$$

where $\lambda_{\min}[\cdot]$ denotes the minimum eigenvalue of a matrix.

Since

$$\|\dot{\mathbf{q}}\|\|\Delta\mathbf{x}\| \leq \frac{1}{2}(\|\dot{\mathbf{q}}\|^2 + \|\Delta\mathbf{x}\|^2) \quad (5.16)$$

Inequality (5.15) can be further written as

$$\begin{aligned} \dot{V} \leq & -\frac{1}{2}\{2\lambda_{\min}[\mathbf{C} + \mathbf{K}_d] - \mathbf{K}_p\beta - \alpha[2\|\mathbf{M}\hat{\mathbf{J}}^T(\mathbf{q})\mathbf{J}(\mathbf{q})\| \\ & + \|\hat{\mathbf{J}}(\mathbf{q})(\mathbf{C} + \mathbf{K}_d)\| + \|\mathbf{M}\hat{\mathbf{J}}^T(\mathbf{q})\|]\}\|\dot{\mathbf{q}}\|^2 \\ & -\frac{1}{2}\{\mathbf{K}_p[2\alpha\lambda_{\min}[\hat{\mathbf{J}}(\mathbf{q})\hat{\mathbf{J}}^T(\mathbf{q})] - \beta] \\ & - \alpha[\|\hat{\mathbf{J}}(\mathbf{q})(\mathbf{C} + \mathbf{K}_d)\| + \|\mathbf{M}\hat{\mathbf{J}}^T(\mathbf{q})\|]\}\|\Delta\mathbf{x}\|^2 \end{aligned} \quad (5.17)$$

So if α is chosen small enough, \mathbf{K}_p and \mathbf{K}_d are chosen large enough, the following conditions can be satisfied for a certain range of kinematics estimation error β :

$$\begin{aligned} & 2\lambda_{\min}[\mathbf{C} + \mathbf{K}_d] - \mathbf{K}_p\beta - \alpha[2\|\mathbf{M}\hat{\mathbf{J}}^T(\mathbf{q})\mathbf{J}(\mathbf{q})\| \\ & + \|\hat{\mathbf{J}}(\mathbf{q})(\mathbf{C} + \mathbf{K}_d)\| + \|\mathbf{M}\hat{\mathbf{J}}^T(\mathbf{q})\|] \geq 0 \end{aligned} \quad (5.18)$$

$$\begin{aligned} & \mathbf{K}_p[2\lambda_{\min}[\hat{\mathbf{J}}(\mathbf{q})\hat{\mathbf{J}}^T(\mathbf{q})] - \frac{\beta}{\alpha}] - [\|\hat{\mathbf{J}}(\mathbf{q})(\mathbf{C} + \mathbf{K}_d)\| \\ & + \|\mathbf{M}\hat{\mathbf{J}}^T(\mathbf{q})\|] \geq 0 \end{aligned} \quad (5.19)$$

such that $\dot{V} \leq 0$.

Considering that V is positive definite, according to Invariant Set Theorem [Slotine and Li, 1991], it can be concluded from (5.17) that $\dot{\mathbf{q}} \rightarrow 0$ and $\Delta\mathbf{x} \rightarrow 0$ asymptotically.

Remark 5.1: From conditions (5.18) and (5.19), it can be seen that the proposed method can handle kinematics error but with certain range. When the kinematics estimation error is too big, meaning β is big, the two conditions may no longer be satisfied and the system performance is not guaranteed, which is logical that automatic controller cannot handle infinite large modelling errors without online updation or adaptation that lead to more complicated

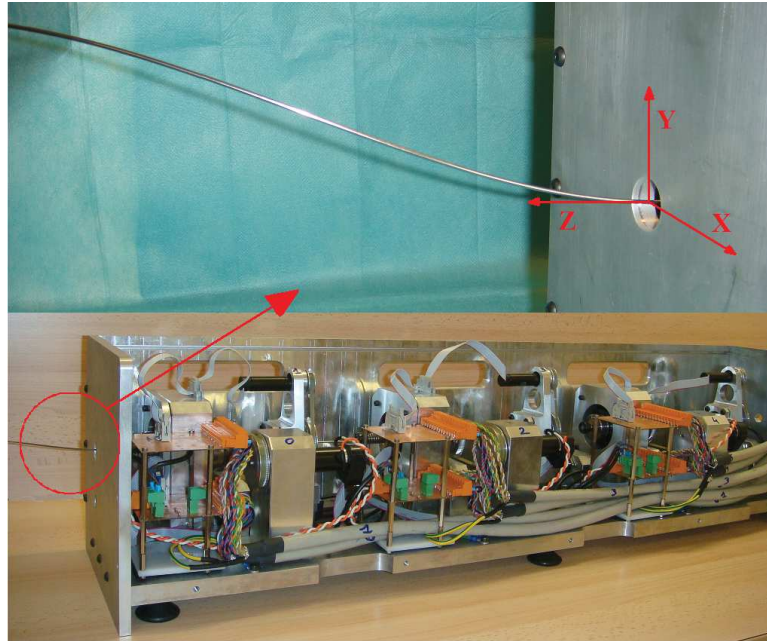


Figure 5.2 – CTR Prototype: (top) Zoomed in picture of the concentric tubes (bottom) Whole system with actuators.

control design. On the other hand, it should be noted that the Lyapunov analysis is very conservative and so are the conditions deduced meaning that in many cases even if conditions (5.18) and (5.19) are not satisfied the control task could be still achieved.

Remark 5.2: Although the proposed actuator current control input also possesses a PID form, it is totally different from the PID control of the actuator which is used to generate the calculated joint position as in inverse kinematics based methods. The difference lies in that the proposed PID actuator controller takes no desired actuator joint position through inverse kinematics as reference but the direct operational space positioning error as feedback signal, and this makes the difference between joint-space controller and task-space controller.

5.4 Simulation studies

Simulation studies have been carried out based on the mechanical design of the CTR prototype shown in Figure 5.2. The prototype is composed of three pre-curved Nitinol tubes with each driven by two motors for 2 DOFs (rotation and translation). Simulation study is

carried out to evaluate the performance of the proposed control method in this chapter. In this simulation study, the position control task with the first two tubes is investigated. The workspace of the two-tube CTR is shown in Figure 5.3.

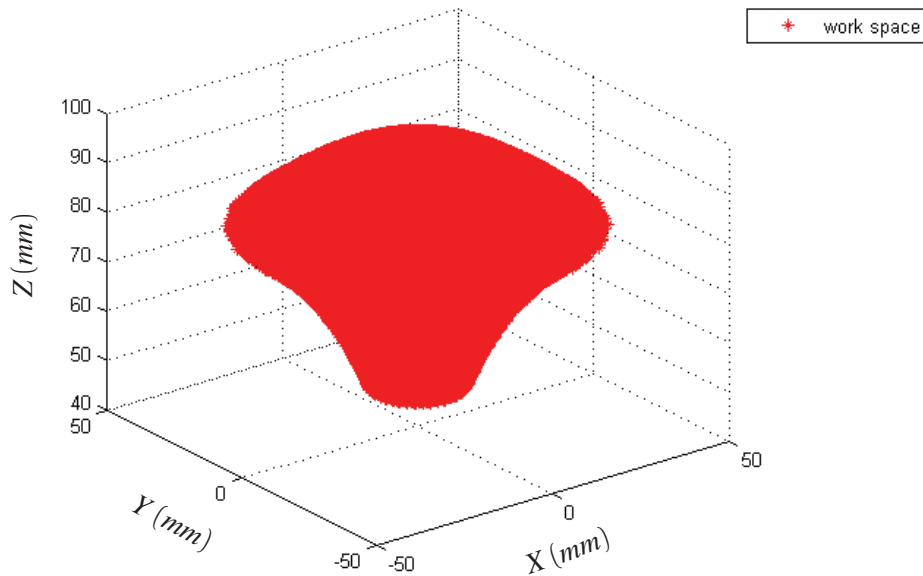


Figure 5.3 – Workspace

In this simulation, two kinematic models are used: the Transmissional Torsion Model (TTM) as the true kinematic model for forward kinematics calculation to feedback the position, and the simpler and less accurate Torsion-Free Model (TFM) which is assumed to be the model that is known to the designer and used to carry out the inverse kinematics based control. These two models with different accuracy are used to simulate the case of inaccurate modelling. Based on TFM the Jacobian matrix is calculated which represents the inaccurate Jacobian used in the proposed actuator current input design and in the inverse kinematic control. Here the more accurate but more complicated torsionally compliant model is not used as the true kinematics model since the purpose of this simulation study is to investigate the capability of the proposed control method in handling kinematics inaccuracy, in this sense the choice of true model does not make real difference as both are simplified approximations of the reality.

Simulation studies are carried out to compare the performances of the traditional inverse kinematics based control method with the proposed task-space controller in face of different kinematics uncertainties.

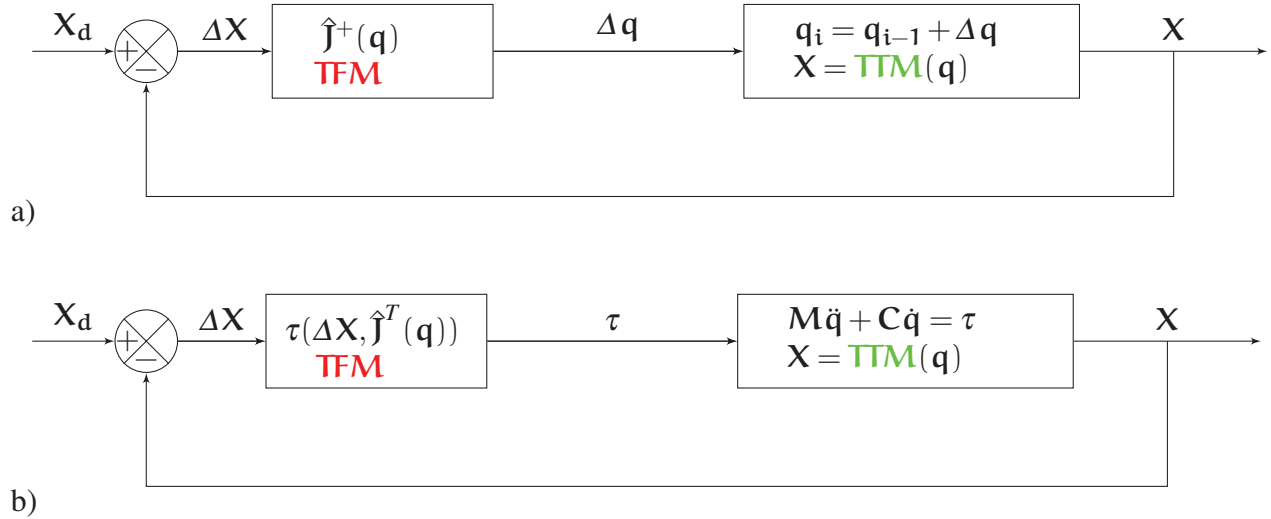


Figure 5.4 – Control schemes: a) Inverse kinematic control, b) Task-space control

The Tubes parameters used in this comparison simulation between task-space control and inverse kinematics control are given in Table 5.1.

Table 5.1 – Tubes parameters.

	Outer tube	Inner tube
Outer diameter (<i>mm</i>)	1,63	1,05
Inner diameter (<i>mm</i>)	1,12	0.61
Young modulus (<i>GPa</i>)	50	50
Shear modulus (<i>GPa</i>)	19,23	19,23
Length of the straight part (<i>mm</i>)	70	359
Length of the curved part (<i>mm</i>)	30	50

For inverse kinematics (IK) based control method (see Figure 5.4.a), the Cartesian errors are converted to joint errors through the pseudo inverse of the Jacobian matrix which is based on the TFM. The corresponding actual task-space positions are calculated through the TTM

forward kinematics which is considered as the true model, and then task-space position errors are fed back to update the joint variables through TFM inverse kinematics in order to reach next desired position.

For the task-space (TS) control proposed, the torques are calculated using the transpose of the Jacobian matrix, the Cartesian errors, and the joint velocities. The Jacobian is calculated based on the TFM model and the Cartesian position feed-back are calculated by the TTM model after integration of the actuators dynamics. The actuator dynamics parameters used are the same as calibrated from the real prototype.

For the position control task, the desired trajectory is defined by 40 points in cannula base frame (as seen in Figure 5.2) along a circular trajectory of 10 mm radius which is within the workspace and defined by:

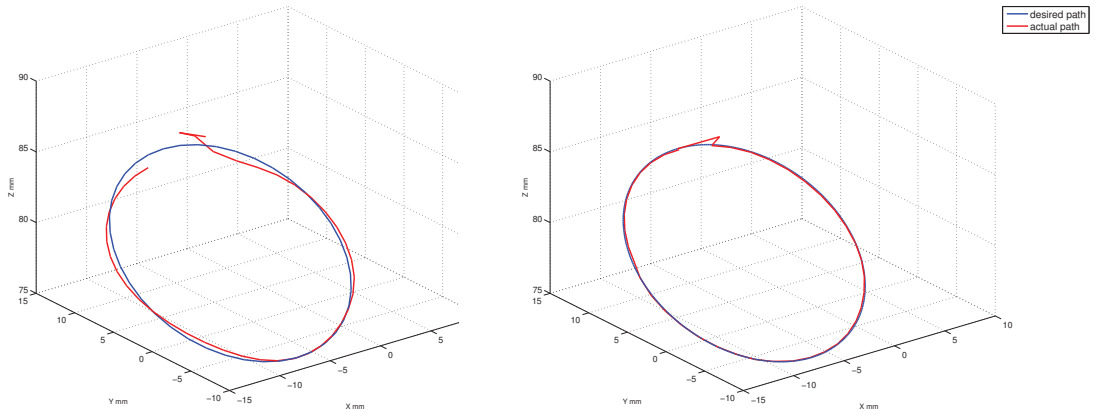
$$x_d = 10\cos\phi, y_d = 5\sqrt{3}\sin\phi - 40, z_d = 5\sin\phi + 40\sqrt{3}. \quad (5.20)$$

A position sensor is assumed to be available to provide online update of task-space positioning errors (in simulation, this information is provided by the TTM model) and it is also assumed that this sensor information is used in the inverse kinematic calculation at the same sampling frequency.

Two types of simulations have been carried out to compare the position control performance of the two control strategies used (IK control and TS control):

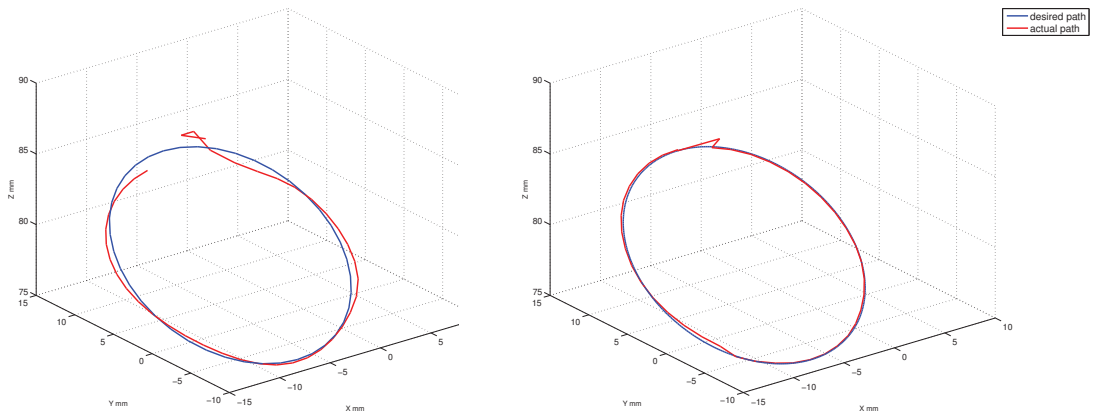
- In the first type of simulation study, the same kinematic model (TFM) is used for both control methods and no kinematics parameter inaccuracy is considered.
- In the second type of simulation study, except using the same simplified model (TFM), kinematics parameter inaccuracy is also introduced to show the control performance of both methods against both structural and parametric inaccuracies in kinematics.

By using the control algorithm proposed as (5.6), the control performances of the task-space approximate Jacobian position control method with the same kinematic uncertainties as for inverse kinematics based control method are illustrated in Figure 5.5 and Figure 5.6. It is seen that the first type of simulation results are illustrated in Figure 5.5.a and 5.5.b. In Figure 5.5.c-f and Figure 5.6, kinematic parameter inaccuracies of deferent levels (on tube curvatures k_1 and k_2) are also included.



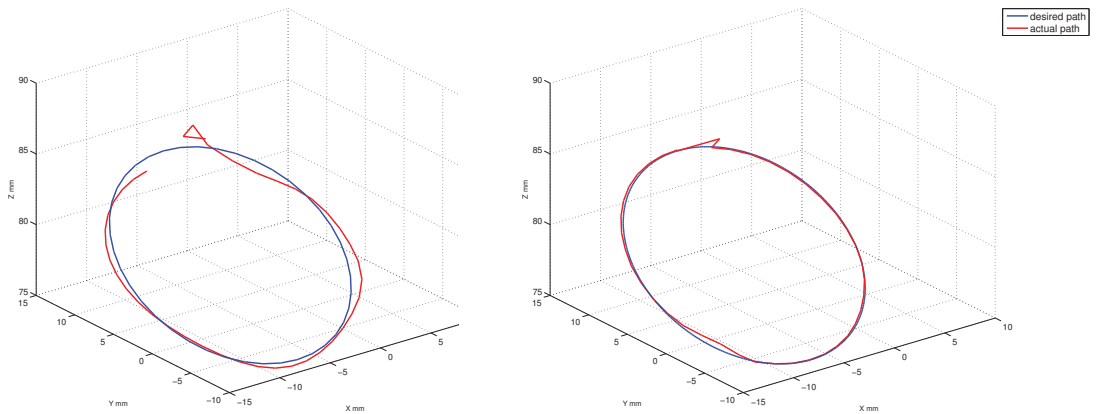
(a) IK Control with only modelling difference inaccuracy.

(b) TS Control with only modelling difference inaccuracy.



(c) IK Control with $(k'_1 = 90\% \cdot k_1)$

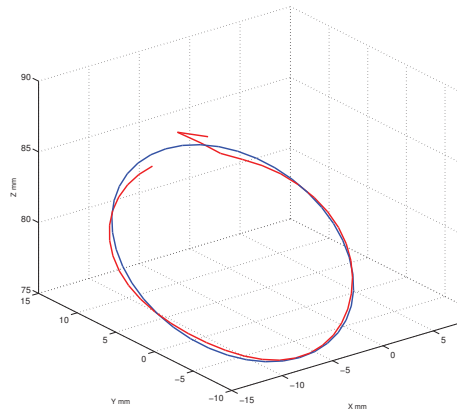
(d) TS Control with $(k'_1 = 90\% \cdot k_1)$



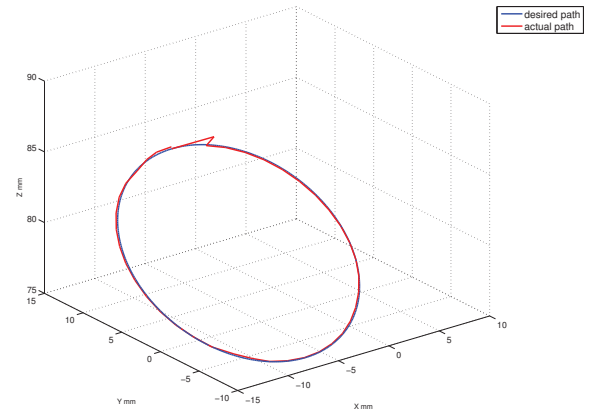
(e) IK Control with $(k'_1 = 80\% \cdot k_1)$

(f) TS Control with $(k'_1 = 80\% \cdot k_1)$

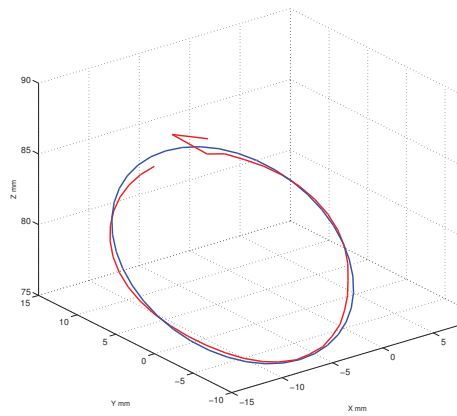
Figure 5.5 – The performances of the two control strategies with modelling inaccuracy and uncertainty in the parameter k_1 .



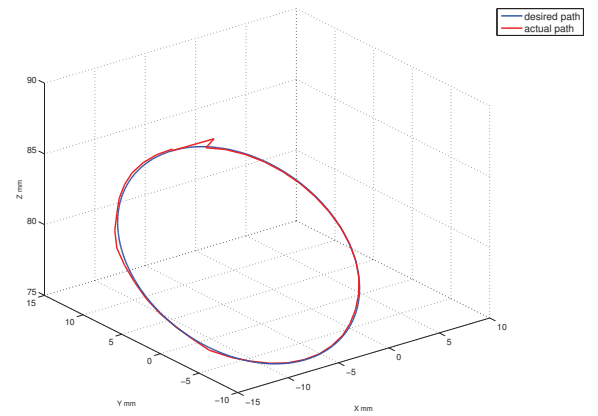
(a) IK Control with $(k'_2 = 90\% \cdot k_2)$



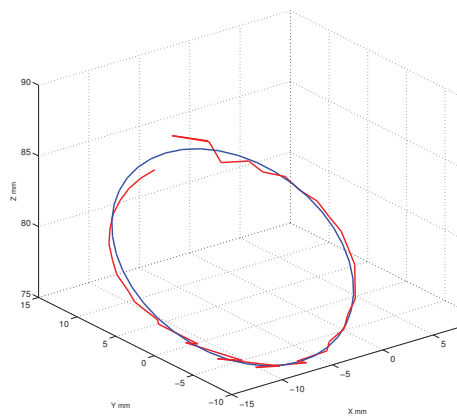
(b) TS Control with $(k'_2 = 90\% \cdot k_2)$



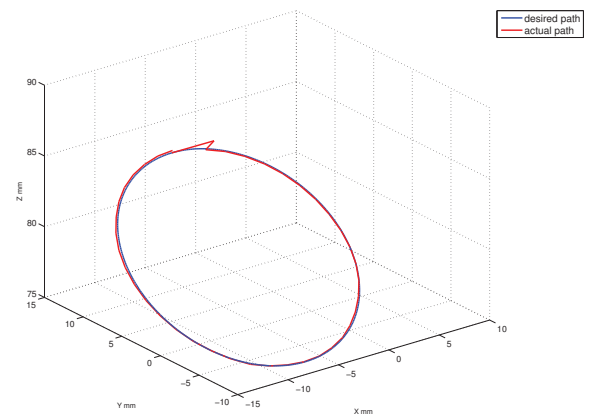
(c) IK Control with $(k'_2 = 80\% \cdot k_2)$



(d) TS Control with $(k'_2 = 80\% \cdot k_2)$



(e) IK Control with $(k'_1 = 80\% \cdot k_1, k'_2 = 80\% \cdot k_2)$



(f) TS Control with $(k'_1 = 80\% \cdot k_1, k'_2 = 80\% \cdot k_2)$

Figure 5.6 – The performances of the two control strategies with modelling inaccuracy and uncertainty in the parameter k_1 and k_2 .

To evaluate the performances of each control strategy, the Cartesian Root Mean Square Errors (RMSE) along X, Y, Z axis of task space axis are calculated in all cases of study presented above and shown in the Table 5.2.

Table 5.2 – Comparison of Position Errors (mm) using two control strategies: Inverse Kinematics (IK) Control and Task-space (TS) Control

Case studied	$RMSE_X$	$RMSE_Y$	$RMSE_Z$	$RMSE$
IK Control with: $(k'_1 = k_1, k'_2 = k_2)$	3.7437	2.4769	3.3830	5.6209
TS Control with: $(k'_1 = k_1, k'_2 = k_2)$	0.7435	0.4714	0.4647	0.9955
IK Control with: $(k'_1 = 90\% \cdot k_1, k'_2 = k_2)$	3.9103	2.9382	3.6250	6.0880
TS Control with: $(k'_1 = 90\% \cdot k_1, k'_2 = k_2)$	0.7614	0.4838	0.4382	1.0029
IK Control with: $(k'_1 = 80\% \cdot k_1, k'_2 = k_2)$	4.1804	3.5221	3.9358	6.7358
TS Control with: $(k'_1 = 80\% \cdot k_1, k'_2 = k_2)$	0.8030	0.5559	0.4535	1.0768
IK Control with: $(k'_1 = k_1, k'_2 = 90\% \cdot k_2)$	3.9164	2.4392	3.1100	5.5642
TS Control with: $(k'_1 = k_1, k'_2 = 90\% \cdot k_2)$	0.7636	0.4931	0.5107	1.0426
IK Control with: $(k'_1 = k_1, k'_2 = 80\% \cdot k_2)$	4.3173	2.7052	2.8775	5.8513
TS Control with: $(k'_1 = k_1, k'_2 = 80\% \cdot k_2)$	0.8148	0.4909	0.5581	1.1029
IK Control with: $(k'_1 = 80\% \cdot k_1, k'_2 = 80\% \cdot k_2)$	5.4901	4.8975	3.3537	8.0854
TS Control with: $(k'_1 = 80\% \cdot k_1, k'_2 = 80\% \cdot k_2)$	0.8080	0.5747	0.5023	1.1115

It can be seen from the Table 5.2 that the Cartesian RMSE for the case of task-space control is in range of 0.9 mm and 1.1 m when the kinematic uncertainties increase. This RMSE is in the rage of 5 mm and 8 m for the case of inverse kinematics control. This means that the impact of kinematics inaccuracy is much higher on the inverse kinematic control (from 5 to 8 mm) than on the proposed task-space controller (from 0.9 to 1.1 mm). Figure 5.8 shows the CTR shape evolution (6 shapes chosen) along the circular trajectory for the simulation study 5.5.a-b of the proposed control method. The shapes are numbered following the time sequence.

From Figure 5.5, Figure 5.6, and Table 5.2, it can be concluded that with the presence of kinematics modelling error, the task-space approximate Jacobian control method provides better positioning performance over inverse kinematics based control method.

It is also noted that once the kinematic inaccuracies exceed certain limit, the position diverges as can be seen from Figure 5.7. This observation is consistent with the theoretical

analysis presented before: the proposed control method can only tolerate uncertainty (β) to certain level as specified by conditions (5.18) and (5.19) which is natural as no control method can tolerate infinitely large uncertainties. As the theoretical based on Lyapunov method which is conservative, the exact value (threshold) of kinematic inaccuracy can not be explicitly calculated.

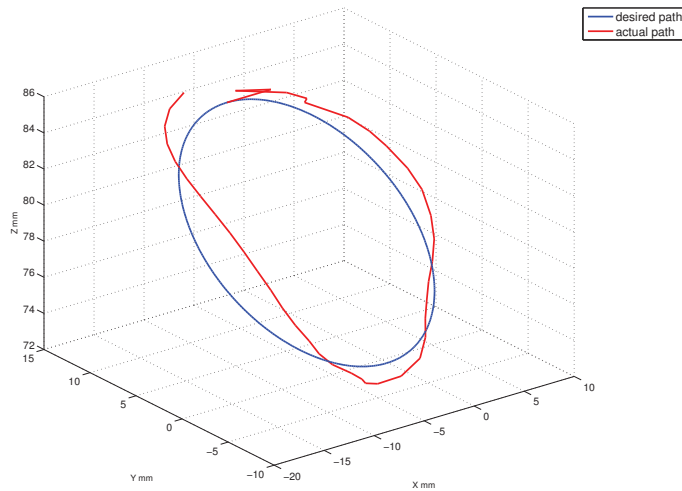


Figure 5.7 – TS Control with ($k'_1 = 60\% \cdot k_1, k'_2 = 60\% \cdot k_2$). The upper limit of the kinematic uncertainties bound is exceeded, and thus the tip position diverges.

Remark 5.3: Although in this simulation study the inverse kinematics based control performance using TFM model is shown for comparison, it does not mean that proposed method is compared to this specific model. In fact, through the simulation study we want to show the fact that with the existence of kinematics modelling error, which is the case for all existing kinematics models, the proposed method can provide automatic compensation at the actuation level to achieve the control task. As mentioned in the introduction, although with manual compensation of the surgeon existing models may be enough for current teleoperated control task, it is still desirable if this manual compensation work could be left to the lower level motion controller such that the surgeon can operate in more intuitive way. To achieve that, the control design should provide the robotic instrument capabilities to tolerate uncertainties and disturbances within certain extent.

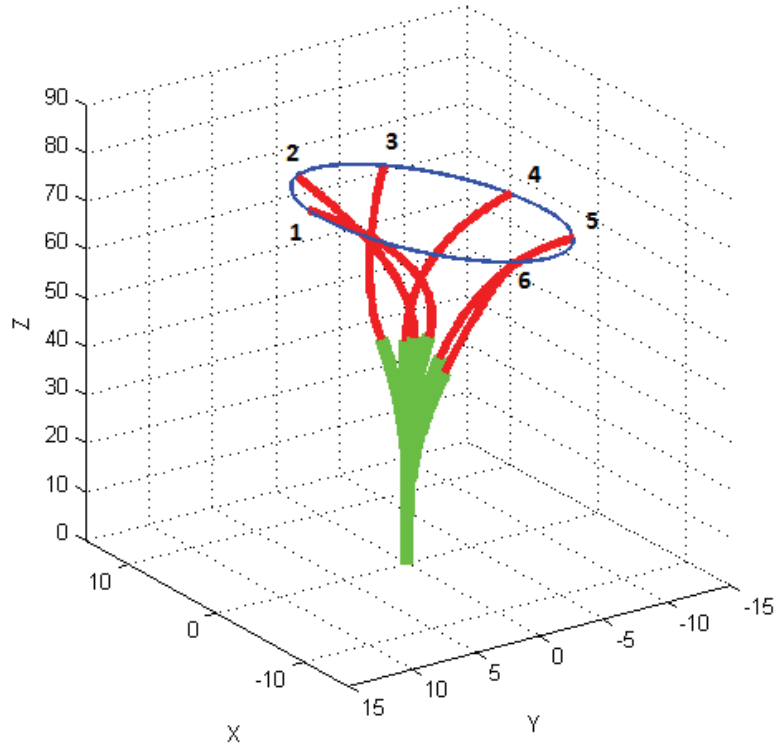


Figure 5.8 – CTR Shape During Control

Remark 5.4: The proposed control method relies on Jacobian matrix of the concentric-tube robot. It is noticed that for most existing kinematics models the Jacobian matrix, i.e. the mapping from the operational space velocity to joint velocity, can be obtained. For very complicated models (existing or to come), an optimized approximation could be used for the Jacobian matrix. In any case, as shown in this work, the proposed control method may work with only an approximated Jacobian without need of exact kinematic information.

5.5 Conclusion

Existing motion control methods for concentric-tube robot are mainly based on inverse kinematics calculation which is prone to inaccuracy in kinematics modelling. Moreover, the use of the most accurate kinematic model is complex and time consuming. Through this work,

we show that this problem can be tackled by using the approximate Jacobian matrix and direct measurement of operational space error in the actuator control input design. The positioning errors are guaranteed to converge asymptotically through rigorous Lyapunov analysis given that the control parameters are properly chosen to satisfy certain conditions. Therefore, accurate CTR motion control can be realized without resorting to highly complicated kinematic model but a simpler alternative, which represents the biggest advantage of this method. This result presents a new control method that has not been explored for concentric-tube robot motion control. It is verified through simulation studies that the control performance of the proposed method with the presence of kinematics inaccuracy is better than inverse kinematics based method.

Conclusions and Perspectives

6.1 Conclusions

In this thesis, the principle of CTR has been explained and existing research CTR works in literature have been presented. Mainly the CTR research works can be categorized into: the design of actuation unit and tubes; the kinematic modelling; the path planning and the control. The works on tubes design and path planning are usually associated to a given surgical application. The tube design works optimize the dimensions of the tubes according to the surgical work space and the anatomical constraints. Feasibility of using CTR in various surgical applications (lung biopsy, neuro-surgery, etc) has been studied and validated through *in vivo* tests for some prototypes.

The forward, inverse, and differential kinematic models have been presented with details. The evolution of kinematic modelling from assuming infinite stiffness of the outer tube to introducing the bending and torsion tubes interaction in the model and the cause and effect of ‘bifurcations’ have been presented.

After literature survey and fundamental knowledge introduction, two contributions have been presented in this thesis. The first one is a concept study of using CTR for frontal lobe tumor removal. An optimization algorithm based on grid-searching Pareto technique which allows to avoid the limitations of scalarization techniques used in literature has been used se-

lect tube dimension parameters in order to maximize the reachability of the desired workspace and to maximize the elastic stability. A new prototype has been designed to satisfy this specific surgical application requirements (way of tubes insertion, translations dimensions, number of tubes etc).

The second contribution is about compensation of kinematic modelling error from the actuator control input level and avoiding the inverse kinematics calculation for traditional CTR motion control. This contribution is motivated by the fact that the kinematic modelling of CTR is challenging because of complicated physical phenomena caused by the elasticity interaction between tubes. A new control method from the actuator level has been proposed and has shown that the control design of actuator input in task-space with approximate Jacobian matrix provides more flexibility and robustness in handling inaccuracy in kinematic model since no accurate Jacobian matrix is obligatory. It has been shown through simulation study that the proposed control method presents better performance compared with traditional inverse kinematics based control method used in literature in face of kinematics inaccuracy.

6.2 Perspectives

As a new area of research in medical robotics, many issues in design, modelling, sensing and control are still open. For all existing prototypes, the actuation unit is not optimized to meet the requirements of the considered surgical application, e.g. limited space inside MRI tunnel. Compact robot design in weight, length, form, and assembly/disassembly in the operating room is required which can be one of the future directions in CTR design. Regarding optimization of the tubes design, other parameters such as the outer and the inner diameter can be added to the decision space. Moreover, the dexterity and force generation of the end-effector are also important criteria to evaluate the performance capability. They can be introduced in the objective function of design optimization algorithms. As for material of the robot tube, rather than Nitinol, other materials may be used such as thermoplastic materials. The work of [Amanov et al., 2015] is a start of this new research direction in CTR design. Other materials could offer full elastically stable workspace. Sensing system, visual systems are usually used to feedback the robot shape (eg. in [Croom et al., 2010]), however, during the navigation the robot is not visible. The interventional MRI feedback or even 3D Ultrasound

feedback [Ren and Dupont, 2012] are known to be slow for real-time applications. For this reason, other shape detection sensors embedded in the robot could be used while considering the complexity of integration inside the tubes of small diameter. For CTR motion control, the work presented in [Kim et al., 2015] shows the promising use of adaptive laws in future either at the kinematic stage or at the control level in real-time for enhancing position control performances of CTR.

In future, the following works are considered to be further pursued :

- Lab experimental tests are scheduled as a direct continuity of this work. The tubes are to be curved accordingly to the obtained optimal curvatures in order to validate the concept of the addressed surgical procedures. For the second contribution of this thesis, the kinematic modelling has already been implemented in the real platform. The controller proposed is to be implemented and compared to the inverse kinematic control.
- In the preliminary tests, it is noticed that the effect of frictions existing in the system is quite significant. Future works will investigate how to deal with system frictions and improve operation accuracy and safety.
- An extension of the optimization algorithm used in this work will be proposed by including the outer and inner diameters of the tubes in the decision space and by considering dexterity in the objective space.
- Adaptive control for CTR is to be studied which is another strategy to compensate the kinematic inaccuracies. The unknown dynamics of the system can be estimated and adapted in real-time. The obtained results will be compared to the second contribution presented in this thesis.

LIRMM CTR Prototype

In LIRMM, a latest CTR prototype has been designed and assembled for future experimental test. The complete system setup is shown in Figure A.1.

In this appendix, the technical documents of the motors, controllers, sensors, gears, communication loop, and the CAD prototype design are presented.



Figure A.1 – System setup of CTR.

A.1 CAD design

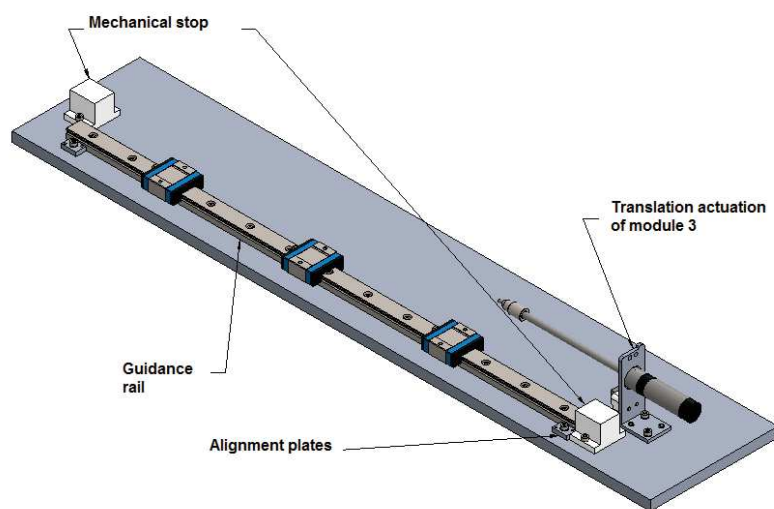


Figure A.2 – Base structure of the CTR robot.

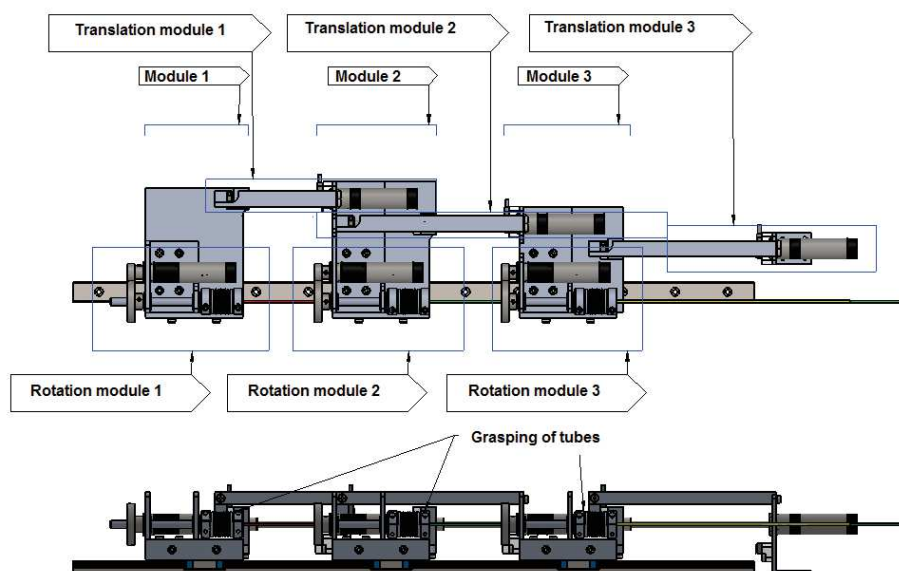


Figure A.3 – Side and top view of the CTR robot.

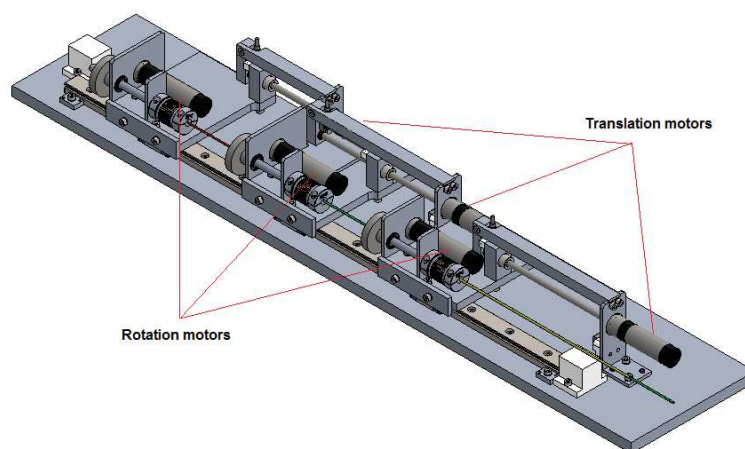
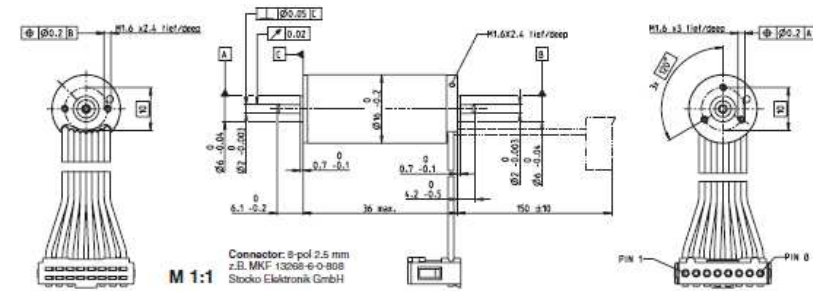


Figure A.4 – CAD of the assembled CRT under Solidworks.

A.2 Motors used

A.2.1 Translation motors: ref. 283833

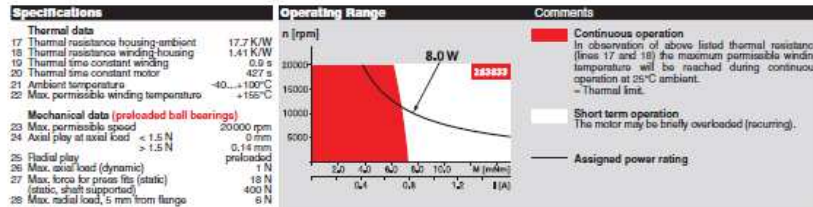
EC-max 16 Ø16 mm, brushless, 8 Watt



maxon EC-max

	283831	283832	283833	283834	283835
--	--------	--------	--------	--------	--------

Motor Data	283831	283832	283833	283834	283835	
Values at nominal voltage						
1 Nominal voltage	V	6	9	12	18	24
2 No load speed	rpm	12000	11900	11900	11900	11900
3 No load current	mA	430	85.1	64.2	42.6	31.9
4 Nominal speed	rpm	7120	7090	7300	7170	7350
5 Nominal torque (max. continuous torque)	mNm	7.96	7.8	8.05	7.87	8.19
6 Nominal current (max. continuous current)	A	1.75	1.17	0.909	0.593	0.461
7 Stall torque	mNm	10.2	10.6	21.1	20.3	22
8 Starting current	A	4.17	2.82	2.27	1.45	1.17
9 Max. efficiency	%	69	69	70	70	71
Characteristics						
10 Terminal resistance phase to phase	Ω	1.44	3.19	5.3	12.4	20.5
11 Terminal inductance phase to phase	mH	0.0343	0.0753	0.14	0.317	0.566
12 Torque constant	mNm/A	4.61	7.02	9.32	14	18.7
13 Speed constant	rpm/V	2070	1360	1020	681	510
14 Speed/torque gradient	rpm/mNm	646	619	582	662	556
15 Mechanical time constant	ms	5.75	5.51	5.18	5.36	4.95
16 Rotor inertia	gcm ²	0.85	0.85	0.85	0.85	0.85



maxon Modular System

- 1 Planetary Gearhead: Ø16 mm, 0.2 - 0.6 Nm, Page 255
- 2 Planetary Gearhead: Ø16 mm, 0.5 - 2.0 Nm, Page 286
- 3 Spindle Drive: Ø16 mm, Page 206-208
- 4 Spindle Drive: Ø20 mm, Page 209/300

Overview on page 20 - 25

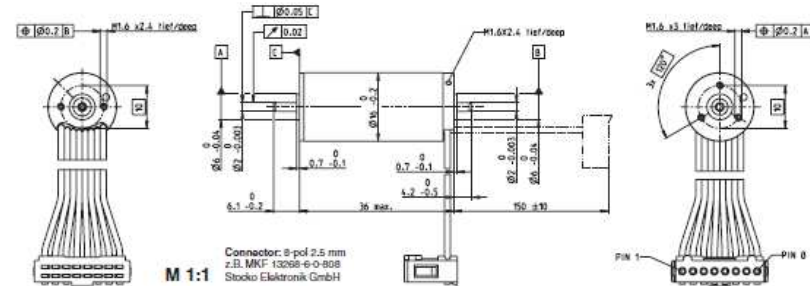
- Encoder MR: 129/296/12 CPT, 2/3 channels, Page 318
- Recommended Electronics:
 - ESCON 36/3 EC: Page 342
 - ESCON Mod 50/4 EC 5: 343
 - ESCON Modulo 50/5: 343
 - ESCON 50/5: 344
 - DEC Modulo 24/2: 348
 - EPOS2 24/2: 350
 - EPOS2 Modulo 36/2: 350
 - EPOS2 70/10 EtherCAT: 357
 - MAXPOS 50/5: 360
 - Notes: 24

Apr 2014 edition / subject to change

maxon EC motor 201

A.2.2 Rotation motors: ref. 283833

EC-max 16 Ø16 mm, brushless, 8 Watt



maxon EC-max

Part Numbers	283831	283832	283833	283834	283835
--------------	--------	--------	--------	--------	--------

Motor Data		283831	283832	283833	283834	283835
Values at nominal voltage						
1 Nominal voltage	V	6	9	12	18	24
2 No load speed	rpm	12000	11000	11000	11900	11900
3 No load current	mA	130	85.1	64.2	42.6	31.9
4 Nominal speed	rpm	7120	7090	7300	7170	7350
5 Nominal torque (max. continuous torque)	mNm	7.66	7.8	8.02	7.87	8.19
6 Nominal current (max. continuous current)	A	1.76	1.17	0.909	0.593	0.461
7 Stall torque	mNm	19.2	19.8	21.1	20.3	22
8 Starting current	A	4.17	2.82	2.27	1.45	1.17
9 Max. efficiency	%	69	69	70	70	71
Characteristics						
10 Terminal resistance phase to phase	Ω	3.44	3.19	5.3	12.4	20.5
11 Terminal inductance phase to phase	mH	0.0343	0.0793	0.14	0.317	0.546
12 Torque constant	mNm/A	4.61	7.02	9.32	14	18.7
13 Speed constant	rpm/V	2070	1360	1020	681	510
14 Speed/torque gradient	rpm/mNm	646	619	582	602	556
15 Mechanical time constant	ms	5.75	5.51	5.18	5.36	4.95
16 Floor inertia	gcm ²	0.85	0.85	0.85	0.85	0.85

Specifications	Operating Range	Comments
Thermal data 17 Thermal resistance housing-ambient 17.7 K/W 18 Thermal resistance winding-housing 1.41 K/W 19 Thermal time constant winding 0.3 s 20 Thermal time constant motor 427 s 21 Ambient temperature -40...+100°C 22 Max. permissible winding temperature +155°C Mechanical data (preloaded ball bearings) 23 Max. permissible speed 20000 rpm 24 Axial play at axial load < 1.5 N 0 mm 0.14 mm preloaded 25 Radial play 1 N 26 Max. axial load (dynamic) 18 N 27 Max. force for press fit (static) (static, shaft supported) 400 N 28 Max. radial load, 5 mm from flange 8 N Other specifications 29 Number of pole pairs 1 30 Number of phases 3 31 Weight of motor 52 g Values listed in the table are nominal. Connection (Cable AWG 24) brown Motor winding 1 Pin 1 red Motor winding 2 Pin 2 orange Motor winding 3 Pin 3 yellow V _{reg} 3...24 VDC Pin 4 green GND Pin 5 Blue Hall sensor 1 Pin 6 violet Hall sensor 2 Pin 7 grey Hall sensor 3 Pin 8 Wiring diagram for Hall sensors see p. 33		<p>Continuous operation In observation of above listed thermal resistance (lines 17 and 18) the maximum permissible winding temperature will be reached during continuous operation at 25°C ambient. - Thermal limit.</p> <p>Short term operation The motor may be briefly overloaded (recurring).</p> <p>— Assigned power rating</p>

maxon Modular System

- Planetary Gearhead Ø16 mm, 0.2 - 0.6 Nm, Page 255
- Planetary Gearhead Ø22 mm, 0.5 - 2.0 Nm, Page 255
- Spindle Drive Ø16 mm, Page 206-208
- Spindle Drive Ø22 mm, Page 209/200

Overview on page 20 - 26

- Encoder MR 129/255 12 CPT, 2/3 channels, Page 318

Recommended Electronics:

- ESCON 36/3 EC Page 342
- ESCON Mod. 50/4 EC-S Page 343
- ESCON Module 50/S Page 343
- ESCON 50/S Page 344
- DEC Module 24/2 Page 348
- EPOS2 24/2 Page 350
- EPOS3 20/10 EtherCAT Page 357
- MAXPOS 50/S Page 360
- Notes Page 24

A.3 Gears connected to the motors

A.3.1 Gears connected to the translation motors

Planetary Gearhead GP 26 B Ø26 mm, 0.5–2.0 Nm
Ceramic Version

NRND Design 03
Not recommended for new design

Technical Data

Planetary Gearhead	straight tooth
Output shaft	stainless steel, hardened
Bearing at output	ball bearing
Radial play, 10 mm from flange	max. 0.08 mm
Axial play at axial load	< 4 N 0 mm
Max. permissible axial load	> 4 N max. 0.05 mm
Max. permissible force for press fits	100 N
Sense of rotation, drive to output	=
Recommended input speed	< 9000 rpm
Recommended temperature range	-40...+100°C
Number of stages	1 2 3 4 5
Max. radial load, 10 mm from flange	60 N 90 N 100 N 100 N 100 N

Part Numbers

	144026	144029	144036	144041	144045	144051	144057	144059	144066	144072	144078
1 Reduction	3.8:1	14:1	53:1	104:1	108:1	370:1	500:1	742:1	1386:1	1098:1	3189:1
2 Reduction absolute	14:1	53:1	104:1	108:1	370:1	500:1	742:1	1386:1	1098:1	3189:1	
3 Max. motor shaft diameter	4 mm	4 mm	4 mm	3.2 mm	4 mm	3.2 mm	4 mm	4 mm	3.2 mm	3.2 mm	4 mm
Part Numbers	144027	144030	144036	144042	144046	144052	144058	144061	144067	144073	144079
1 Reduction	4.4:1	16:1	62:1	100:1	231:1	380:1	600:1	867:1	1460:1	2102:1	3728:1
2 Reduction absolute	16:1	62:1	100:1	100:1	231:1	380:1	600:1	867:1	1460:1	2102:1	3728:1
3 Max. motor shaft diameter	3.2 mm	3.2 mm	3.2 mm	4 mm	3.2 mm	3.2 mm	3.2 mm	3.2 mm	3.2 mm	3.2 mm	3.2 mm
Part Numbers	144028	144031	144037	144043	144047	144053	144060	144062	144068	144074	144080
1 Reduction	5.4:1	19:1	72:1	128:1	270:1	410:1	650:1	1014:1	1538:1	2214:1	4502:1
2 Reduction absolute	19:1	72:1	128:1	128:1	270:1	410:1	650:1	1014:1	1538:1	2214:1	4502:1
3 Max. motor shaft diameter	2.5 mm	3.2 mm	3.2 mm	3.2 mm	3.2 mm	4 mm	2.5 mm	3.2 mm	4 mm	4 mm	2.5 mm
Part Numbers	144032	144038	144044	144048	144054			144063	144069	144075	
1 Reduction	20:1	76:1	157:1	285:1	455:1			1088:1	1621:1	2458:1	
2 Reduction absolute	76:1	157:1	157:1	285:1	455:1			1088:1	1621:1	2458:1	
3 Max. motor shaft diameter	4 mm	4 mm	2.5 mm	4 mm	3.2 mm			4 mm	3.2 mm	3.2 mm	
Part Numbers	144033	144039		144049	144055			144064	144070	144076	
1 Reduction	24:1	84:1		116:1	470:1			1185:1	1707:1	2550:1	
2 Reduction absolute	84:1	84:1		116:1	470:1			1185:1	1707:1	2550:1	
3 Max. motor shaft diameter	3.2 mm	3.2 mm		3.2 mm	3.2 mm			3.2 mm	3.2 mm	3.2 mm	
Part Numbers	144034	144040		144050	144056			144065	144071	144077	
1 Reduction	29:1	80:1		333:1	561:1			1240:1	1798:1	3027:1	
2 Reduction absolute	80:1	80:1		333:1	561:1			1240:1	1798:1	3027:1	
3 Max. motor shaft diameter	2.5 mm	3.2 mm		3.2 mm	3.2 mm			3.2 mm	3.2 mm	3.2 mm	
4 Number of stages	1	2	3	3	4	4	4	5	5	5	5
5 Max. continuous torque	Nm	0.5	0.6	1.3	1.3	1.9	1.9	2.0	2.0	2.0	2.0
6 Intermittently permissible torque at gear output	Nm	0.8	0.9	1.8	1.9	2.7	2.7	3.0	3.0	3.0	3.0
7 Max. efficiency	%	84	70	50	50	40	40	42	42	42	42
8 Weight	g	65	86	108	108	130	130	152	152	152	152
9 Average backlash no load	°	1.0	1.2	1.8	1.6	2.0	2.0	2.0	2.0	2.0	2.0
10 Max inertia	gcm ²	0.6	0.5	0.4	0.4	0.4	0.4	0.4	0.4	0.4	0.4
11 Gearhead length L1*	mm	29.2	36.0	42.8	42.8	49.6	49.6	56.4	56.4	56.4	56.4

* For A-max 26 and HED 5540 L1 19-22 mm

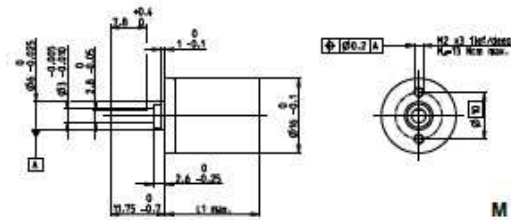
Overall length [mm]

Motor	Page	Sensor/Brake	Page	Overall length [mm]	Motor length	gearhead length	flange offset	assembly pitch
RE 25	06/101		302	83.8	90.6	97.4	97.4	104.2
RE 25	06/101	MR	302	94.8	101.6	108.4	108.4	115.2
RE 25	06/101	Enc 22	304	97.9	104.7	111.5	111.5	118.3
RE 25	06/101	HED_5540	306/307	104.6	111.4	118.2	118.2	125.0
RE 25	06/101	DCT22	315	106.1	112.9	119.7	119.7	126.5
RE 25, 20 W	100		302	72.3	79.1	85.9	85.9	92.7
RE 25, 20 W	100	MR	302	83.3	90.1	96.9	96.9	103.7
RE 25, 20 W	100	HED_5540	306/309	93.1	99.9	106.7	106.7	113.5
RE 25, 20 W	100	DCT22	315	94.6	101.4	108.2	108.2	115.0
RE 25, 20 W	100	AG 26	348	106.4	113.2	120.0	120.0	126.8
RE 25, 20 W	100	HED_5540 / AB 28	306/348	123.6	130.4	137.2	137.2	144.0
RE 25, 20 W	101	AB 28	346	117.9	124.7	131.5	131.5	138.3
RE 25, 20 W	101	HED_5540 / AB 28	307/348	135.1	141.9	148.7	148.7	155.5
A-max 26	126-132		314	71.8	78.6	85.4	85.4	92.2
A-max 26	126-132	MEnc 13	314	78.9	85.7	92.5	92.5	99.3
A-max 26	126-132	MR	302	80.8	87.4	94.2	94.2	101.0
A-max 26	126-132	Enc 22	304	86.2	93.0	99.8	99.8	106.6
A-max 26	126-132	HED_5540	306/307	90.2	97.0	103.8	103.8	110.6
RE-max 29	155-158		302	71.8	78.6	85.4	85.4	92.2
RE-max 29	158/158	MR	302	80.8	87.4	94.2	94.2	101.0

382 mazon special program June 2013 edition / subject to change

A.3.2 Gears connected to the rotation motors

Planetary Gearhead GP 16 A $\varnothing 16$ mm, 0.1–0.3 Nm



Technical Data	
Planetary Gearhead	straight tooth
Output shaft	stainless steel, hardened
Bearing at output	silicon bearing
Radial play, 6 mm from flange	max. 0.06 mm
Axial play	0.02–0.10 mm
Max. permissible axial load	8 N
Max. permissible force for press fits	100 N
Sense of rotation, drive to output	=
Recommended input speed	< 8000 rpm
Recommended temperature range	-15...+100°C
Extended range as option	-40...+100°C
Number of stages	1 2 3 4 5
Max. radial load, 6 mm from flange	8 N 12 N 16 N 20 N 20 N

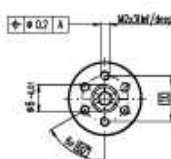
M 1:1

Block program Standard program Special program (on request)	Part Numbers							
	110321	110322	110323	110326	110324	134782	110325	134785
Gearhead Data								
1 Reduction	4.4:1	19:1	84:1	157:1	370:1	600:1	1621:1	3027:1
2 Reduction absolute								
3 Max. motor shaft diameter	2	2	2	1.5	2	2	2	2
RE 16								
1 Reduction	5.4:1	24:1	104:1		455:1	950:1	1906:1	3728:1
2 Reduction absolute								
3 Max. motor shaft diameter	1.5	2	2		2	1.5	2	2
A-max 16								
1 Reduction		29:1	128:1		561:1		2458:1	4502:1
2 Reduction absolute								
3 Max. motor shaft diameter		1.5	2		2		2	1.5
4 Number of stages	1	2	3	3	4	4	5	5
5 Max. continuous torque	Nm 0.10	0.15	0.20	0.20	0.25	0.25	0.30	0.30
6 Intermittently permissible torque at gear output	Nm 0.150	0.225	0.300	0.300	0.375	0.375	0.450	0.450
7 Max. efficiency	% 90	81	73	73	65	65	59	59
8 Weight	g 20	23	27	27	31	31	36	36
9 Average backlash no load	" 1.4	1.6	2.0	2.0	2.4	2.4	3.0	3.0
10 Mass inertia	gcm ² 0.07	0.05	0.05	0.04	0.05	0.05	0.05	0.05
11 Gearhead length L1	mm 15.5	16.1	22.7	22.7	26.3	26.3	29.9	29.9



Motor Modular System				
Motor	Page	Sensor/Brake	Page	Overall length [mm]
RE 16, 2 W	94			37.0
RE 16, 2 W	94	MR	298/300	43.6
RE 16, 3.2 W	95/96			56.0
RE 16, 3.2 W	96	MR	298/300	61.0
RE 16, 3.2 W	96	MEnc 13	313	62.1
RE 16, 4.5 W	97/98			59.0
RE 16, 4.5 W	98	MR	298/300	64.0
RE 16, 4.5 W	98	MEnc 13	313	65.2
A-max 16	113-116			41.0
A-max 16	114/116	MR	298/300	46.0
A-max 16	114/116	MEnc 13	313	49.1
RE-max 17	143-146			41.0
RE-max 17	144/146	MR	298/300	46.0
EC 16, 30 W	169			55.6
EC 16, 30 W	169	MR	301	66.3
EC-max 16, 5 W	187			39.8
EC-max 16, 5 W	187	MR	301	46.0
EC-max 16, 2-wire	188			49.1

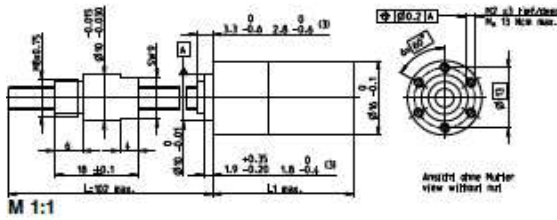
Option Ball Bearing	Part Numbers			Technical Data		
	4.4:1	19:1	84:1	Planetary Gearhead	straight tooth	
	138333	138334	138343	Output shaft	stainless steel, hardened	
	5.4:1	138334	561:1	138344	Bearing at output	preloaded ball bearings
	19:1	138335	600:1	138345	Radial play, 6 mm from flange	max. 0.08 mm
	24:1	138336	850:1	138346	Axial play at axial load	< 4 N max. 0.05 mm
	29:1	138337	1621:1	138347	Max. permissible axial load	25 N
	84:1	138338	1996:1	138348	Max. permissible force for press fits	100 N
	104:1	138339	2458:1	138349	Sense of rotation, drive to output	=
	128:1	138340	3027:1	138350	Recommended input speed	< 8000 rpm
	157:1	138341	3728:1	138351	Recommended temperature range	-15...+100°C
	370:1	138342	4502:1	138352	Extended range as option	-40...+100°C
					Number of stages	1 2 3 4 5
					Max. radial load, 6 mm from flange	10 N 15 N 20 N 20 N 20 N
					Gearhead values according to above bearing version	



A.4 Motion transmission

A.4.1 Translation transmission: spindle drive

Spindle Drive GP 16 S Ø16 mm, Ball Screw



Technical Data	
Spindle	Ø6 x 2, stainless steel
Standard length	102 mm
Spindel length (5 mm steps)	max. 200 mm
Nut (standard)	thread nut
Material	X46Cr13, hardened
Axial play	< 0.01 mm
Planetary gearhead	straight tooth
Bearing	ball bearing/axial bearing
Radial play 6 mm from flange	< 0.08 mm
Axial play	preload
Recommended input speed ²	< 12000 rpm
Recommended temperature range	-15...+80°C
Max. axial load (static) ¹	500 N
Number of stages	0 1 2 3 4
Max. radial load, 6 mm from flange	20 N 40 N 60 N 80 N 80 N

	Stock program Standard program Special program (on request)	Part Numbers				
		424221	424222	424223	424210	424204
Spindle Drive Data (provisional)						
1 Reduction		1:1	4.4:1	19:1	84:1	370:1
2 Reduction absolute		1/5	1/5	1/19	1/84	1/370
20 Max. feed velocity ²	mm/s	150	90.9	21.1	4.8	1.1
21 Max. feed force (continuous) ¹	N	54	64	104	171	280
22 Max. feed force (intermittent)	N	149	176	287	403	403
Part Numbers						
1 Reduction			5.4:1	24:1	104:1	455:1
2 Reduction absolute			1/5.4	1/24	1/104	1/455
20 Max. feed velocity ²	mm/s		74.1	16.7	3.8	0.9
21 Max. feed force (continuous) ¹	N		69	113	184	300
22 Max. feed force (intermittent) ¹	N		189	311	403	403
Part Numbers						
1 Reduction				424744	424747	424750
2 Reduction absolute				1/29.1	1/128.1	1/581.1
20 Max. feed velocity ²	mm/s			13.8	3.1	0.7
21 Max. feed force (continuous) ¹	N			120	197	322
22 Max. feed force (intermittent) ¹	N			331	403	403
Part Numbers						
1 Reduction					424748	424751
2 Reduction absolute					1/157.1	1/690.1
20 Max. feed velocity ²	mm/s				2.5	0.6
21 Max. feed force (continuous) ¹	N				211	345
22 Max. feed force (intermittent) ¹	N				403	403
Part Numbers						
1 Reduction						424752
2 Reduction absolute						1/850.1
20 Max. feed velocity ²	mm/s					0.5
21 Max. feed force (continuous) ¹	N					370
22 Max. feed force (intermittent) ¹	N					403
4 Number of stages		0	1	2	3	4
7 Max. efficiency gearhead incl. spindle	%	93	87	79	71	63
8 Weight ¹	g	52	58	81	65	80
9 Average backlash no load	"	1.0	1.4	1.6	2.0	2.4
23 Mechanical positioning accuracy ³	mm	0.030	0.041	0.042	0.044	0.046
10 Mass inertia gearhead incl. spindle ⁴	gmF	0.23	0.11	0.05	0.05	0.05
11 Gearhead length L1	mm	19.2	22.3	27.4	31.0	34.6
¹ based on spindle length 100 mm (standard length) ² for reduction 1:1 = 4500 rpm ³ for reduction 1:1						



Motor	Page	Sensor/Brake	Page	Overall length [mm]	Motor length + gearhead length + (sensor / brake) + assembly parts
RE 16, 2 W	94			41.6	44.7
RE 16, 2 W	94	MR	298/300	47.3	50.4
RE 16, 3.2 W	95/96			50.7	52.8
RE 16, 3.2 W	96	MR	298/300	54.7	57.8
RE 16, 3.2 W	96	MEnc 13	313	65.8	68.9
RE 16, 4.5 W	97/98			62.7	65.8
RE 16, 4.5 W	98	MR	298/300	67.7	70.8
RE 16, 4.5 W	98	MEnc 13	313	68.9	72.0

Continuation of the modular system (respectively of the spindles) on page 282 and 283.

A.4.2 Translation transmission: gear

Engrenage droit acier

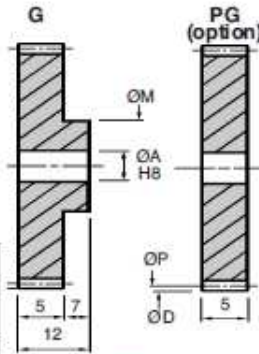


MODULE

Acier 34C10

0,5

- Classe de précision 9
- Angle de pression 20°
- Vitesse linéaire 300m/min



Indication de couple et de puissance				
Pour 50 dents à 1000 t/min.				
	34C10 210CNP10.00	34C10 trempé	laiton	fibre
Nm	0,391	1,850	0,195	0,156
KW	0,041	0,194	0,021	0,016

24/48 HEURES
en STOCK*
 sinon contactez-nous



REMISES

Qté	1+	6+	20+	40+
Rem. Prix	-12%	-25%	Sur demande	

Références	Z Dents	OP Primitif	OD Extérieur	OM Moyeu	OA Alésage	Stock*	Poids (kg)		Prix Uni. 1 à 5	
							G	PG	G	PG
G0.5-10	10	5.50	6.50	6.50	3	-	0.0020	0.0006	15.27	€
G0.5-11	11	6.00	7.00	7.00	3	-	0.0025	0.0008	15.27	€
G0.5-12	12	6.00	7.00	7.00	3	✓	0.0025	0.0008	15.27	€
G0.5-13	13	6.50	7.50	7.50	3	-	0.0030	0.0010	15.44	€
G0.5-14	14	7.00	8.00	8.00	3	✓	0.0035	0.0012	15.63	€
G0.5-15	15	7.50	8.50	8.50	3	✓	0.0037	0.0014	15.81	€
G0.5-16	16	8.00	9.00	8.50	4	✓	0.0038	0.0014	16.09	€
G0.5-17	17	8.50	9.50	8.50	4	-	0.0041	0.0017	16.23	€
G0.5-18	18	9.00	10.00	8.50	4	✓	0.0043	0.0020	16.33	€
G0.5-19	19	9.50	10.50	8.50	4	-	0.0046	0.0022	16.52	€
G0.5-20	20	10.00	11.00	8.50	4	✓	0.0049	0.0025	16.84	€
G0.5-21	21	10.50	11.50	8.50	4	-	0.0052	0.0028	17.00	€
G0.5-22	22	11.00	12.00	8.50	4	-	0.0055	0.0032	17.20	€
G0.5-23	23	11.50	12.50	8.50	4	✓	0.0059	0.0035	17.42	€
G0.5-24	24	12.00	13.00	10.00	5	✓	0.0067	0.0036	17.60	€
G0.5-25	25	12.50	13.50	10.00	5	✓	0.0071	0.0039	17.81	€
G0.5-26	26	13.00	14.00	10.00	5	-	0.0075	0.0043	18.02	€
G0.5-27	27	13.50	14.50	10.00	5	-	0.0079	0.0047	18.27	€
G0.5-28	28	14.00	15.00	10.00	5	-	0.0083	0.0051	18.52	€
G0.5-29	29	14.50	15.50	10.00	5	-	0.0087	0.0056	18.52	€
G0.5-30	30	15.00	16.00	10.00	5	-	0.0092	0.0060	18.63	€
G0.5-31	31	15.50	16.50	10.00	5	-	0.0096	0.0065	18.86	€
G0.5-32	32	16.00	17.00	10.00	5	✓	0.0101	0.0069	19.07	€
G0.5-33	33	16.50	17.50	10.00	5	-	0.0106	0.0074	19.26	€
G0.5-34	34	17.00	18.00	10.00	5	-	0.0111	0.0079	19.43	€
G0.5-35	35	17.50	18.50	10.00	5	✓	0.0116	0.0085	19.74	€

Sur demande

*Dans la limite du disponible

Références	Z Dents	QP Primitif	QD Extérieur	QM Moyeu	QA Alésage	Stock*	Poids (kg)		Prbr. Uni. 1 à 5	
							G	PG	G	PG
G0.5-36	36	18,00	19,00	10,00	5	✓	0,0121	0,0090	19,93 €	
G0.5-37	37	18,50	19,50	10,00	5	-	0,0127	0,0095	20,15 €	
G0.5-38	38	19,00	20,00	10,00	5	-	0,0133	0,0101	20,31 €	
G0.5-39	39	19,50	20,50	10,00	5	-	0,0138	0,0107	20,54 €	
G0.5-40	40	20,00	21,00	10,00	5	✓	0,0144	0,0113	20,74 €	
G0.5-41	41	20,50	21,50	10,00	5	-	0,0150	0,0119	20,96 €	
G0.5-42	42	21,00	22,00	10,00	5	-	0,0157	0,0125	21,18 €	
G0.5-43	43	21,50	22,50	10,00	5	-	0,0163	0,0131	21,35 €	
G0.5-44	44	22,00	23,00	10,00	5	-	0,0169	0,0138	21,57 €	
G0.5-45	45	22,50	23,50	10,00	5	-	0,0176	0,0145	21,78 €	
G0.5-46	46	23,00	24,00	10,00	5	-	0,0183	0,0151	22,00 €	
G0.5-47	47	23,50	24,50	10,00	5	-	0,0190	0,0158	22,20 €	
G0.5-48	48	24,00	25,00	10,00	5	-	0,0197	0,0166	22,67 €	
G0.5-49	49	24,50	25,50	10,00	5	✓	0,0204	0,0173	22,67 €	
G0.5-50	50	25,00	26,00	12,00	6	✓	0,0222	0,0177	22,91 €	
G0.5-51	51	25,50	26,50	12,00	6	-	0,0230	0,0185	23,05 €	
G0.5-52	52	26,00	27,00	12,00	6	-	0,0238	0,0192	23,17 €	
G0.5-53	53	26,50	27,50	12,00	6	-	0,0246	0,0200	23,40 €	
G0.5-54	54	27,00	28,00	12,00	6	-	0,0254	0,0208	23,50 €	
G0.5-55	55	27,50	28,50	12,00	6	-	0,0262	0,0216	23,67 €	
G0.5-56	56	28,00	29,00	12,00	6	-	0,0270	0,0225	23,82 €	
G0.5-57	57	28,50	29,50	12,00	6	-	0,0279	0,0233	23,99 €	
G0.5-58	58	29,00	30,00	12,00	6	-	0,0287	0,0242	24,14 €	
G0.5-59	59	29,50	30,50	12,00	6	-	0,0296	0,0251	24,32 €	
G0.5-60	60	30,00	31,00	12,00	6	✓	0,0305	0,0260	24,46 €	
G0.5-61	61	30,50	31,50	12,00	6	-	0,0314	0,0269	24,56 €	
G0.5-62	62	31,00	32,00	12,00	6	-	0,0323	0,0278	24,75 €	
G0.5-64	64	32,00	33,00	12,00	6	-	0,0342	0,0297	25,09 €	
G0.5-65	65	32,50	33,50	12,00	6	-	0,0352	0,0307	25,28 €	
G0.5-68	68	34,00	35,00	12,00	6	-	0,0382	0,0337	25,43 €	
G0.5-70	70	35,00	36,00	12,00	6	✓	0,0403	0,0357	25,72 €	
G0.5-72	72	36,00	37,00	12,00	6	✓	0,0424	0,0379	25,98 €	
G0.5-75	75	37,50	38,50	12,00	6	-	0,0457	0,0412	26,18 €	
G0.5-77	77	38,50	39,50	12,00	6	-	0,0480	0,0435	26,49 €	
G0.5-80	80	40,00	41,00	12,00	6	✓	0,0515	0,0470	26,74 €	
G0.5-84	84	42,00	43,00	12,00	6	-	0,0565	0,0519	26,96 €	
G0.5-86	86	43,00	44,00	12,00	6	-	0,0590	0,0545	27,30 €	
G0.5-88	88	44,00	45,00	12,00	6	-	0,0616	0,0571	27,50 €	
G0.5-90	90	45,00	46,00	12,00	6	✓	0,0643	0,0598	27,83 €	
G0.5-96	96	48,00	49,00	12,00	6	-	0,0727	0,0682	28,07 €	
G0.5-100	100	50,00	51,00	12,00	6	✓	0,0786	0,0740	28,17 €	
G0.5-120	120	60,00	61,00	18,00	6	✓	0,1116	0,1071	34,11 €	
G0.5-140	140	70,00	71,00	18,00	6	-	0,1507	0,1462	40,76 €	
G0.5-150	150	75,00	76,00	18,00	6	-	0,1725	0,1679	44,31 €	
G0.5-180	180	90,00	91,00	20,00	8	-	0,2469	0,2423	50,11 €	
G0.5-200	200	100,00	101,00	20,00	8	-	0,3040	0,2994	54,73 €	
G0.5-220	220	110,00	111,00	20,00	10	-	0,3671	0,3625	59,67 €	
G0.5-250	250	125,00	126,00	20,00	10	-	0,4730	0,4684	65,60 €	
↓ Au choix : tout engrenage jusqu'à cette taille ↓										
G0.5-278	278	139,00	140,00	Dimensions : contactez-nous			sur demande			

*Dans la limite du disponible

Fax: 0325 88 6000

cial2@hpceurope.com

HPC

Tome 4 2013 4 213

Sur demande

A.5 Sensors used

A.5.1 Joint position sensors used for the translation and rotation motors

Encoder MR Type M, 128–512 CPT, 2/3 Channels, with Line Driver

Timing diagram showing three channels (A, B, I) with pulse widths and phase relationships. Cycle T = 200%, Pulse T = 100%, Pulse width = 50%, $t_{A-B} = 90^\circ$, $t_{A-I} = 45^\circ$. Direction of rotation cw (definition on p. 72).

Program	228176	228177	228181	228182	201957	261948
Stock program						
Standard program						
Special program (on request)						

Type	128	128	256	256	512	512
Number of channels	3	3	2	3	2	3
Max. operating frequency (kHz)	80	80	160	160	300	300
Max. speed (rpm)	37500	37500	37500	37500	37500	37500



Motor	Pages	Gearhead	Pages	Brake	Pages	Overall length [mm] / see Gearhead					
RE 16, 2 W	102					28.0	28.0	28.0	28.0	28.0	28.0
RE 16, 2 W	102	GP 16, 0.1 - 0.6 Nm	254/255								
RE 16, 2 W	102	GP 16 S	206/207								
RE 16, 3.2 W	104					45.4	45.4	45.4	45.4	45.4	45.4
RE 16, 3.2 W	104	GP 16, 0.1 - 0.6 Nm	254/255								
RE 16, 3.2 W	104	GP 16 S	206/207								
RE 16, 4.5 W	106					48.4	48.4	48.4	48.4	48.4	48.4
RE 16, 4.5 W	106	GP 16, 0.1 - 0.6 Nm	254/255								
RE 16, 4.5 W	106	GP 16 S	206/207								
A-max 16	120/124					30.4	30.4	30.4	30.4	30.4	30.4
A-max 16	120/124	GS 16, 0.01 - 0.1 Nm	250/253								
A-max 16	120/124	GP 16, 0.1 - 0.6 Nm	254/255								
A-max 16	120/124	GP 16 S	206/207								
A-max 19, 1.5 W	126					34.0	34.0	34.0	34.0	34.0	34.0
A-max 19, 1.5 W	126	GP 19, 0.1 - 0.3 Nm	257								
A-max 19, 1.5 W	126	GP 22, 0.5 - 2.0 Nm	263/264								
A-max 19, 1.5 W	126	GS 24, 0.1 Nm	260								
A-max 19, 1.5 W	126	GP 22 S	209/300								
A-max 19, 2.5 W	128					35.8	35.8	35.8	35.8	35.8	35.8
A-max 19, 2.5 W	128	GP 19, 0.1 - 0.3 Nm	257								
A-max 19, 2.5 W	128	GS 20 0.06 - 0.25 Nm	260								
A-max 19, 2.5 W	128	GP 22, 0.5 - 2.0 Nm	263/264								
A-max 19, 2.5 W	128	GS 24, 0.1 Nm	260								
A-max 19, 2.5 W	128	GP 22 S	209/300								
A-max 22	130/132					36.0	36.0	36.0	36.0	36.0	36.0
A-max 22	130/132	GP 22, 0.1 - 0.6 Nm	260/261								
A-max 22	130/132	GP 22, 0.5 - 2.0 Nm	263/264								
A-max 22	130/132	GS 24, 0.1 Nm	260								
A-max 22	130/132	GP 22 S	209/300								
RE-max 17	150/154					30.4	30.4	30.4	30.4	30.4	30.4
RE-max 17	150/154	GP 16, 0.1 - 0.3 Nm	254								


Technical Data	Pin Allocation	Connection example
Supply voltage V_{CC} : 5 V \pm 5% Output signal: TTL compatible Phase shift ϕ : 90° \pm 45° Index pulse width: 90° \pm 45° Operating temperature range: -25...+85°C Moment of inertia of code wheel: \approx 0.50 gcm ² Output current per channel: max. 5 mA	<p>1 Motor + 2 Vcc 3 GND 4 Motor - 5 Channel T 6 Channel A 7 Channel B 8 Channel I 9 Channel T (Index) 10 Channel I (Index)</p> <p>10M Connector 4162.U EN 60600-13 AWI shield cable AWG 28 *version with 3 channels</p>	<p>Line driver Recommended ICs: MC 3401 28 pin DIP AM 26 LS 23</p> <p>Terminal resistance R = typical 120 Ω Capacitor C \geq 0.1 nF per m line length</p>

A.5.2 Proximity sensors used for the translated blocks

SICK
Sensor Intelligence.

Inductive proximity sensors
Rectangular housing, IQ04

Model Name > IQ04-1B5PSKWZS
Part No. > 6042017




At a glance

- Flat, compact design
- Long sensing distance up to 1.5 mm
- Easily visible indication LEDs
- Available in a plastic housing
- Dimensions: 8 mm x 16 mm x 4 mm

Your benefits

- Reduced mechanical damage due to space-saving flat housing, which does not protrude from sensor
- Time-saving simple installation with one or two screws
- No restrictions on machine design

CE 

Features

Housing:	Rectangular
Dimensions (W x H x D):	8 mm x 16 mm x 4 mm
Sensing range Sr:	1.5 mm
Assured sensing range Sa:	1.215 mm
Installation type:	Flush
Switching frequency:	600 Hz
Switching output:	PNP
Output function:	NO
Electrical wiring:	DC 3-wire
Enclosure rating:	IP 67 ¹⁾
Connection type:	Cable, 3-wire, 2 m

¹⁾ According to EN 60529

Mechanics/electronics

Supply voltage:	10 V DC...30 V DC
Ripple:	≤ 10 % ¹⁾
Voltage drop:	< 1.5 V ²⁾
Power consumption:	10 mA ³⁾
Time delay before availability:	≤ 10 ms
Hysteresis:	1 % ... 15 %
Repeatability:	± 1 % ^{4) 5)}
Temperature drift (% of Sr):	± 10 %

Inductive proximity sensors © SICK AG. Subject to change without notice. 4/3/2013 3:48:41 PM

EMC:	According to EN 60947-5-2
Output current I _a :	100 mA
Cable material:	PVC
Conductor cross-section:	0.09 mm ²
Cable diameter:	2.5 mm
Short-circuit protection:	✓
Shock/vibration:	30 g, 11 ms/10 ... 55 Hz, 1 mm
Ambient operating temperature:	-25 °C ... 70 °C
Housing material:	Plastic
Sensing face material:	Plastic, PA 6
Tightening torque, max.:	≤ 0.06 Nm

¹⁾ Or V_S ²⁾ At I_a max ³⁾ Without load ⁴⁾ U_b and T_a constant ⁵⁾ Or 5r

Reduction factors

Note:	The values are reference values which may vary
Stainless steel (V2A, 304):	Ca. 0.7
Copper (Cu):	Ca. 0.3
Aluminum (Al):	Ca. 0.4
Brass (Br):	Ca. 0.4

Installation note

A:	0 mm
B:	16 mm
C:	8 mm
D:	4,5 mm
E:	0 mm
F:	24 mm
Remark:	Associated graphic see "Installation"

A.6 Controllers

The *EPOS3 70/10 EtherCAT* cards used allow three control modes: position control; velocity control; and torque control. The mode used to validate the controller proposed in Chapter 5 is the torque mode.



Figure A.5 – EPOS3 70/10 EtherCAT

A.7 Communication loop

Several motors can be controlled at the same time, they are connected in series with an *Ethernet* cable. The *EtherCAT* communication protocol allows the communication with the master which runs in real time under *Linux RTAI*. The synchronization and addressing are automatically ensured thanks to the *EtherCAT* communication protocol. A *Beckho EK1100* coupler is used to transit the informations between the master and the slaves (*EPOS3* cards).

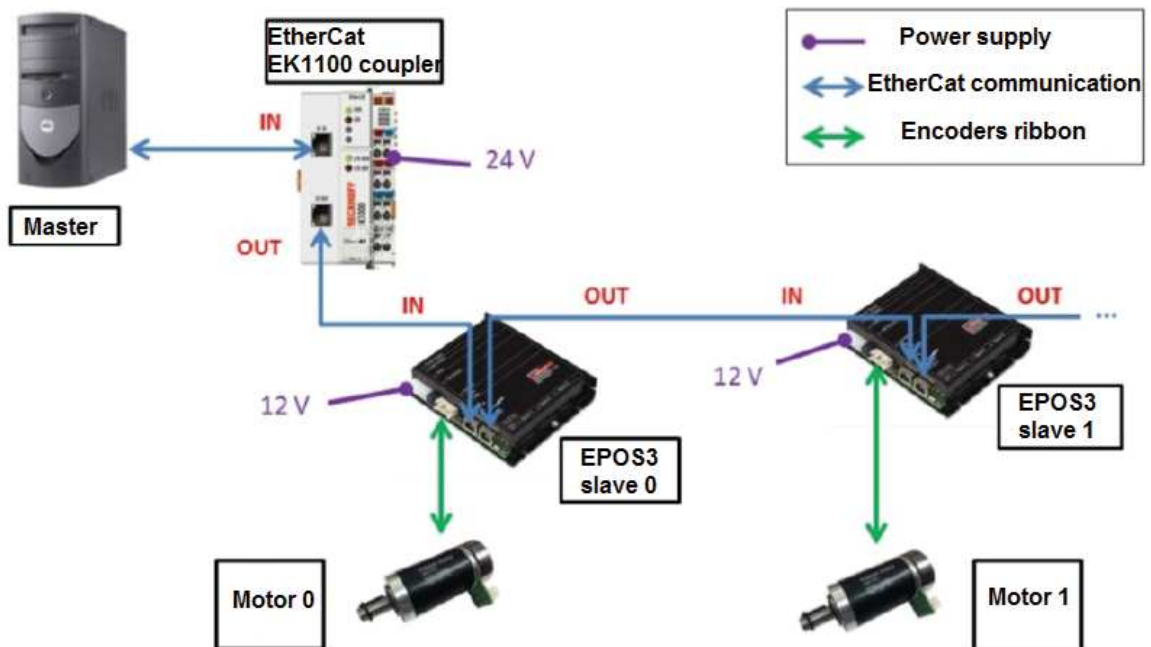


Figure A.6 – Communication loop.

List of Publications

1. M. N. Boushaki, C. Liu, and P. Poignet. Task-space position control of concentric-tube robot with inaccurate kinematics using approximate jacobian. In IEEE International Conference on Robotics and Automation, pages 5877–5882, 2014.
2. M. N. Boushaki, M. T. Chikhaoui, K. Rabenorosoa, C. Liu, N. Andreff, and P. Poignet. Conception, modélisation et commande des robots à tubes concentriques : vers des applications médicales. *Technique de l'Ingénieur*, (S7767), 2016.
3. M. N. Boushaki, C. Liu, V. Trevillot, and P. Poignet. Endonasal Endoscopic Approach for Deep Brain Tumors Using Concentric Tube Robot, SURGETICA 2014.
4. M. N. Boushaki, C. Liu, and P. Poignet. Optimization of Concentric-Tube Robot Design for Deep Anterior Brain Tumor Surgery. submitted to ICARCV 2016.



Bibliography

URL www.euroflex.de. Cited page 74.

URL www.iarc.fr. Cited pages 9 and 64.

URL www.youtube.com/watch?v=y4s9i3ucBmY. Cited pages 63 and 128.

R. Alterovitz, S. Patil, and A. Derbakova. Rapidly-exploring roadmaps: Weighing exploration vs. refinement in optimal motion planning. *Proc. IEEE Int. Conf. Robotics and Automation (ICRA)*, May 2011. Cited page 30.

E. Amanov, T. Nguyen , and J. Burgner-Kahrs. Additive manufacturing of patient-specific tubular continuum manipulators, 2015. Cited page 98.

T. Anor, J. R. Madsen, and P. E. Dupont. Algorithms for design of continuum robots using the concentric tubes approach: A neurosurgical example. In *IEEE International Conference on Robotics and Automation*, pages 667–673, 2011. Cited pages 24, 25, 27, 56, and 57.

S. S. Antman. *Nonlinear Problems of Elasticity*. Springer, 1995. Cited pages 28, 46, and 50.

Charles Audet and J. E. Dennis Jr. Analysis of Generalized Pattern Searches. *SIAM Journal on Optimization*, 13(3):889–903, 2003. Cited page 25.

- H. Azimian, T. Looi, and J. Drake. Closed-loop inverse kinematics under inequality constraints : Application to concentric-tube manipulators. In *IEEE International Conference on Intelligent Robots and Systems*, pages 498 – 503, 2014. Cited pages 23 and 33.
- C. Bedell, J. Lock, A. Gosline, and P. E. Dupont. Design optimization of concentric tube robots based on task and anatomical constraints. In *IEEE International Conference on Robotics and Automation*, pages 398–403, 2011. Cited pages 24, 25, 27, 51, 56, 57, and 58.
- C. Bergeles and P. E. Dupont. Planning stable paths for concentric tube robots. In *IEEE International Conference on Intelligent Robots and Systems*, pages 3077–3082, 2013. Cited pages 30 and 31.
- C. Bergeles, A. H. Gosline, N. V. Vasilyev, P. J. Codd, P. J. del Nido, and P. E. Dupont. Concentric tube robot design and optimization based on task and anatomical constraints. *IEEE Transactions on Robotics*, 31(1):67–84, 2015. Cited pages 26, 27, 57, 58, and 71.
- M. N. Boushaki, C. Liu, and P. Poignet. Task-space position control of concentric-tube robot with inaccurate kinematics using approximate jacobian. In *IEEE International Conference on Robotics and Automation*, pages 5877–5882, 2014. Cited page 79.
- M. N. Boushaki, M. T. Chikhaoui, K. Rabenoroso, C. Liu, N. Andreff, and P. Poignet. Conception, modélisation et commande des robots à tubes concentriques : vers des applications médicales. *Technique de l'Ingénieur*, (S7767), 2016. Cited page 13.
- J. Burgner, P. J. Swaney, D. C. Rucker, H. B. Gilbert, S. T. Nill, P. T. Russell, K. D. Weaver, and R. J. Webster. A bimanual teleoperated system for endonasal skull base surgery. In *IEEE International Conference on Intelligent Robots and Systems*, pages 2517–2523, 2011. Cited pages 16, 17, 23, 24, 25, 27, 32, 51, 56, 57, 64, 73, and 127.
- J. Burgner, P. J. Swaney, T. L. Bruns, M. S. Clark, D. C. Rucker, E. C. Burdette, and R. J. Webster. An Autoclavable Steerable Cannula Manual Deployment Device: Design and Accuracy Analysis. *Journal of Medical Devices*, 6(4):41007–1 – 41007–7, 2012. Cited page 23.

- J. Burgner, H. B. Gilbert, and R. J. Webster. On the computational design of concentric tube robots: Incorporating volume-based objectives. In *IEEE International Conference on Robotics and Automation*, pages 1193–1198, 2013a. Cited pages [26](#), [27](#), [56](#), and [57](#).
- J. Burgner, P. J. Swaney, R. A. Lathrop, K. D. Weaver, and R. J. Webster. Debulking from within: A robotic steerable cannula for intracerebral hemorrhage evacuation. *IEEE, Transactions on Biomedical Engineering*, 60(9):2567–2575, 2013b. Cited page [23](#).
- J. Burgner, D. C. Rucker, H. B. Gilbert, P. J. Swaney, P. T. Russell, K. D. Weaver, and R. J. Webster. A Telerobotic System for Transnasal Surgery. *IEEE/ASME Transactions on Mechatronics*, 19(3):996–1006, 2014. Cited pages [16](#), [17](#), [23](#), [32](#), [33](#), [51](#), and [127](#).
- J. Burgner-Kahrs, D. C. Rucker, and H. Choset. Continuum robots for medical applications: A survey. *IEEE Transactions on Robotics*, 31(6):1261–1280, 2015. Cited page [8](#).
- E. J. Butler, R. Hammond-Oakley, S. Chawarski, A. H. Gosline, P. Codd, T. Anor, J. R. Madsen, P. E. Dupont, and J. Lock. Robotic Neuro-Endoscope with Concentric Tube Augmentation, 2012. Cited page [23](#).
- M. Caramia and P. Dell’Olmo. Multi-objective management in freight logistics. *Springer*, 2008. Cited pages [59](#), [63](#), and [70](#).
- D. C. Cardona. A mri compatible concentric tube continuum robot with pneumatic actuation. Master’s thesis, Vanderbilt University, 2012. Cited pages [17](#), [18](#), [23](#), and [127](#).
- M. T. Chikhaoui, K. Rabenoroso, and N. Andreff. Kinematics and performance analysis of a novel concentric tube robotic structure with embedded soft micro-actuation. *Mechanism and Machine Theory*, 104:234 – 254, 2016. Cited page [22](#).
- D. B. Comber, D. Cardona, R. J. Webster, and E. J. Barth. Sliding Mode Control of an MRI-Compatible Pneumatically Actuated Robot. *Proceedings of the Fluid Power and Motion Control Symposium*, pages 283–293, 2012. Cited pages [18](#), [19](#), [23](#), [32](#), [33](#), and [127](#).
- E. Cosserat and F. Cosserat. *Théorie des corps déformables*. ÉDITIONS JACQUES GABAY, 1909. Cited pages [28](#) and [46](#).

- J. M. Croom, D. C. Rucker, J. M. Romano, and R. J. Webster. Visual sensing of continuum robot shape using self-organizing maps. In *IEEE International Conference on Robotics and Automation*, pages 4591–4596, 2010. Cited page 98.
- Rucker D. Caleb and Webster III R. J. Mechanics of Bending, Torsion, and Variable Pre-curvature in Multi - Tube Active Cannulas. *International Conference on Robotics and Automation*, pages 2533–2537, 2009b. Cited pages 27 and 80.
- Levy Doron. Introduction to Numerical Analysis, 2010. Cited page 45.
- P. E. Dupont, J. Lock, and E. Butler. Torsional kinematic model for concentric tube robots. In *IEEE International Conference on Robotics and Automation*, pages 3851–3858, 2009. Cited pages 28, 45, and 69.
- P. E. Dupont, J. Lock, B. Itkowitz, and E. Butler. Design and control of concentric-tube robots. *IEEE Transactions on Robotics*, 26(2):209–225, 2010a. Cited pages 8, 19, 21, 23, 24, 28, 32, 46, 52, 58, 71, 72, 75, and 127.
- P. E. Dupont, J. Lockand, and B. Itkowitz. Real-time position control of concentric tube robots. In *IEEE International Conference on Robotics and Automation*, pages 562–568, 2010b. Cited pages 32, 33, and 51.
- J. Furusho, T. Katsuragi, T. Kikuchi, T. Suzuki, H. Tanaka, Y. Chiba, and H. Horio. Curved multi-tube systems for fetal blood sampling and treatments of organs like brain and breast. *Journal of Computer Assisted Radiology and Surgery*, pages 223 – 226, 2006. Cited pages 25, 28, 29, and 80.
- Junji Furusho, Tomoya Ono, R. Murai, T. Fujimoto, Y. Chiba, and H. Horio. Development of a curved multi-tube (CMT) catheter for percutaneous umbilical blood sampling and control methods of CMT catheters for solid organs. *IEEE International Conference Mechatronics and Automation*, (July):410–415, 2005. Cited page 36.
- H. B. Gilbert and R. J. Webster. Can concentric tube robots follow the leader? In *IEEE International Conference on Robotics and Automation*, pages 4881–4887, 2013. Cited pages 24 and 26.

- H. B. Gilbert, J. Neimat, and R. J. Webster. Concentric tube robots as steerable needles: Achieving follow-the-leader deployment. *IEEE Transactions on Robotics*, 31(2):246–258, 2015. Cited page 26.
- A. H. Gosline, N. V. Vasilyev, E. J. Butler, C. Folk, A. Cohen, R. Chen, N. Lang, P. J. del Nido, and P. E. Dupont. Percutaneous intracardiac beating-heart surgery using metal MEMS tissue approximation tools. *International Journal of Robotics Research*, 31(9):1081–1093, 2012a. Cited pages 19, 21, 23, and 127.
- A. H. Gosline, N. V. Vasilyev, A. Veeramani, M. Wu, G. Schmitz, R. Chen, V. Arabagi, P. J. del Nido, and P. E. Dupont. Metal mems tools for beating-heart tissue removal. In *IEEE International Conference on Robotics and Automation*, pages 1921–1926, 2012b. Cited page 25.
- J. Ha, F. C. Park, and P. E. Dupont. Achieving elastic stability of concentric tube robots through optimization of tube precurvature. In *IEEE International Conference on Intelligent Robots and Systems*, pages 864–870, 2014. Cited pages 26, 27, and 57.
- R. J. Hendrick, S. D. Herrell, and R. J. Webster. A multi-arm hand-held robotic system for transurethral laser prostate surgery. In *IEEE International Conference on Robotics and Automation*, pages 2850–2855, 2014. Cited pages 21, 22, 23, 51, and 127.
- Burgner-Kahrs Jessica, Rucker D. Caleb, and Choset Howie. Continuum Robots for Medical Applications: A Survey. *IEEE TRANSACTIONS ON ROBOTICS*, pages 1261–1280, 2015. Cited page 56.
- S. Karaman and E. Frazzoli. Incremental sampling-based algorithms for optimal motion planning. *Computing Research Repository*, 2010. Cited page 30.
- S. Karaman and E. Frazzoli. Sampling-based algorithms for optimal motion planning. *International Journal of Robotics Research*, 30(7):846 – 894, 2011. Cited page 30.
- E. M. Kasprzak and K. E. Lewis. An approach to facilitate decision tradeoffs in Pareto solution sets. *Journal of Engineering Valuation and Cost Analysis*, pages 173–187, 2000. Cited pages 60, 61, and 62.

- C. Kim, S. C. Ryu, and P. E. Dupont. Real-time adaptive kinematic model estimation of concentric tube robots. In *IEEE International Conference on Intelligent Robots and Systems*, pages 3214–3219, 2015. Cited page 99.
- J. Lagarias, Reeds J. A, Wright M. H, and Wriqh P. E. Convergence Properties of the Nelder-Mead Simplex Method in Low Dimensions. *SIAM Journal of Optimization*, 1998. Cited page 26.
- S. M. LaValle. Planning Algorithms. *Cambridge, U.K.: Cambridge University Press*, 2006. Cited page 26.
- C. Liu and C. C. Cheah. Task-space Adaptive Setpoint Control for Robots with Uncertain Kinematics and Actuator Model. *Transactions on Automatic Control*, pages 1854–1860, 2006. Cited page 82.
- C. Liu, C. C. Cheah, and J. J. E. Slotine. Adaptive Jacobian Tracking Control of Rigid-Link Electrically Driven Robots based on Visual Task-Space Information. *Automatica*, pages 1491–1501, 2006. Cited page 82.
- J. Lock and P. E. Dupont. Friction Modeling in Concentric Tube Robots. *International Conference on Robotics and Automation*, page 1139–1146, 2011. Cited page 28.
- Lisa a. Lyons, Robert J. Webster, and Ron Alterovitz. Motion planning for active cannulas. *2009 IEEE/RSJ International Conference on Intelligent Robots and Systems, IROS 2009*, pages 801–806, 2009. Cited pages 29, 31, and 80.
- Lisa A Lyons, Robert J Webster III, and Ron Alterovitz. Planning active cannula configurations through tubular anatomy. In *IEEE International Conference on Robotics and Automation*, pages 2082–2087, Anchorage, USA, May 2010. Cited pages 29, 31, and 80.
- Mohsen Mahvash and Pierre E Dupont. Stiffness Control of Surgical Continuum Manipulators. *IEEE TRANSACTIONS ON ROBOTICS*, 27(2):334–345, 2011. Cited pages 29, 32, and 33.
- R. M. Murray, Z. L. Li, and S. S. Sastry. *A Mathematical Introduction to Robotic Manipulation*. CRC Press, 1994. Cited pages 47 and 49.

- J. A. Nelder and R. Mead. A simplex method for function minimization. *The Computer Journal.*, 1965. Cited page [26](#).
- S. Neppalli, M. A. Csencsits, B. A. Jones, and I. D. Walker. Closed-form inverse kinematics for continuum manipulators. *Advanced Robotics*, pages 2077–2091, 2009. Cited page [80](#).
- J. Park and W. Chung. Geometric Integration on Euclidean Group With Application to Articulated Multibody Systems. *IEEE TRANSACTIONS ON ROBOTICS*, page 850–863, 2005. Cited page [47](#).
- III R. J. Webster and B. A. Jones. Design and kinematic modeling of constant curvature continuum robots: A review. *International Journal of Robotics Research*, 29:1661–1683, 2010. Cited pages [37](#), [41](#), [80](#), [82](#), and [128](#).
- III R. J. Webster, J. M. Romano, and N. J. Cowan. Mechanics of precurved-tube continuum robots. *IEEE Transactions on Robotics*, 25:67–78, 2009. Cited pages [28](#), [30](#), [42](#), and [44](#).
- H. Ren and P. E. Dupont. Tubular enhanced geodesic active contours for continuum robot detection using 3d ultrasound. In *IEEE International Conference on Robotics and Automation*, pages 2907–2912, 2012. Cited page [99](#).
- J. Rosen, B. Hannaford, and R. M. Satava, editors. *Surgical Robotics*. Springer, 2011. Cited page [7](#).
- D. C. Rucker. *THE MECHANICS OF CONTINUUM ROBOTS: MODEL-BASED SENSING AND CONTROL*. PhD thesis, Vanderbilt University, 2011. Cited page [30](#).
- D. C. Rucker and R. J. Webster. Computing jacobians and compliance matrices for externally loaded continuum robots. In *Robotics and Automation (ICRA), 2011 IEEE International Conference on*, pages 945–950, 2011. Cited page [50](#).
- D. C. Rucker, Robert J Webster III, G. S. Chirikjian, and N. J. Cowan. Equilibrium conformations of concentric-tube continuum robots. *International Journal of Robotics Research*, 29:1263–1280, 2010a. Cited pages [28](#) and [46](#).

- D. Caleb Rucker, Bryan a. Jones, and Robert J. Webster. A geometrically exact model for externally loaded concentric-tube continuum robots. *IEEE Transactions on Robotics*, 26(5):769–780, 2010b. Cited pages 26, 28, and 46.
- Daniel Caleb Rucker and Robert J. Webster. Parsimonious evaluation of concentric-tube continuum robot equilibrium conformation. *IEEE Transactions on Biomedical Engineering*, 56(9):2308–2311, 2009. Cited page 25.
- R.M. Satava. Future applications of robotics. *Prob. Gen. Surg.*, 20(2):79–85, 2003. Cited page 7.
- Patrick Sears and Pierre Dupont. A Steerable Needle Technology Using Curved Concentric Tubes. *2006 IEEE/RSJ International Conference on Intelligent Robots and Systems*, pages 2850–2856, 2006. Cited pages 27, 28, 42, 51, and 56.
- Patrick Sears and Pierre Dupont. Inverse Kinematics of Concentric Tube Steerable Needles. *International Conference on Robotics and Automation*, pages 1887–1892, 2007. Cited pages 51 and 80.
- J. J. E. Slotine and W. Li. *Applied Nonlinear Control*. 1991. Cited page 85.
- M. H. Smith, C. L. Flanagan, J. M. Kemppainen, J. A. Sack, H. Chung, S. Das, S. J. Hollister, and S. E. Feinberg. Computed tomography-based tissue-engineered scaffolds in craniomaxillofacial surgery. *The international journal of medical robotics + computer assisted surgery : MRCAS*, 2(3):207–216, 2006. Cited page 36.
- Hao Su, Diana C. Cardona, Weijian Shang, Alexander Camilo, Gregory a. Cole, D. Caleb Rucker, Robert J. Webster, and Gregory S. Fischer. A MRI-guided concentric tube continuum robot with piezoelectric actuation: A feasibility study. *Proceedings - IEEE International Conference on Robotics and Automation*, pages 1939–1945, 2012. Cited pages 17, 18, 23, 51, 80, and 127.
- P. J. Swaney, J. M. Croom, J. Burgner, H. B. Gilbert, D. C. Rucker, R. J. Webster, K. D. Weaver, and P. T. Russell. Design of a quadramanual robot for single-nostril skull base surgery. *Annual Dynamic Systems and Control Conference joint with the JSME Motion and Vibration Conference*, 2012. Cited page 23.

- P. J. Swaney, A. Mahoney, H. B. Gilbert, A. Ramirez, E. Lamers, B. Hartley, R. Feins, R. Alterovitz, and R. J. Webster III. Tendons, concentric tubes, and a bevel tip: Three steerable robots in one transoral lung access system. In *IEEE International Conference on Robotics and Automation*, pages 5378–5383, 2015. Cited page 23.
- Luis G. Torres and Ron Alterovitz. Motion planning for concentric tube robots using mechanics-based models. *IEEE International Conference on Intelligent Robots and Systems*, pages 5153–5159, 2011. Cited pages 30, 31, and 51.
- Luis G Torres, Robert J Webster III, and Ron Alterovitz. Task-oriented design of concentric tube robots using mechanics-based models. In *IEEE/RSJ International Conference on Intelligent Robots and Systems*, pages 4449–4455, 2012. Cited pages 25, 27, 30, 31, 56, and 57.
- Luis G Torres, Cenk Baykal, and Ron Alterovitz. Interactive-rate Motion Planning for Concentric Tube Robots. *IEEE International Conference on Robotics and Automation*, pages 1915–1921, 2014. Cited pages 30 and 31.
- V. Torzcon. On the Convergence of Pattern Search Algorithms. *SIAM J Optimization*, 7(1): 1–25, 1997. Cited page 24.
- R. Unal, G. Kiziltas, and V. Patoglu. Multi-criteria Design Optimization of Parallel Robots. *IEEE Conference on Robotics, Automation and Mechatronics*, pages 3888–3895, 2008. Cited pages 58 and 70.
- V. Vitiello, S. L. Lee, T. P. Cundy, and G. Z. Yang. Emerging robotic platforms for minimally invasive surgery. *IEEE Reviews in Biomedical Engineering*, 6:111–126, 2013. Cited page 7.
- C. Wampler. Manipulator Inverse Kinematic Solutions Based on Vector Formulations and Damped Least-Squares Methods. *IEEE Transactions on Systems, Man, and Cybernetics*, pages 93–101, 1986. Cited pages 32 and 51.
- R. J Webster, J. M. Romano, and N. J. Cowan. Kinematics and calibration of active cannulas. *International Conference on Robotics and Automation*, pages 3888–3895, 2008. Cited page 28.

- Robert J. Webster, John P. Swensen, Joseph M. Romano, and Noah J. Cowan. Closed-form differential kinematics for concentric-tube continuum robots with application to visual servoing. *Springer Tracts in Advanced Robotics*, 54:485–494, 2009. Cited pages 31 and 33.
- Robert J Webster III. *Design and Mechanics of Continuum Robot for Surgery*. PhD thesis, The John Hopkins University, 2007. Cited pages 17, 23, 43, 52, and 127.
- Robert J Webster III, A. M. Okamura, and N. J. Cowan. Toward active cannulas: Miniature snake-like surgical robots. In *IEEE/RSJ International Conference on Intelligent Robots and Systems*, pages 2857–2863, 2006. Cited page 27.
- R Xu and R V Patel. A fast torsionally compliant kinematic model of concentric-tube robots. *Conference proceedings : Annual International Conference of the IEEE Engineering in Medicine and Biology Society. IEEE Engineering in Medicine and Biology Society. Conference*, 2012:904–7, January 2012. Cited pages 28 and 33.
- Ran Xu, Ali Asadian, Anish S. Naidu, and Rajni V. Patel. Position control of concentric-tube continuum robots using a modified Jacobian-based approach. *Proceedings - IEEE International Conference on Robotics and Automation*, pages 5813–5818, 2013. Cited pages 20, 21, 23, 33, 51, and 127.
- Ran Xu, Ali Asadian, Seyed Farokh Atashzar, and Rajni V Patel. Real-time Trajectory Tracking for Externally Loaded Concentric-tube Robots. *IEEE International Conference on Robotics and Automation*, pages 4374–4379, 2014. Cited pages 23 and 33.



List of Figures

1.1	Conception of a concentric tube robot.	9
1.2	Nasal access to the frontal lobe using CTR.	10
2.1	Actuation unit with serial translation blocks: a) structure, b) kinematic scheme.	16
2.2	CTR with serial actuation blocks and coupled rotation/translation for three tubes [Webster III, 2007]	17
2.3	RTC equipped with two three-tubes arms and an actuation serial unit without coupling [Burgner et al., 2011] [Burgner et al., 2014].	17
2.4	Two-tubes CTR with a) pneumatic actuation unit [Cardona, 2012] and b) piezoelectric actuation unit [Su et al., 2012] non coupled.	18
2.5	Three-tubes CTR actuated pneumatically with translation coupling [Comber et al., 2012].	19
2.6	CTR actuation unit with parallel translation blocks: a) structure b) kinematic graph.	20
2.7	RTC a) [Dupont et al., 2010a] b) [Gosline et al., 2012a] with three tubes decoupled and actuated in parallel.	21
2.8	Two-tubes CTR with parallel actuation unit [Xu et al., 2013]	21
2.9	a) Two arms CTR with b) parallel actuation unit [Hendrick et al., 2014].	22

3.1	Tow mappings defining the forward kinematic model: f_1 from the joint space (α_i, l_i) to the configuration space (ρ_j, l_j, φ_j) and f_2 from the configuration space to the task space (tip pose \mathbf{X}). This figure is adapted from [R. J. Webster and Jones, 2010].	37
3.2	Two-tube CTR with three constant curvature sections, from the base to the tip: the first section of length l_1 delimited by the frame \mathbf{H}_1 (attached to the base of the outer tube) and by the frame \mathbf{H}_2 (attached to the distal extremity of the straight part of the outer tube) is composed of two straight tubes; the second section of length l_2 delimited by the frame \mathbf{H}_2 and the frame \mathbf{H}_3 (attached to the distal extremity of the curved part of the outer tube) is composed of a curved dominant outer tube and an inner tube with a straight and a curved part; the third section of length l_3 is composed of only one curved tube and is delimited by the frames \mathbf{H}_3 and \mathbf{H}_t which is attached to the tip.	38
3.3	Section geometry, adapted from [R. J. Webster and Jones, 2010].	41
3.4	Two-tube CTR with four constant curvature sections, from the base to the tip: the first section is composed of two straight tubes; the second section is composed of an outer curved tube and an inner straight tube; the third section is composed by two curved tubes and the fourth section is a single curved tube.	42
3.5	Effect of tube curvatures on the elastic stability: from the blue (***) to the red (***) dot-curve, the curvatures of the two tubes are increased as $1/100, 1/80, 1/70, 1/60 \text{ mm}^{-1}$, and the lengths of both tubes are set to 100 mm . . .	52
3.6	Effect of tube lengths on the elastic stability: from the blue (***) to the red (***) dot-curve, the lengths of the two tubes are increased as $(100, 120, 140, 160) \text{ mm}$, and the curvatures of both tubes are set to $1/100 \text{ mm}^{-1}$	53
4.1	Evolution of CTR tubes design. (ISM: Infinite Stiffness Model, TFM: Torsion Free Model, TCM: Transmissional Compliant Model)	57
4.2	Example of a Pareto front in case of two objective functions.	60
4.3	Convex and non-convex Pareto curve.	61
4.4	Mapping from decision space to objective space.	62
4.5	Transcranial intervention for frontal lobe tumor resection [YOU]	63
4.6	Work-space characterization (a-c) and inner tubes insertion (d).	65

<i>List of Figures</i>	129
4.7 Robot shaft sections	67
4.8 CTR Robot: CAD and real platform.	68
4.9 Joint jumps	72
4.10 Stability evaluation	76
4.11 Reachability evaluation	76
4.12 Stability/Reachability selection	77
5.1 The task-space desired trajectory at the master side is converted through the inverse kinematic model f_{InvKin} to a desired joint trajectory at the slave side.	81
5.2 CTR Prototype: (top) Zoomed in picture of the concentric tubes (bottom) Whole system with actuators.	86
5.3 Workspace	87
5.4 Control schemes: a) Inverse kinematic control, b) Task-space control	88
5.5 The performances of the two control strategies with modelling inaccuracy and uncertainty in the parameter k_1	90
5.6 The performances of the two control strategies with modelling inaccuracy and uncertainty in the parameter k_1 and k_2	91
5.7 TS Control with $(k'_1 = 60\% \cdot k_1, k'_2 = 60\% \cdot k_2)$. The upper limit of the kinematic uncertainties bound is exceeded, and thus the tip position diverges.	93
5.8 CTR Shape During Control	94
A.1 System setup of CTR.	101
A.2 Base structure of the CTR robot.	102
A.3 Side and top view of the CTR robot.	102
A.4 CAD of the assembled CRT under Solidworks.	103
A.5 EPOS3 70/10 EtherCAT	114
A.6 Communication loop.	115



List of Tables

2.1	Existing CTR prototypes.	23
2.2	Algorithms of tubes design optimization for RTC	27
2.3	Path planing algorithms for CTRs	31
2.4	Control architectures of RTC.	33
3.1	Tubes parameters used in simulation of length and curvature effects on the elastic stability.	53
4.1	Notations and Dimensions	70
4.2	Tubes parameters used in simulation of length and curvature effects on the elastic stability.	75
5.1	Tubes parameters.	88
5.2	Comparison of Position Errors (mm) using two control strategies: Inverse Kinematics (IK) Control and Task-space (TS) Control	92